

ABSTRACT

Title of Document: ANALYTICAL MODELING AND
EXPERIMENTAL EVALUATION OF A
PASSIVELY MORPHING ORNITHOPTER
WING

Aimy Wissa, Doctor of Philosophy, 2014

Directed By: Langley Distinguished Professor, James E.
Hubbard, Jr., Department of Aerospace
Engineering

Ornithopters or flapping wing Unmanned Aerial Vehicles (UAVs) have potential applications in both civil and military sectors. Amongst all categories of UAVs, ornithopters have a unique ability to fly in low Reynolds number flight regimes and have the agility and maneuverability of rotary wing aircraft. In nature, birds achieve such performance by exploiting various wing kinematics known as gaits. The objective of this work was to improve the steady level flight performance of an ornithopter by implementing the Continuous Vortex Gait using a novel passive compliant mechanism. A compliant mechanism, called a compliant spine, was fabricated, and integrated in the ornithopter's wing leading edge spar. Each compliant spine was designed to be flexible in bending during the wing upstroke and stiff in bending during the wing downstroke. Inserting a variable stiffness compliant mechanism in the leading edge spar of the ornithopter could affect its structural stability. An analytical model was developed to determine the structural stability

of the ornithopter leading edge spar. The model was validated using experimental measurements. After ensuring the structural stability of the leading edge spar, a test ornithopter was tested in air and in vacuum as well as in free and constrained flight with various compliant spine designs inserted in its wings. Results from all the tests, proved that feasibility and efficacy of passive wing morphing using a compliant mechanism in improving the steady level flight performance of the test ornithopter. Inserting the compliant spine into the leading edge spar of the ornithopter during free flight reduced the baseline configuration body vertical center of mass positive acceleration by 69%, which translates into overall lift gains. It also increased the horizontal propulsive force by 300%, which translates into thrust gains.

ANALYTICAL MODELING AND EXPERIMENTAL EVALUATION OF A
PASSIVELY MORPHING ORNITHOPTER WING

By

Aimy A. Wissa

Dissertation submitted to the Faculty of the Graduate School of the
University of Maryland, College Park, in partial fulfillment
of the requirements for the degree of
Doctor of Philosophy
2014

Advisory Committee:

Professor James E. Hubbard Jr., Chair

Professor Amr Baz

Professor Anya Jones

Professor Darryll Pines

Professor Norman Wereley

@ Copyright

Aimy A. Wissa

2014

Preface

This research was funded by the Air Force Office of Scientific Research (AFOSR) under grants FA9550-09-1-0632 and FA9550-13-0126

Dedication

“Thus far the Lord has helped us” 1 Samuel 7:12

This work is dedicated to the glory of the name of Jesus Christ and to my lovely family
and amazing fiancé.

Acknowledgments

“Nothing in the world can take the place of persistence, talent will not: nothing is more common than unsuccessful men with talent. Genius will not: unrewarded genius is almost a proverb. Education will not: the world is full of educated derelicts. Persistence and Determination alone are omnipotent.” Calvin Coolidge

The quote above was posted on my office’s door the first day I reported to graduate school. For a while, I thought it meant my own persistence and determination, however, almost six years of graduate school changed this perspective. I discovered that it took the persistence and determination of other people and their belief in me in order to reach this point in my professional career. I would like to use this section to attempt and recognize those whose support and persistence are the reasons that this work is complete.

First, I would like to thank my advisor, mentor, and role model, Dr. James E. Hubbard Jr. Dr. Hubbard has always been a source of endless support and wisdom. He taught me the true meanings of teamwork and leadership. He was always determined to see the best in me and was always persistent when it came to helping me achieve excellence. I could have not asked for a better adviser. Thank you Dr. Hubbard for being the incredible human being you are. You have truly made a difference in my life and the lives of everyone you encounter.

Second, I would like to thank my committee members, their guidance along the way was essential in helping me complete this work. Dr. Baz was always encouraging and supportive, and always believed in my work and for that I am grateful. I am also very thankful to Dr. Jones, she was always very prompt during our communications. Dr. Pines,

meeting with him was always a pleasure. I knew that I could always rely on getting great advice from him whether it was about the fundamentals of linear momentum or career decisions. I am also very grateful of Dr. Wereley's guidance and support. Without his help, I would not have been able to complete the analytical portion of my work and strengthen my analytical skills. Moreover, I am thankful for two mentors whose support during my undergraduate years was crucial to my success today. I would like to recognize Dr. George Lesieutre, who was my undergraduate thesis adviser and the first person to introduce me to the world of research. I would also like to acknowledge the efforts of Dr. Janice Margle, who guided me through the first two years of my undergraduate studies and who always encouraged me to pursue a doctorate in engineering.

Third, I am forever thankful to the support of my lab mates. I am so blessed to be a part of such an incredible group of intellects. This work would have not been possible without the support and persistence of Gen I and Gen II (Cornelia Alltenbuchner, Nelson Guerriero, Jared Grauer, Geoff Slipher, Sandra Ugrina, and Ben Nickless,). Special thanks to Jared and Nelson, who took time out of their busy schedules to help me during the flight test. I am also very thankful to Gen III (Jose Mondragon, Michael Cunningham, Zohaib Hasnain, and Nick Rymer) and I wish them a research journey full of successes and excitement.

Fourth, I would like to acknowledge the persistence and love of one friend and colleague who truly changed and saved my life. My life would have not been the same, if I had not met Alexander Brown. Alex taught me to believe in myself, his positive outlook on life and persistence to excel in everything he did, proved to me that anything is possible. Thank you Alex for teaching me how to become a leader and thank you for the short three years we spent together. I will always remember you as a friend, a brother, and a mentor.

My journey through graduate school would not have been as memorable without my incredible group of friends. I would like to thank Denisse Aranda, Taylor Spalt, Duncan McGillvray, Nicole Pothier, Limor Nevel, Marian Nous, Shady Farah, Nermin Hanna, and Jared Grauer for your unconditional friendship. Thank you for being there through the peaks and valleys of this journey and thank you for letting me know through actions and words that I can always rely on you.

Finally, I would like to thank my family. My father, Aziz Wissa, has always been my rock and support. He always believed in me and in my potential even when I did not believe in myself. As for my mother, she is a daily proof of unconditional love and sacrifices. Through the years, she never missed a day without asking about me. She has always been my confidant and the person I can share anything with. As for my youngest and only sister, I would like to thank her for always holding me at a higher standard. Her faith in me and in my ability helped me become a stronger person. The last member of my family that I would like to recognize is my incredible fiancé, Mina. Mina's selflessness through the last three years cannot be described by words. He always put my needs before his and my interest at a higher priority. I am very thankful for his presence. I am truly blessed to have such a loving man in my life.

Table of Contents

Preface.....	ii
Dedication.....	iii
Acknowledgments.....	iv
Table of Contents.....	vii
List of Tables.....	x
List of Figures.....	xi
1. Chapter 1: Introduction.....	1
1.1. Small Unmanned Air Vehicles Background.....	1
1.1.1. A Comparison of Fixed, Rotary, and Flapping Wing UAVS.....	1
1.1.2. Scale Classification of Flapping Wing UAVs.....	2
1.2. Review of Morphing in Flapping Wing Vehicles.....	3
1.2.1. Review of Active Wing Morphing.....	4
1.2.2. Review of Passive Wing Morphing.....	8
1.3. Current Research Goal, Hypothesis and Objectives.....	12
1.4. Dissertation Outline.....	13
2. Chapter 2: Technical Approach.....	16
2.1. Research Platform Description.....	16
2.2. A Bio-inspired Passive Approach to in Flight Wing Morphing.....	21
2.2.1. Avian Wing Morphology and Flight Kinematics.....	21
2.2.1.1. Avian Wing Morphology.....	21
2.2.1.2. Avian Wing Kinematics.....	23
2.2.2. Continuous Vortex Gait Design Specifications.....	31
2.2.2.1. Compliant Spine Load Specifications.....	32

2.2.2.1.	Compliant Spine Bending Deflection Specifications	35
2.3.	Compliant Spine Design	36
2.4.	Chapter Summary	40
3.	Chapter 3: Leading Edge Spar Analytical Model and Stability Analysis.....	42
3.1.	Leading Edge Spar Equations of Motion.....	42
3.2.	Leading Edge Spar Model Validation.....	45
3.3.	Leading Edge Spar Stability Analysis	49
3.4.	Effect of Damping on Leading Edge Spar Stability	53
3.5.	Chapter Summary	57
4.	Chapter 4: Constrained Flight Test Experiment	58
4.1.	Preliminary Constrained Flight Test.....	58
4.1.1.	Experimental Procedures of Constrained Flight Test.....	58
4.1.2.	Experimental Results of Constrained Flight Test.....	62
4.2.	Constrained Flight Test in Vacuum	68
4.2.1.	Vacuum Test Experimental Procedures.....	68
4.2.1.1.	Facility and Equipment.....	68
4.2.1.2.	Tested Wing Spar Configurations.....	70
4.2.2.	Vacuum Constrained Flight Test Results	72
4.3.	Chapter Summary	76
5.	Chapter 5: Free Flight Testing Experiment	78
5.1.	Free Flight Testing Experimental Procedures.....	78
5.1.1.	Test Platform Experimental Setup.....	79
5.1.2.	Flight Testing Technique	81

5.1.3.	Free Flight Tested Ornithopter Wing Configurations.....	82
5.2.	Free Flight Experimental Results.....	83
5.2.1.	Ornithopter's Free Flight Kinematics.....	84
5.2.2.	Effect of Compliant Spine Presence on Leading Edge Spar Deflection	89
5.2.3.	Effect of Compliant Spine Presence on Wing Performance.....	92
5.2.3.1.	The Power Expenditure Performance Metric	92
5.2.3.2.	Horizontal Propulsive Force Performance Metric	93
5.2.3.3.	Vertical Propulsive Force Performance Metric	96
5.3.	Chapter Summary	99
6.	Chapter 6: Concluding Remarks.....	101
6.1.	Summary of Work.....	101
6.2.	Summary of Original Contributions	103
6.3.	Future Recommendations	105

List of Tables

Table 1. Specifications for the Park Hawk test platform	16
Table 2. Experimental and Simulation Strains recorded at the locations of the compliant mechanisim root and tip [Adapted from [20]].	34
Table 3. Bending deflections at the compliant spine tip relative to the wing root*.	67
Table 4. Throttle settings tested for all wing spar configurations in air and vacuum.	70
Table 5. Specifications of compliant spine designs for vacuum constrained flight test. ..	72
Table 6. Specifications of compliant spine designs.	83
Table 7. Values for horizontal power loading for the non-compliant and compliant wing spar configurations.	95
Table 8. Values for the coefficient of vertical propulsive force for the solid and compliant wing spar configurations.	99

List of Figures

Figure 1. Flight capabilities that are only achievable using small flapping wing unmanned air vehicles.	2
Figure 2. Schematic of a wing flapping mechanism for bird-sized UAVs [15].	6
Figure 3. Bio-inspired bat-like MAV. The robot wings include shape memory alloy wires that enable wing folding [18].	7
Figure 4. Schematic of wing design showing the sections, which would be exposed during the upstroke [27].	8
Figure 5. Passive torsional spring that allow for bending only during the upstroke and locks during the downstroke [28].	9
Figure 6. The morphing wing shape at mid downstroke (left) and mod upstroke (right) due to the presence of a passive torsional spring inserted at the wing half span [28].	10
Figure 7. The compliant hinges designed to enable wing bending during the upstroke: (Top) solid hinge concept, (Middle) flexible Delrin hinge concept, and (Bottom) compliant carbon fiber hinge concept.	11
Figure 8. Morphing wing with compliant carbon fiber hinge at 50% of wing half span..	11
Figure 9. Research work flow chart	13
Figure 10. Park Hawk test Platform.....	17
Figure 11. ML101 test platform.....	18
Figure 12. Top view of the test platform wing showing the nylon membrane, the finger spars and the leading edge and diagonal spars.....	19

Figure 13. High speed photography of the stroke cycle. Downstroke is presented on the left column, starting at the top of the figure and ending at the bottom. Upstroke begins at the bottom of the right column and continues to the top of the right column [6].	20
Figure 14. Relative dimensions of the hand wing to arm wing for five species: a) Calliope hummingbird; (b) Rock dove; (c) Blue grouse; (d) Starling; (e) Albatross [33].	22
Figure 15. Wings of an albatross and a pheasant showing the difference in aspect ratio. Albatross has an AR of 14 while the pheasant has an aspect ratio of 5.	23
Figure 16. Interpretation of the vortex ring gait wake structure behind a chaffinch in flapping flight [38].	24
Figure 17. Interpretation of the continuous vortex gait wake structure behind a chaffinch in flapping flight [Adapted from [39]].	25
Figure 18. Top view of the vortex ring gait (top) and continuous vortex gait (bottom) wake structure of flapping birds (Top). [Adapted from [34]].	25
Figure 19. Illustration of the effect of Aspect Ratio and flight speed on gait selection in birds [35].	27
Figure 20. Vertical and horizontal forces produced during the downstroke and upstroke of a flapping wing beat cycle.	28
Figure 21. Top view of a pigeon's wing flight in a variable speed wing tunnel showing the wing kinematics at: A) mid downstroke, B) mid upstroke of a vortex ring gait with tip reversal upstroke C) mid mid upstroke of a vortex ring gait with feathered upstroke kinematics, and D) mid upstroke of a continuous vortex gait upstroke. [Taken from [34]]	29

Figure 22. Side and top view of the wingtip and wrist paths of a pigeon during (a) a tip reversal upstroke vortex ring gait, (b) a feathered upstroke vortex ring gait, and (c) a continuous vortex gait [Adapted from [34]].	30
Figure 23. During the continuous vortex gait the wings are fully extended at mid downstroke (left) and out of plane bent, twisted and swept at mid upstroke (right) [Adapted from [45]].	31
Figure 24. The compliant spine is inserted into the leading edge spar to mimic the function of an avian wrist	32
Figure 25. Strain gages mounted on the leading edge spar at the location of the compliant spine root and tip	33
Figure 26. Experimental set-up for measuring the strains at the locations of the compliant spine root and tip at a flapping frequency of 5 Hz.	33
Figure 27. Inboard and Outboard Strains at the Location of the Compliant Spine Root and Tip	35
Figure 28. Lateral Flapping Sequence for a Cockatiel in a Wind Tunnel	36
Figure 29. (a) The desired stiffness of the compliant spine is nonlinear. The Y-axis represents the forces during a flapping cycle and the X-axis represents the compliant spine tip bending deflection (b) Schematic of a compliant spine with three compliant joints.	37
Figure 30. The geometry (left) and von-Mises stress distribution at mid upstroke (right) of all the compliant spine designs tested.	39

Figure 31. Compliant spines were assumed to have clamped-free boundary condition and were designed using either tip load (TL) loading condition (right) or pure moment (PM) loading condition (left). 40

Figure 32. The research platform mounted on a test stand with the compliant leading edge spar model superimposed on the right wing for clarification. 43

Figure 33. Detailed model of the leading edge spar with a torsional spring representing the compliant spine showing all relevant angles, lengths, and masses. 44

Figure 34. a) A Phantom high speed camera mounted outside the vacuum chamber. b) 3 LED panels mounted on the inside of the chamber to light the chamber and cause the markers to reflect light 46

Figure 35. Example of a leading edge spar-spine configuration that was used to validate the leading edge spar analytical model. 47

Figure 36. Experimental and analytical wing root angle versus time normalized by the period of one wing beat cycle. The experiment agrees with the model within 7%. . 48

Figure 37. Experimental and analytical spine root angle versus time normalized by the period of one wing beat cycle. The experiment agrees with the model within 11%. 49

Figure 38. Strutt diagram for Mathieu’s equation. The lines form boundaries or transition point between stable and unstable solution regions. Regions marked with US are unstable and regions marked with S are stable. 51

Figure 39. Strutt diagram for Mathieu’s equation in terms of the upstroke and downstroke stiffness. The black dot represents compliant spine Comp 4TL. Regions marked with US are unstable and regions marked with S are stable. 52

Figure 40. Phase plane plot of the spine root angle. The plot shows that the response of the leading edge spar with design Comp 4TL inserted at 37% of the wing half span is bounded and stable.....	53
Figure 41. Model of the leading edge spar-spine system with a linear damping element	54
Figure 42. Strutt Diagram of the Lossy Mathieu's Equation for the cases of $\zeta=0$ (red), 0.2 (blue), and 0.5 (green).....	55
Figure 43. Strutt diagram for the lossy Mathieu's equation in terms of the upstroke and downstroke stiffness for the cases of $\zeta=0$ (red), 0.2 (blue), and 0.5 (green).	56
Figure 44. The compliant spine was attached to the spar (a) using 10-32 Nylon bolts. The bolts were glued to both ends of the spar as shown in (b) and (c). Then the spars were screwed into the ends of the spine as shown in (d) and (e).....	59
Figure 45. Schematic of current sensor circuit.	60
Figure 46. (a) Test ornithopter mounted on a six channel load cell. (b) The compliant spine was inserted at the leading edge spar of the test ornithopter at 37% of the wing half span	61
Figure 47. Red markers at the wing leading edge used for capturing wing bending deflections at the wing root, the compliant spine tip and the wing tip.	61
Figure 48. (a) Electric power required vs. flapping frequency (b) Flapping frequency versus percent throttle for the continuous and compliant ornithopter.	63
Figure 49. (a) Mean lift produced over one flapping cycle, normalized by the weight versus percentage throttle (b) Mean thrust produced over one flapping cycle versus throttle position plot.....	65

Figure 50. (a) Wing bending deflections at mid downstroke for the ornithopter with the continuous spar, i.e., without the compliant spine. (b) Wing bending deflections at mid downstroke for the ornithopter with the compliant spine. (c) Wing bending deflections at mid upstroke for the ornithopter with the continuous spar. (d) Wing bending deflections at mid upstroke for the ornithopter with the compliant spine. . 66

Figure 51. (a) NASA LaRC 5 foot x 5 foot thermal vacuum chamber. (b) Test ornithopter mounted inside the vacuum chamber..... 69

Figure 52. (a) Test ornithopter mounted on a six channel load cell in a 5 ft x 5 ft thermal vacuum chamber. (b) Load cell mounted on an aluminum pylon inside the vacuum chamber..... 70

Figure 53. Compliant spine assembly components..... 71

Figure 54. Mean thrust versus flapping frequency for the Continuous, Comp 4PM, Comp 4TL, and Comp 24PM wing spar configurations in ambient pressure (red and black data markers) and at vacuum (green and yellow data markers)..... 73

Figure 55. Mean lift normalized by the vehicle’s weight for the Continuous, Comp 4PM, Comp 4TL, and Comp 24PM wing spar configurations in ambient pressure (black and red data markers) and at vacuum (yellow and green data markers)..... 74

Figure 56. Mean pitching moment versus flapping frequency for the Continuous, Comp 4PM, Comp 4TL, and Comp 24PM wing spar configurations in ambient pressure (black and red data) and in vacuum (yellow and green data). 75

Figure 57. Test Chamber in the AFRL SUAS flight lab..... 78

Figure 58. (a) Wing and (b) Tail reflective markers placement. 80

Figure 59. (a) Schematic for current sensor. (b) Logomatic v2 Serial SD data logger used to record the current sensor output.....	81
Figure 60. Test setup schematic showing the Vicon® cameras (representative), high speed cameras, flight path, braking tether, and video capturing area.	82
Figure 61. The flight testing control volume, showing the inertial, CI, and body fixed, C0, coordinate systems along with the position vector naming conventions.	84
Figure 62. X, Y, and Z position of the 53 markers mounted on the ornithopter with respect to the inertial frame of reference showing over eight flapping cycles of consistent and repeatable kinematics.	86
Figure 63. Ornithopter fuselage’s center of mass altitude (red line) showing that the test ornithopter is flying above the altitude threshold (black line) for free flight.	86
Figure 64. The altitude above ground level of the right wing tip marker (blue) and the fuselage's center of mass (red) versus time, normalized by the period of one flapping cycle.	87
Figure 65. Wing tip marker Z-position with respect to the center of mass (blue) and the center of mass acceleration (black) versus time normalized by the period of one flapping cycle.....	88
Figure 66. Wing tip marker Z-position with respect to the center of mass (blue), thrust flap marker Z-position with respect to the center of mass (green), and the center of mass acceleration (black) versus time, normalized by the period of one flapping cycle.	89
Figure 67. Wing planform showing the thrust flap region and the locations of the wing tip and thrust flap markers.....	89

Figure 68. The Z position of the reflective markers mounted at the right wing leading edge spar versus the normalized span location at (a) mid upstroke and (b) mid downstroke.....	91
Figure 69. Mean specific power over one flapping cycle for the compliant and solid, non-compliant, wing configurations.	93
Figure 70. Coefficient of mean horizontal propulsive force for the compliant and solid, non-compliant, wing configurations.	94
Figure 71. Vertical acceleration of the fuselage center of mass for the solid (black), Comp 4PM (green, and Comp 24PM (red) configurations versus time normalized by the period of one flapping cycle	96
Figure 72. Mean positive vertical acceleration over one flapping cycle for the compliant and solid, non-compliant, wing configurations.....	98

Chapter 1: Introduction

1.1. Small Unmanned Air Vehicles Background

Unmanned Air Vehicles (UAVs) have the potential to revolutionize the civil and military markets [1]. In the civil market, UAVs can improve the methods currently used to survey crops, monitor the environment, and respond to disasters, just to mention a few applications. On the military side, UAVs can be used for intelligence, surveillance and reconnaissance applications. They can be useful in high urban areas or for missions that are too dull, dirty, and dangerous for humans [1, 2]. For the last few decades, interest in small scale UAVs has peaked. Smaller UAVs (SUAVs) are enabled through advances in electronics and the availability of lightweight structures [3, 4]. There are three main categories to consider when trying to classify current SUAVs platforms. These are fixed, rotary, and flapping wing SUAVs.

1.1.1. A Comparison of Fixed, Rotary, and Flapping Wing UAVS

When compared to fixed or rotary wing SUAVs, flapping wing vehicles fill a unique niche [5]. At small scales and slow flight speeds, fixed wing SUAVs suffer from a deterioration in steady level flight performance due to drag penalties [6]. Flapping wing SUAVS or ornithopters, overcome those penalties because of their ability to generate additional lift using the unsteady flow around their wings and by using phenomenon such as dynamic stall and stable leading edge vortices [1, 7]. Also at small scales, flapping wing SUAVs have higher agility and maneuverability than fixed wing and rotary wing SUAVs [7]. Flapping wing SUAVs are also quieter and safer than rotary wing SUAVs of the same size. They also provide an element of stealth by mimicry, which could be useful for military

applications. Flapping wing un-manned air vehicles are also unique in their mission adaptability. Flapping wing un-manned air vehicles, like natural flyers, can have the ability to cruise, hover, perch, and maneuver efficiently. Figure 1 summarizes the key motivations behind developing and implementing ornithopters in both the civil and military markets. The figure shows a triangle of flight properties that can only be achieved using flapping wing, un-manned air vehicle platforms. The three sides of the triangle are improved flight performance at small scale and slow flight speeds or low Reynolds number, agility, and mission adaptability.

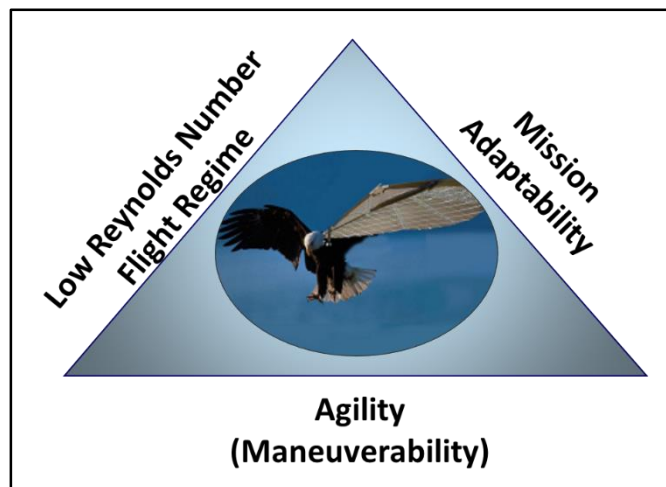


Figure 1. Flight capabilities that are only achievable using small flapping wing unmanned air vehicles.

1.1.2. Scale Classification of Flapping Wing UAVs

Within the category of flapping wing un-manned air vehicles, there is a distinct classification according to a vehicle's scale. This classification divides flapping wing unmanned air vehicle into two subcategories: insect scale and avian scale SUAVs. The insect scale SUAVS are also referred to as micro air vehicles (MAV). The design specification for MAVs is to have a wing span that is no longer than 15 cm [4, 1, 2]. When

compared to insect scale SUAVs, avian scale SUAVS have received less attention [8, 9]. Avian scale SUAVs are useful and worthy of attention because they have a higher payload capability and are more suitable for outdoor flight as they can withstand higher wind gusts. Nonetheless, in order for avian scale SUAVs to reach their full potential and achieve the capabilities shown in Figure 1, wing morphing is required.

1.2. Review of Morphing in Flapping Wing Vehicles

The word morphing is short for metamorphose [10], which is defined in Webster's dictionary as to "change in an important way into something that is very different" [11]. Among the aeronautical community, morphing is defined as changing the vehicle shape or properties in order to improve performance [10, 12]. In short, morphing can be defined as radical shape change. In nature, morphing can be observed in birds, bats and insects during flight and it is used to alter the flight dynamics of the flyer [13]. During flight, birds change their head position and tail orientation but changing their wing shape has the most pronounced effect on their flight dynamics [4]. Morphing enables natural flyers to perform efficiently over multiple missions scenarios [14]. It also allows smaller birds like the European Kestrel to fly forward at various speeds, glide to save energy while maintaining superior maneuverability [15]. Morphing also enables larger birds such as the falcon, to use its extended wings to loiter and then morph its wings into a strike configuration to catch its prey [16]. Wing morphing is beneficial for both steady level flight performance and for maneuverability. During steady level flight, wing morphing during the upstroke reduces the drag and lift penalties experienced during this portion of the wing beat cycle [2]. A numerical model developed by Wu and Liang shows that separately changing the wing camber, surface area, and bending of a flapping wing vehicle during steady level flight

improves the mean lift coefficient from 0.79 to 2.49, 1.69, and 0.89, respectively [17]. In bats, research shows that wing morphing has a great impact on maneuverability [18]. The same holds true for birds and insects, the wing morphing enables the high level of maneuverability observed in birds and insects during flight. Designing adaptive wings for UAVs will allow the man made vehicles to perform efficiently during multiple mission roles, improve its steady level flight performance, and maneuverability.

With respect to fixed wing UAVs, actuators are required to achieve wing morphing, thus only active approaches to morphing are feasible [10]. Wing morphing in flapping wing UAVs, however, can be achieved using active or passive approaches [19]. The next two subsections present a literature review of both active and passive wing morphing approaches for flapping wing UAVs. Active wing morphing is defined as a wing shape change due to inputs from the pilot or a control system. Passive wing morphing on the other hand is defined as wing shape change due to the operational loads the vehicle experience during flight and not due to control actuation from a pilot or a control system [19].

1.2.1. Review of Active Wing Morphing

Most wing morphing efforts in the literature follow an active wing morphing approach. For fixed wing unmanned air vehicles, this approach to morphing is necessary. A detailed review of fixed wing UAVs morphing aircraft is found in [10] and [12]. Wing morphing research for flapping wings is limited when compared to fixed wings. Wing morphing efforts for ornithopters can be divided into two main categories. The first category includes designing the flapping mechanism to achieve certain wing trajectories and the second category is on designing mechanisms that cause wing shape change during flight. The majority of the work found in the literature belongs to the first category.

The first category is inspired by the wing musculature of insects. Insect wings only contain muscles at the root. A desired wing trajectory is obtained during flight by actuating the muscles at the wing root, while the rest of the wing is simply a passive flexible structure [13]. The majority of the flapping mechanisms designed for UAVs use either smart materials or multiple bar linkages [20]. Conn et al. presents a review of flapping mechanism designs developed for unmanned air vehicles [21]. From the review of the current mechanisms, the authors concluded that more than one mechanism was required to incorporate full three degree of freedom (DOF) motion, which increases the vehicle's mass and complexity. Conn also presented a novel parallel crank rocker mechanism that had flapping and pitching degrees of freedom. The mechanism prototype was tested on 75 mm long wings. The wings produced 3.35 grams of lift while the weight of the motor used to power the mechanism was 7 grams [21]. Flight testing this setup would not be possible as the wings would not be able to support the motor. Cox et. al. and Frampton et. al. designed four and five bar linkages that convert the linear output of a piezoelectric actuator into a single degree of freedom flapping motion. The lift and thrust produced by the wings flapped by this mechanism were measured and related to the wing first bending and torsion frequency ratio. No successful flight tests were reported [22, 23]. Banala and Argwal designed a flapping mechanism than includes a four-bar and a five-bar linkage to generate an insect-like figure eight wing tip motion. The mechanism was successful in producing the desired motion however, it was only tested on a bench top and not in free flight [24]. Madangpol et al used an insect's thorax, where the wing muscles are present, as inspiration to design a flapping wing mechanism. The mechanism included two four-bar linkages, a crank shaft and two tensional springs. The presence of the tensional springs in the

mechanism reduced the load on the motor and reduced the power required. The mechanism was successfully implemented on a 36 cm wing span ornithopter and flight tests were reported [25]. Also Zdunich et al developed and tested the Mentor, which is a flapping wing MAV. The flapping mechanism on the vehicle enabled it to cruise and hover. Successful free flight tests was reported for two vehicle prototypes [26]

Even though successful flight tests were reported for insect scale flapping wing UAVs that achieve a desired wing trajectory by articulating a mechanism at the wing root the same cannot be said about bird scale UAVS. As the wings and vehicle size increase to avian scale, the flapping mechanisms become heavier, more complex, and demand more power. Thus making them ill-suited for flight testing. Grand et al. designed a wing flapping mechanism that allows for wide range of dihedral and twist variations [15]. Figure 2 shows a schematic of the wing flapping mechanism. The mechanism contained four motors each of which weighed 100 grams. Therefore, in order for the wing to support the weight of the motors alone, they need to produce 400 grams, which limits the overall payload capability a test vehicle.

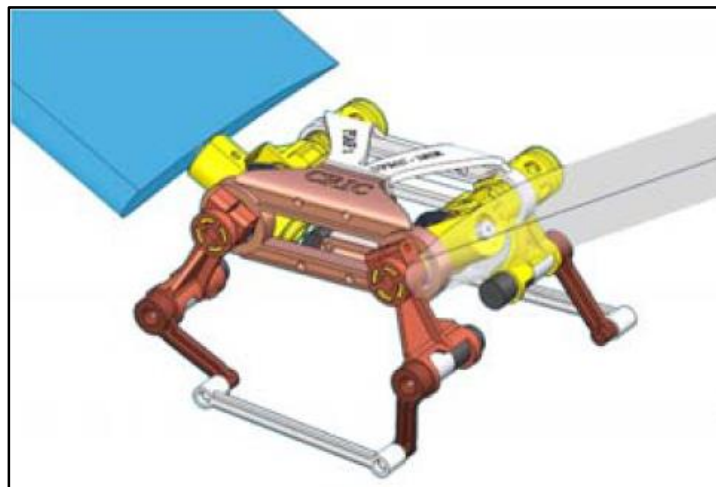


Figure 2. Schematic of a wing flapping mechanism for bird-sized UAVs [15].

The second category of the active wing morphing approach focuses on achieving desired wing kinematics by changing the wing shape during flight. There is limited work found in the literature that focus on active wing shape change for flapping wing unmanned air vehicles. Colorado et al. designed a 53 cm wing span bat-like micro air vehicle with morphing wings. Figure 3 shows the bio-inspired bat-like robot and its wings design [18].

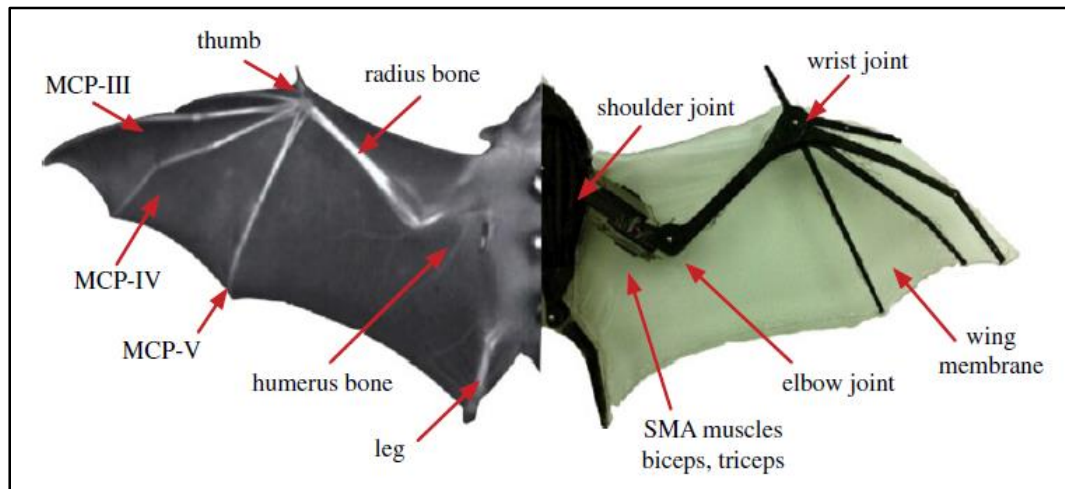


Figure 3. Bio-inspired bat-like MAV. The robot wings include shape memory alloy wires that enable wing folding [18].

Shape memory alloy wire acted as biceps and triceps and enabled the wing to fold and extend during the wing beat cycle to mimic the wing kinematics of a bat. The wing morphing system was successful in achieving the desired kinematics and was able to actuate the wing morphing at 2.5 Hz. The design however experienced fatigue issues. After 5 minutes of actuating the wings at 2.5 Hz, a performance reduction of 56% was noticed. The design was able to maintain actuation at the optimal frequency of 2.5 Hz for 1.5 minutes only.

1.2.2. Review of Passive Wing Morphing

The literature includes limited research in the area of passive wing morphing. There are only three research efforts listed that used a passive approach towards wing morphing in flapping wing UAVS. This section summarizes these three efforts.

The first effort was done by Demetgul et. al. [27]. In their paper, a simple wing planform was designed and tested. A segment of a rectangular wing that was made out of balsa wood was removed and replaced with a plastic sheet. The plastic sheet was held from one side only, so that the wing cutout section was exposed during the upstroke to reduce air resistance. During the downstroke, however, the plastic sheet covered the wing opening. The wings were fixed to a dynamometer and was flapped at 21 Hz. Figure 4 shows a schematic of the wing design, showing the areas of the wing that would be exposed during the upstroke. The authors did not state any conclusions about the effect of exposing and covering the wing cutout on the force the wing produced.

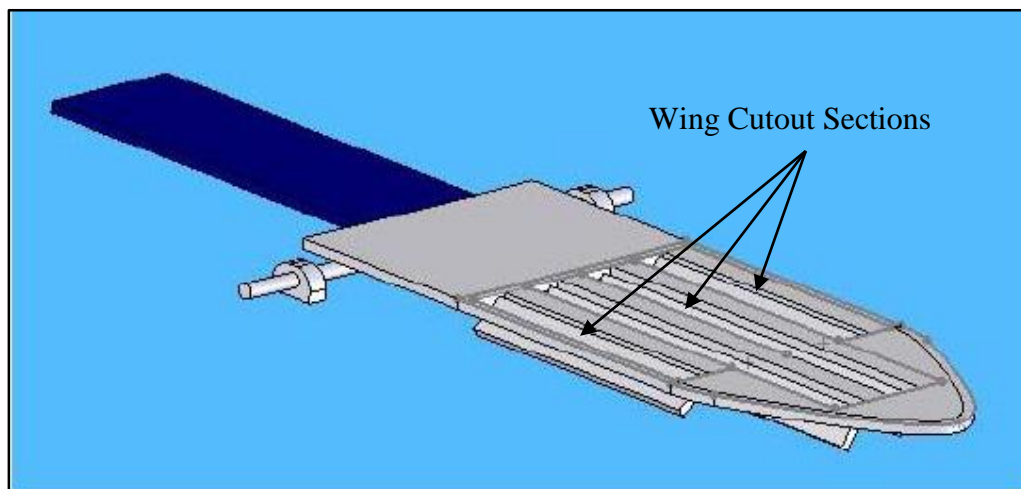


Figure 4. Schematic of wing design showing the sections, which would be exposed during the upstroke [27].

The second research in passive wing morphing in ornithopter was done by Billingsley et. al. [28]. In this effort, passive torsional spring was installed into the leading edge spar at the wing half span in order to exploit the advantages of wing surface area reduction during the upstroke. These springs were designed to deflect on the upstroke only and lock during the downstroke. Figure 5 shows the torsional spring.



Figure 5. Passive torsional spring that allow for bending only during the upstroke and locks during the downstroke [28].

Wing bending during the upstroke reduced the wing relative area (i.e., the wing area perpendicular to the flapping motion), which in turn mitigated the drag penalties and negative lift experienced by the test ornithopter during this portion of its wing beat cycle. The test ornithopter with the wings and the torsional springs were mounted on a six DOF load cell to measure the lift and thrust. The ornithopter was flapped at frequencies ranging from 3.5 Hz to 7.5 Hz. Figure 6 show snapshots of the morphing wing at mid upstroke and mid downstroke. The figure shows that the torsional spring allow for bending during the upstroke while it lock Results of Billingsely's experiment showed an increase in net lift, but they also showed that significant thrust penalties were incurred. These thrust penalties prohibited successful flight testing.

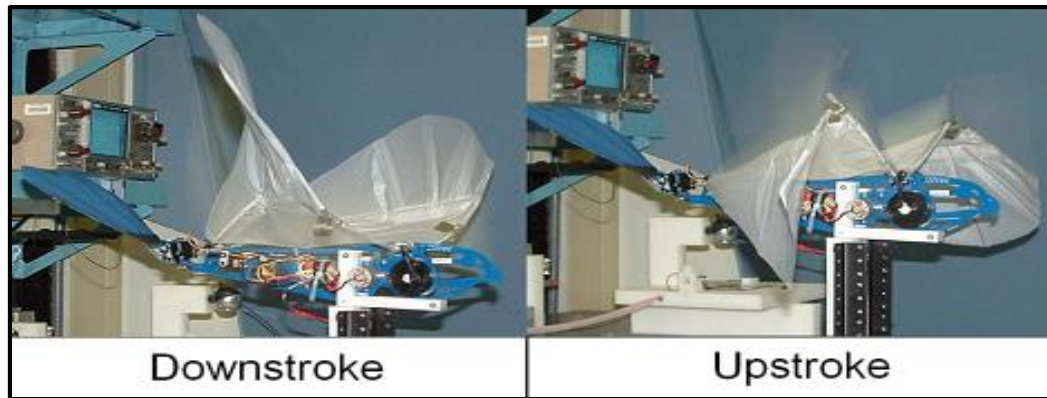


Figure 6. The morphing wing shape at mid downstroke (left) and mod upstroke (right) due to the presence of a passive torsional spring inserted at the wing half span [28].

The final and most extensive effort was done by Mueller et al [29]. In this work, three compliant hinges were designed. All joints allowed for bending during the upstroke only. Figure 7 shows a schematic of the three hinges. These hinges were inserted at 50% of the wing half span, as shown in Figure 8. The ornithopter with and without the hinges was mounted on a load cell where the lift and thrust could be measured and it was flapped at 5 Hz. Several configurations of the first two hinges were tested. The angles and cross sections of the hinges were determined arbitrarily. The solid hinge was tested with three angular ranges, namely 15, 25, and 35 degrees. The flexible Delrin hinge concept was fabricated with two wall thicknesses, namely 1.2 mm and 1.5 mm. Out of the three compliant hinge designs, only the compliant carbon fiber concept was the only one that could support flight. Also when comparing the lift and thrust produced by the ornithopter with the compliant hinges to the lift and thrust produced by the ornithopter with the continuous carbon fiber spar, it was observed that any lift gains achieved due to morphing were counteracted by thrust penalties.

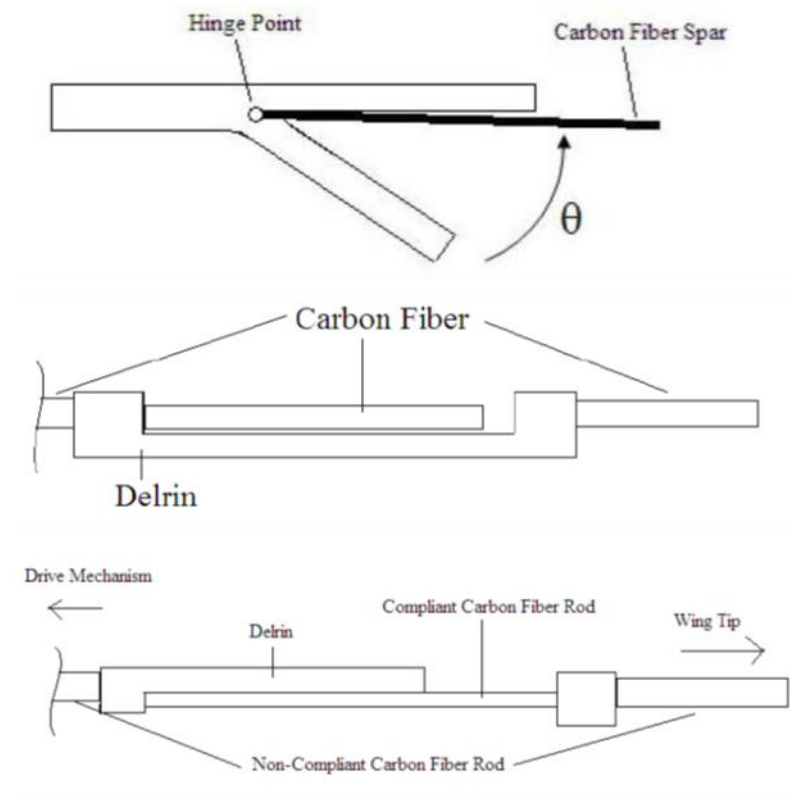


Figure 7. The compliant hinges designed to enable wing bending during the upstroke: (Top) solid hinge concept, (Middle) flexible Delrin hinge concept, and (Bottom) compliant carbon fiber hinge concept.

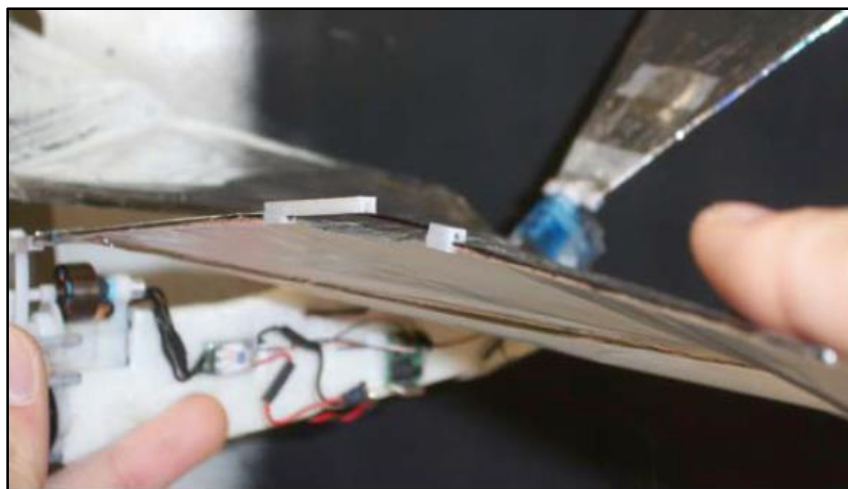


Figure 8. Morphing wing with compliant carbon fiber hinge at 50% of wing half span.

1.3.Current Research Goal, Hypothesis and Objectives

There is an obvious gap of knowledge when it comes to wing morphing of avian-size ornithopters. The goal of this work was to passively improve the wing performance of avian scale flapping wing UAVs using wing structural modifications during the wing beat cycle. A passive approach was selected because when compared to active approaches, passive mechanisms require no additional energy expenditure, while introducing minimal weight addition and complexity. According to Section 1.2.2, all of the previous passive wing morphing systems cited had one thing in common; they introduced lift gains but incurred thrust penalties.

The hypothesis tested in this work was that implementing a set of wing kinematics used by natural flyers using a passive approach and a compliant mechanism will improve the overall steady level wing performance of an avian scale flapping wing unmanned air vehicle. The steady level wing performance was defined as the horizontal and vertical propulsive forces produced by the wings over one flapping cycle. The hypothesis would be confirmed if the passive wing morphing system implemented in the ornithopter wing achieved the following objectives:

- Use a bio-inspired gait (CVG) to determine deflection design specifications for the compliant spine
- Improve the test vehicle wing performance with limited power, weight, and complexity penalties.
- Achieve lift gains without incurring thrust penalties

The remainder of this dissertation is aimed to testing and confirming the research hypothesis in order to achieve the above objectives and the research goal. Figure 9 shows the workflow of the research.

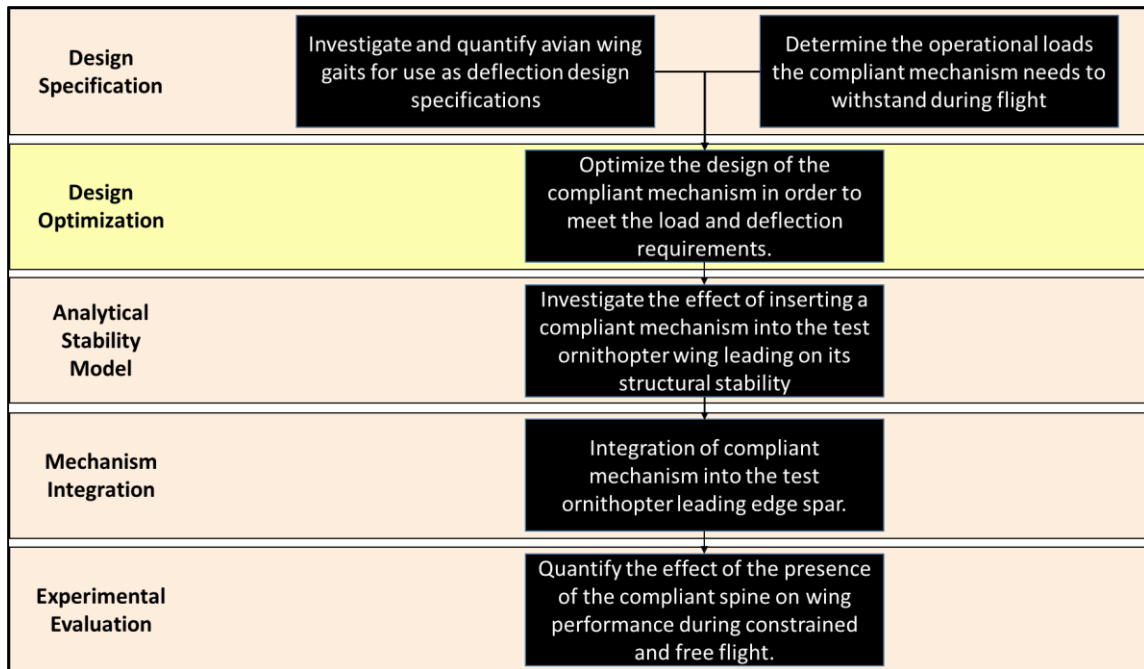


Figure 9. Research work flow chart

The Engineering Design and Optimization Group at Pennsylvania State University has deep expertise and resources in the field of compliant mechanism design optimization, thus the design optimization task of this research was allocated to them [30].

1.4. Dissertation Outline

This dissertation is composed of six chapters. A brief description of each of these chapters is given below:

Chapter one gives background on unmanned air vehicles, and classifies them according to scale and wing configuration. Fixed, rotary, and flapping wing unmanned air vehicles are compared and the need for flapping wing unmanned air vehicles is motivated. The need

for wing morphing is motivated and the various approaches to wing morphing is summarized. The chapter concludes by stating the current research goal, hypothesis and objectives.

Chapter two presents the description

n of the test platform. A review of avian wing morphology and wing kinematics is summarized. The bio-inspired technical approach taken towards identifying and quantifying the design specification for the passive wing morphing mechanism is discussed. The last section of the chapter, introduces the mechanisms that met the load and deflection design specification requirements. The approach by which these mechanisms are integrated in the leading edge spar is also shown in this chapter.

Chapter three introduces an analytical model of the leading edge spar with the passive morphing mechanism inserted in it. The model is then validated with experimental data and the structural stability of the model is then determined using analytical and graphical methods.

Chapter four presents the experimental evaluation of the test vehicle with its body is constrained to a load cell. The chapter shows a comparison between the steady level performance of the wing with and without the morphing mechanism inserted in the wings both in air and in vacuum. The vacuum test is used to isolate the aerodynamic effects from the inertial effects in order to determine the effect of wing morphing on both separately.

Chapter five details the free flight experimental evaluation of the test ornithopter. The chapter details the novel testing technique and introduced several performance metrics to evaluate the wing. The free flight test is used to compare the overall performance of the

wing with and without the morphing mechanism in free flight. The test is also used to better understand the body dynamics and flight physics of the vehicle.

Chapter six is the concluding chapter of the dissertation. It is used to summarize the research, state the original contributions to the field, and recommend future research areas.

Chapter 2: Technical Approach

This chapter discusses the technical approach taken to achieve the research objectives presented in Section 1.3. The chapter is divided into three main sections. The first section introduces the research platform. The second section discusses the bio-inspired approach used to achieve passive wing morphing using a structural modification called a compliant spine. The last section discusses the compliant spine design specifications, its properties and the optimization process used to implement the design.

2.1. Research Platform Description

The test platform that was used for this research was the commercially available Park Hawk. The Park Hawk is a radio controlled flapping wing un-manned air vehicle [31]. The test ornithopter had a 1.07 m wing span. This configuration was chosen for its stability, controllable flight behavior, and payload capability [6]. Additional test platform specifications can be found in Table 1. Figure 10 shows a picture of the vehicle. Because the main objective of this research was to improve steady level wing performance, determining the steady level flapping frequency was necessary. Previous experiments performed at the Morpheus Laboratory show that the steady level flapping frequency for the Park Hawk is between 4 to 5 Hz [6].

Table 1. Specifications for the Park Hawk test platform

Mass	Span	Max. Chord	Aspect Ratio	Flapping Rate	Speed	Wing Stroke Angle
425 g	1.07 m	0.28 m	4.97	4 – 6 Hz	2.5-8.5 m/s	1.17 rad



Figure 10. Park Hawk test Platform

Through the course of this research, the Park Hawk platform became unavailable and could not be purchased. Thus, it was decided to design and fabricate a custom built test platform that was similar to the Park Hawk. The new test vehicle design will be referred to as the ML101 design for the remainder of this document. Figure 11 shows a picture of the new test vehicle. ML101 has the same specifications listed in Table 1 and thus is an adequate replacement for the Park Hawk in the experiments. However, structural changes were implemented on the new platform to overcome some of the weaknesses that were found in the Park Hawk. These design changes include:

- Changing the Fuselage material from Garolite (a glass fiber epoxy layup) to a stronger, lighter and stiffer carbon fiber epoxy lay-up
- Adding lightening holes near the tail and material was added near the gear train in order to change the body second moment of inertia, as flexibility in the **Park Hawk** model caused the gears to grind against each other, causing the gears to break at the higher frequencies
- Changing the design of one the fuselage side fairings to improve the vehicle's flexural stiffness, without adding weight.

- Standardizing all the screws on the ornithopter making it easier and faster to assemble.
- Improving the design of the drive axel to include less moving parts.

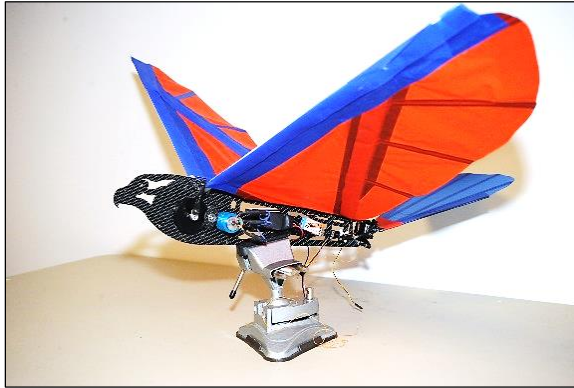


Figure 11. ML101 test platform

For both the Park Hawk and the ML101 test platforms, the wings design was identical. The wings consisted of a nylon rip-stop membrane stretched over several carbon fiber spars referred to as fingers. There were two main spars in each wing. The first one was at the leading edge and the second one was placed diagonally from the leading edge to the rear of the fuselage. Each spar was held in place by a Dacron tape pocket to add stiffness and durability. Figure 12 shows a top view of the wing with the spars labeled.

Due to the flexibility of the membrane, the wing shape varied significantly during flapping. Figure 13 shows a high speed photo sequence of the wing beat cycle. This flapping sequence shows the downstroke on the left and the upstroke on the right in a counterclockwise circle.

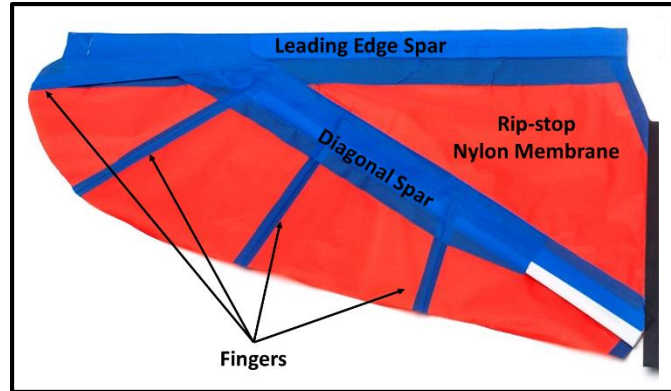


Figure 12. Top view of the test platform wing showing the nylon membrane, the finger spars and the leading edge and diagonal spars

The Park Hawk test vehicle was used for the preliminary constrained flight testing as discussed in Section 4.1, while the ML101 test vehicle was used for the constrained flight tests performed in vacuum and discussed in Section 4.2, as well as the flight tests discussed in Chapter 5.

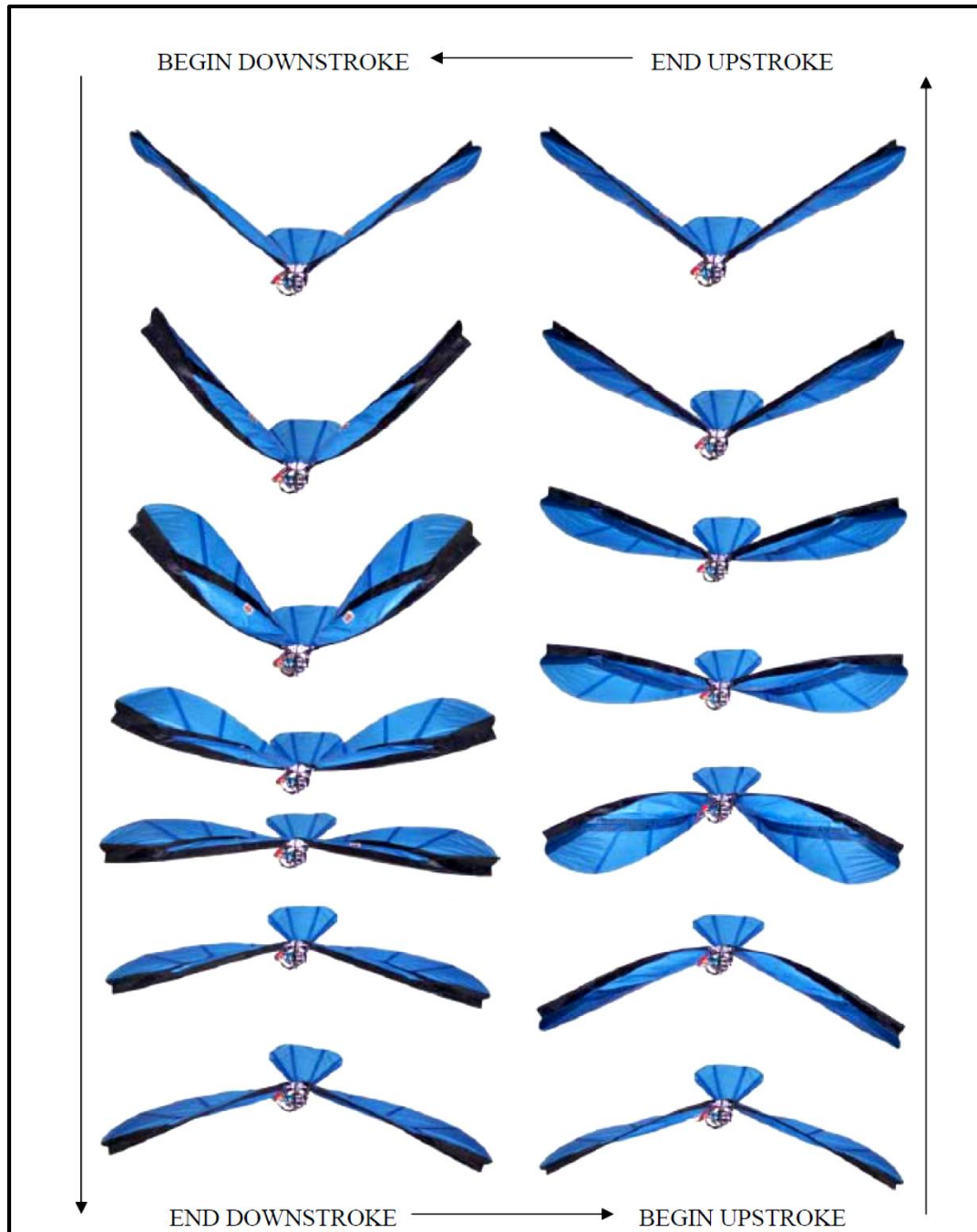


Figure 13. High speed photography of the stroke cycle. Downstroke is presented on the left column, starting at the top of the figure and ending at the bottom. Upstroke begins at the bottom of the right column and continues to the top of the right column [6].

2.2. A Bio-inspired Passive Approach to in Flight Wing Morphing

As mentioned in Section 1.2, several approaches can be used to achieve wing morphing. A passive approach was chosen for this research because when compared to active morphing, passive morphing mechanisms require no actuation, energy expenditure, minimal weight addition and a significant reduction in complexity. From Billingsely et. al., it was concluded that more sophisticated wing kinematics are required when morphing in order to maintain the lift gains achieved while mitigating thrust penalties [28]. The goal here was to mitigate the inefficient kinematics, shown in Figure 6, and focus on achieving efficient, tailorable kinematics.

This section is divided into two main sub-sections. The first sub-section discusses avian wing morphology and flight kinematics. The second sub-section discusses the avian wing kinematics chosen for the current research and the design specifications for the compliant mechanism used to achieve wing morphing.

2.2.1. Avian Wing Morphology and Flight Kinematics

2.2.1.1. Avian Wing Morphology

Morphology in biology is defined as the study of the form and structure of a plant or animal or any of its parts. In this section, the morphology of bird' wings is discussed briefly. A detailed description of bird' wing geometry, internal, and external structures can be found in [32]. Bird wings include three major joints: the shoulder, elbow, and wrist. The shoulder joint connects the wings to the body, where the main flight muscles exist, thus allowing for the up and down flapping motion. The elbow and wrist joints allow the avian wing to flex and extend during the up and down strokes. Avian wings can be divided into two sections, the inner section, which is referred to as the arm wing and the outer section,

which is referred to as the hand wing [32]. Figure 14 shows the hand and arm wings for five different birds [33]. In the figure, the wings were scaled so that the hand wing were equal in order to illustrate the proportional size of the hand wing to the arm wing. From the figure, it is clear that the relative dimensions of the hand and arm wings differ among bird species. These differences provide insight into the functions of the arm and hand wings, as well as the flight characteristics of each species. The hand wing in primarily soaring birds (e.g. Albatrosses) occupy about 40% to 45% of the wing total length. While for more agile species, the hand wing can occupy up to 80% of the wing total length (e.g. Hummingbirds) [32].

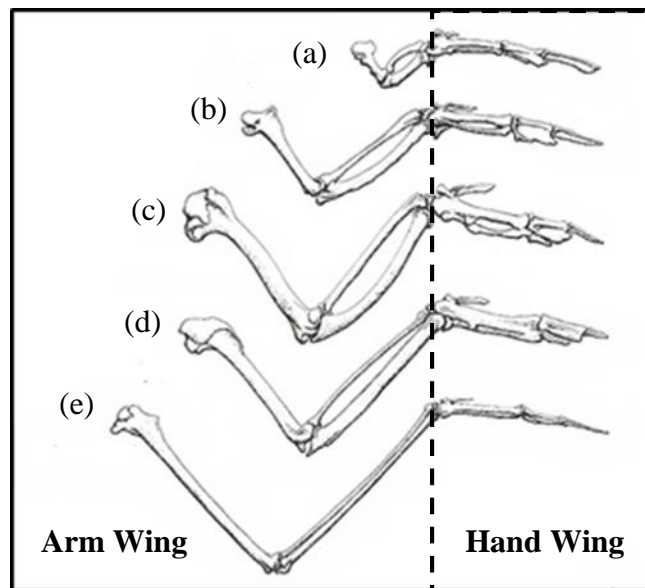


Figure 14. Relative dimensions of the hand wing to arm wing for five species: a) Calliope hummingbird; (b) Rock dove; (c) Blue grouse; (d) Starling; (e) Albatross [33].

The wing Aspect Ratio (AR) is another geometric parameter that provides insight into flight performance. AR is defined as the wing span divided by the wing area. The AR is large for birds with long narrow wings such as the albatross (AR=14) and it is small for birds with short broad wings such as Pheasants (AR=5). Figure 15 shows a picture of an

albatross and a pheasant in order to contrast their wing AR. In general, birds with higher AR are fast and low drag gliders, while birds with small AR are slow gliders but are good at complex maneuvers at short range.

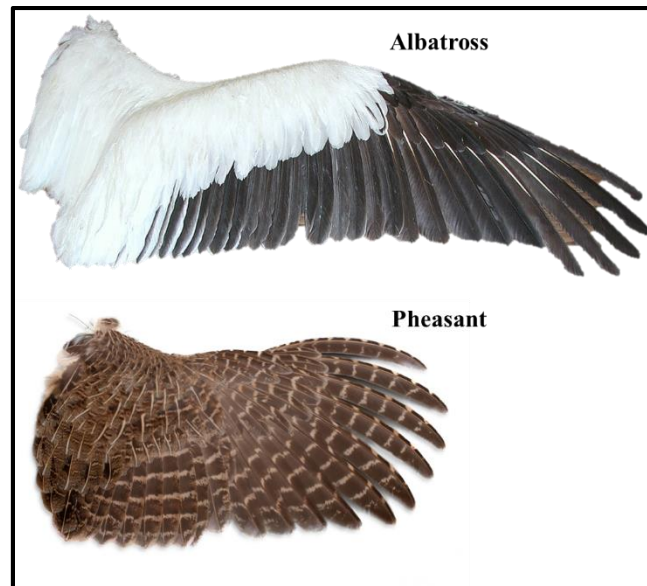


Figure 15. Wings of an albatross and a pheasant showing the difference in aspect ratio. Albatross has an AR of 14 while the pheasant has an aspect ratio of 5.

2.2.1.2. *Avian Wing Kinematics*

The main purpose of a bird's wing is to produce lift and thrust. Birds generate lift by accelerating masses of air downwards and generate thrust by accelerating air backwards [32]. A bird with a fully extended wing and without flapping may be fully capable of supporting its own weight but would only glide while losing altitude. Flapping is necessary because it is the mechanism birds use to maintain steady level flight by producing lift alone [34, 35]. In other words, the lift produced by a bird during flapping is used for both weight support and thrust generation to balance. Various avian species use different wing kinematics to produce the required lift and thrust for flapping flight. Biologists classify wing flapping kinematics, also referred to as gaits, into two main gaits depending on the shape

of the wake visualized behind the wings during flight. The first gait is the Vortex Ring Gait (VRG). Based on several wake visualization experiments, a closed vortex ring is produced during each downstroke of the vortex ring gait, while the upstroke hardly contributes to the wake [36, 37, 38]. Figure 16 shows an interpretation of the wake behind a chaffinch flying at a slow speed through clouds of wood and paper dust [38]. The figure shows the vortex rings that are formed during the downstroke. It also shows that the upstroke does not form vortex rings but it drags the paper dust upwards.

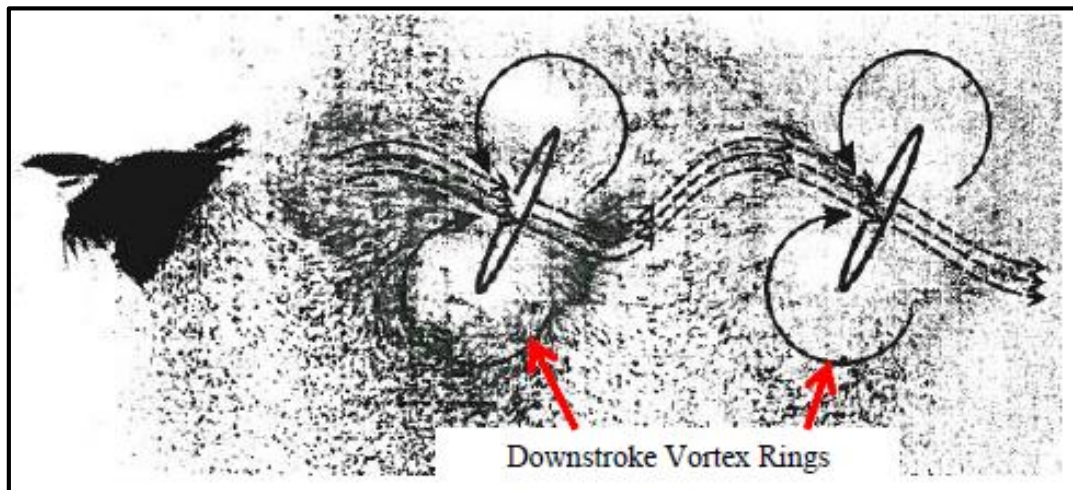


Figure 16. Interpretation of the vortex ring gait wake structure behind a chaffinch in flapping flight [38].

The second gait is the continuous vortex gait (CVG). This gait was discovered in birds by Spedding in 1987 when he studied the wake of a kestrel flying at a cruise speed of 7 m/s [39]. Spedding discovered that the wake structure did not look like separate vortex rings but rather a continuous pair of trailing vortices with constant circulation. Figure 17 shows the interpretation of the wake structure behind a kestrel flying at a cruise speed of 7 m/s. The figure shows tip vortices being shed continuously and that the vortices are following

the wing tip path. Figure 18 shows a schematic of the top view of both the vortex ring and the continuous vortex gait's wake structure.

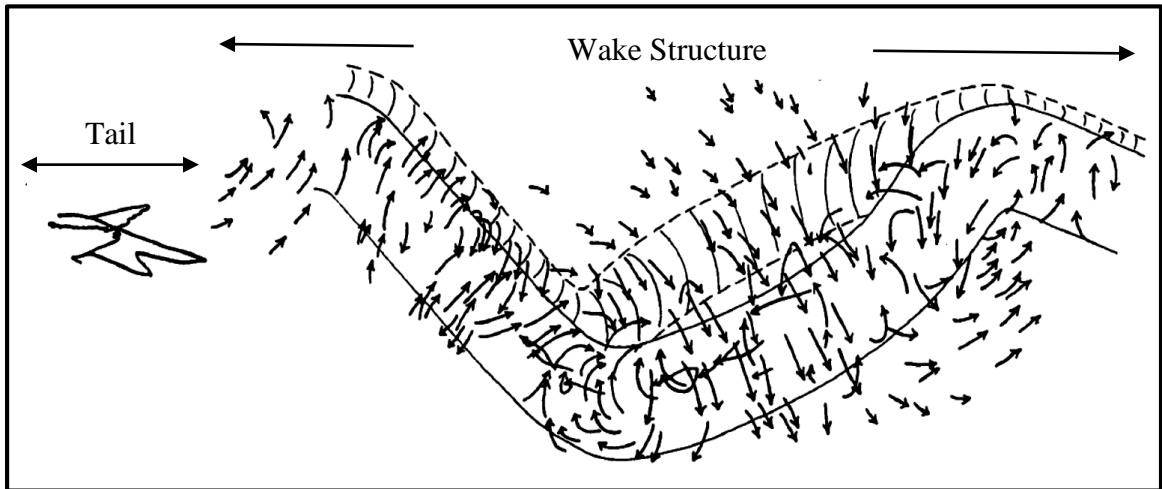


Figure 17. Interpretation of the continuous vortex gait wake structure behind a chaffinch in flapping flight [Adapted from [39]].

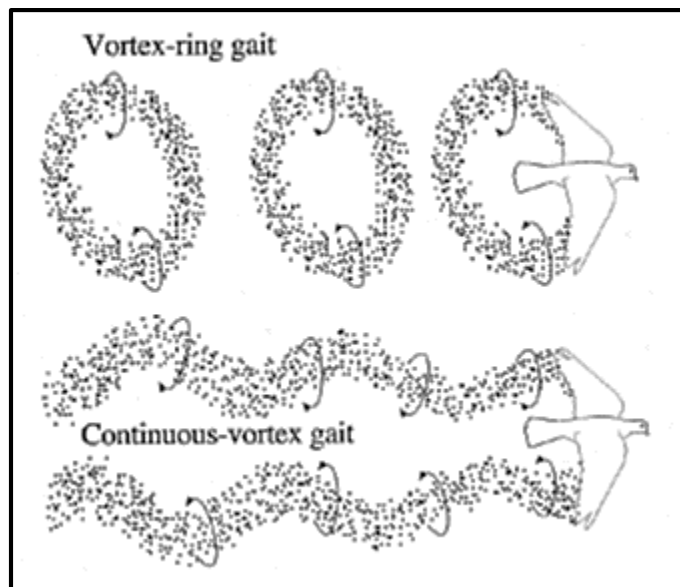


Figure 18. Top view of the vortex ring gait (top) and continuous vortex gait (bottom) wake structure of flapping birds. [Adapted from [34]]

Several researchers and biologists have tried to classify species using these flight gaits. Research showed that one species may change from one gait to the other depending on its

flight speed, while others may use the same gait for all flight speeds [40, 34]. Rosen et al. trained a thrush nightingale to fly at steady level with speeds between 4 m/s to 11 m/s. The wake structures of the nightingale changed gradually with increased speed. At 4 m/s, the nightingale had a vortex ring gait wake structure, which gradually changed to a continuous vortex gait structure at higher speeds [41]. Research done by Tobalske and Dial showed that a magpie for instance used the vortex ring gait for flight speeds ranging from 4 m/s to 14 m/s [42]. Although it had not been fully understood, several factors determine which gait a given species will use during given flight conditions. Gait selection depends highly on both the flight speed and the wing morphology [40]. Aspect ratio is one of the important wing morphology properties that research showed affect gait selection. Bird species with broad wings and low aspect ratio, such as the magpies, tended to use a vortex ring gait at all speeds. Species with larger aspect ratios transitioned among flight speeds using a vortex ring gait at slow speeds and a continuous vortex gait at higher speeds [43]. The transition speeds for most species, compared in the literature, occurred between 7 to 10 m/s [44]. Figure 19 illustrate the effect of wing morphology and flight speed on gait selection by birds and bats in flapping flight [35].

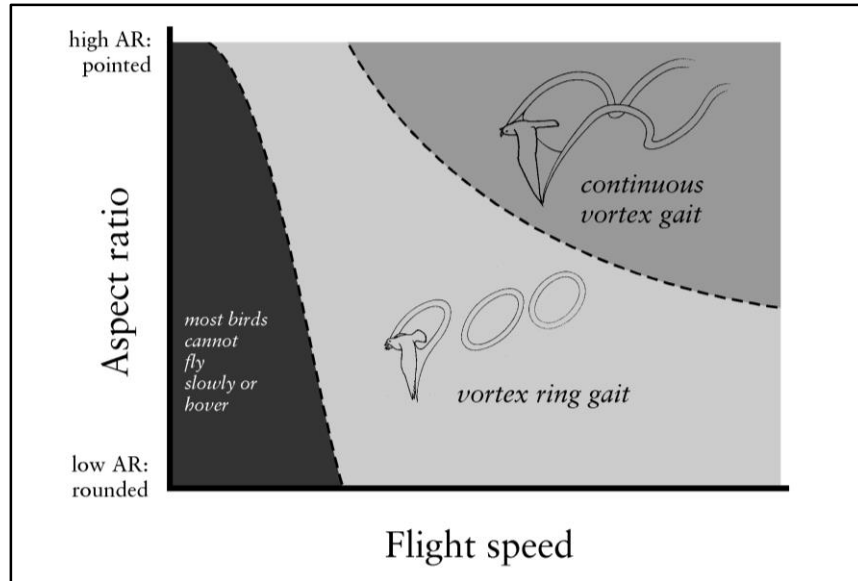


Figure 19. Illustration of the effect of Aspect Ratio and flight speed on gait selection in birds [35]

The upstroke wing kinematics used to achieve one of the two wake structures discussed above are different, while the downstroke kinematics are similar [43]. During the downstroke of all gaits, the wings are fully extended and they move downwards and forwards. The lift vector is therefore inclined forward and pointed upwards providing both weight support and thrust. The downstroke portion of the wing beat cycle is considered the power stroke and keeping the wings fully extended during the downstroke allows for the maximum production of lift and thrust. During the upstroke, if the wing maintains a positive angle of attack with the relative flow, it can still generate lift for weight support but this lift is accompanied by drag. Therefore, the upstroke and the downstroke have to be asymmetric in order to ensure the production of a positive mean net thrust [40]. Figure 20 shows the vertical and horizontal force vectors produced by a wing at a positive angle of attack during flapping.

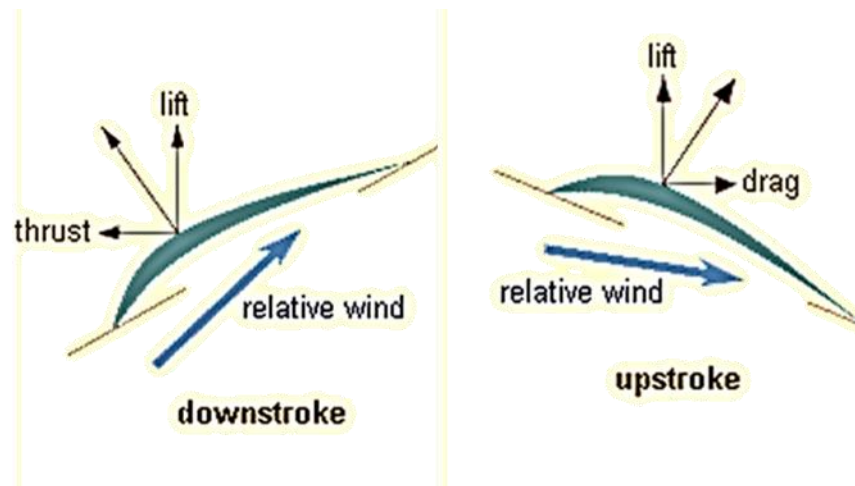


Figure 20. Vertical and horizontal forces produced during the downstroke and upstroke of a flapping wing beat cycle.

As mentioned earlier, the upstroke kinematics vary between the various wing gaits. The upstroke kinematics of the vortex ring gait are more pronounced and can be classified into two types of upstroke: a tip reversal upstroke and a feathered upstroke. During the tip reversal upstroke, at mid upstroke the wrists are held above the body and adducted and the hand wings are supinated (rotated upwards). The amplitude of the wing beat angle may approach 180 degrees and a side view of the wingtip path shows a figure eight pattern. During the feathered upstroke, the entire wing is folded and the wing feathers may take the shape of a “venetian blind”. The side view of wing tip path is elliptical [34]. The third and final type of upstroke is the continuous vortex gait. During this gait, the wings are not folded close to the body, but only the feathers are flexed and closed up parallel to the airflow. Figure 21 shows a top view of a pigeon’s wings flying in a variable speed wind tunnel [34]. Figure 21A shows the wing shape a mid downstroke. Figure 21B shows the wing shape at mid upstroke of a vortex ring gait with tip reversal upstroke kinematics. Figure 21C shows the wing shape at mid upstroke of a vortex ring gait with feathered

upstroke kinematics. Figure 21D shows the wing shape at mid upstroke of a vortex ring gait upstroke kinematics.

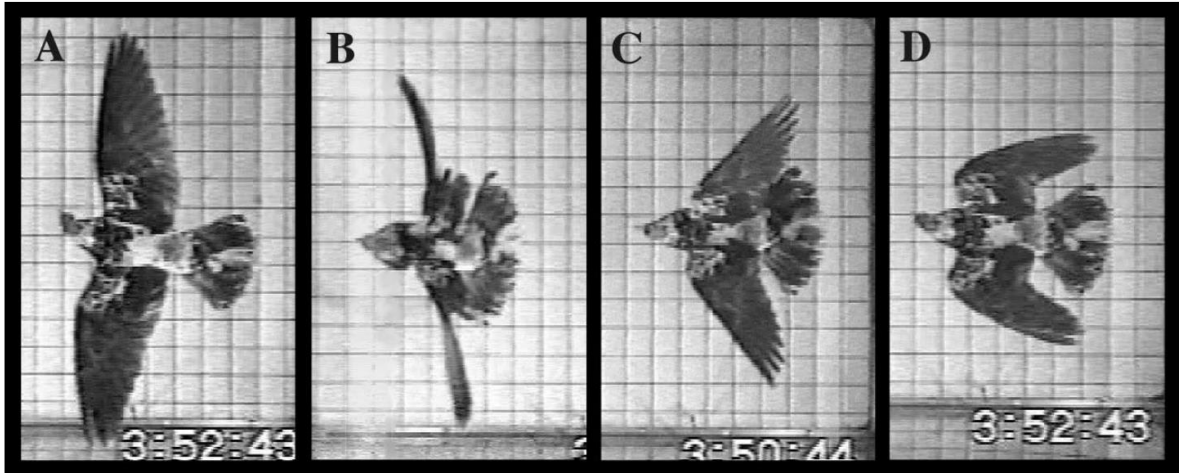


Figure 21. Top view of a pigeon's wing flight in a variable speed wing tunnel showing the wing kinematics at: A) mid downstroke, B) mid upstroke of a vortex ring gait with tip reversal upstroke C) mid upstroke of a vortex ring gait with feathered upstroke kinematics, and D) mid upstroke of a continuous vortex gait upstroke. [Taken from [34]]

Figure 22 shows the side and top views of the wingtip and wrist paths of a pigeon during a tip reversal upstroke vortex ring gait, a feathered upstroke vortex ring gait, and a continuous vortex gait.

It is clear from the figures and discussion above that the upstroke kinematics for the tip reversal and feathered upstroke are more complex and they require a larger range of motions in all of the wings joints when compared to the continuous vortex gait upstroke kinematics. Even though nature achieves the continuous vortex gait upstroke kinematics by flexing and folding the feathers, these kinematics can be achieved on the test ornithopter as described in Section 2.1 by articulating one mechanism at the location of the avian wrist. Figure 23 shows that the continuous vortex gait kinematics could be achieved by slightly bending, twisting and sweeping the bird's wrist during the upstroke. The front view in

Figure 23 shows the wing bending, the side view shows that wing twist, and the top view shows the wing sweep at mid downstroke (left) and mid upstroke (right). A detailed discussion of the kinematics of CVG can be found in [34], [39], and [42].

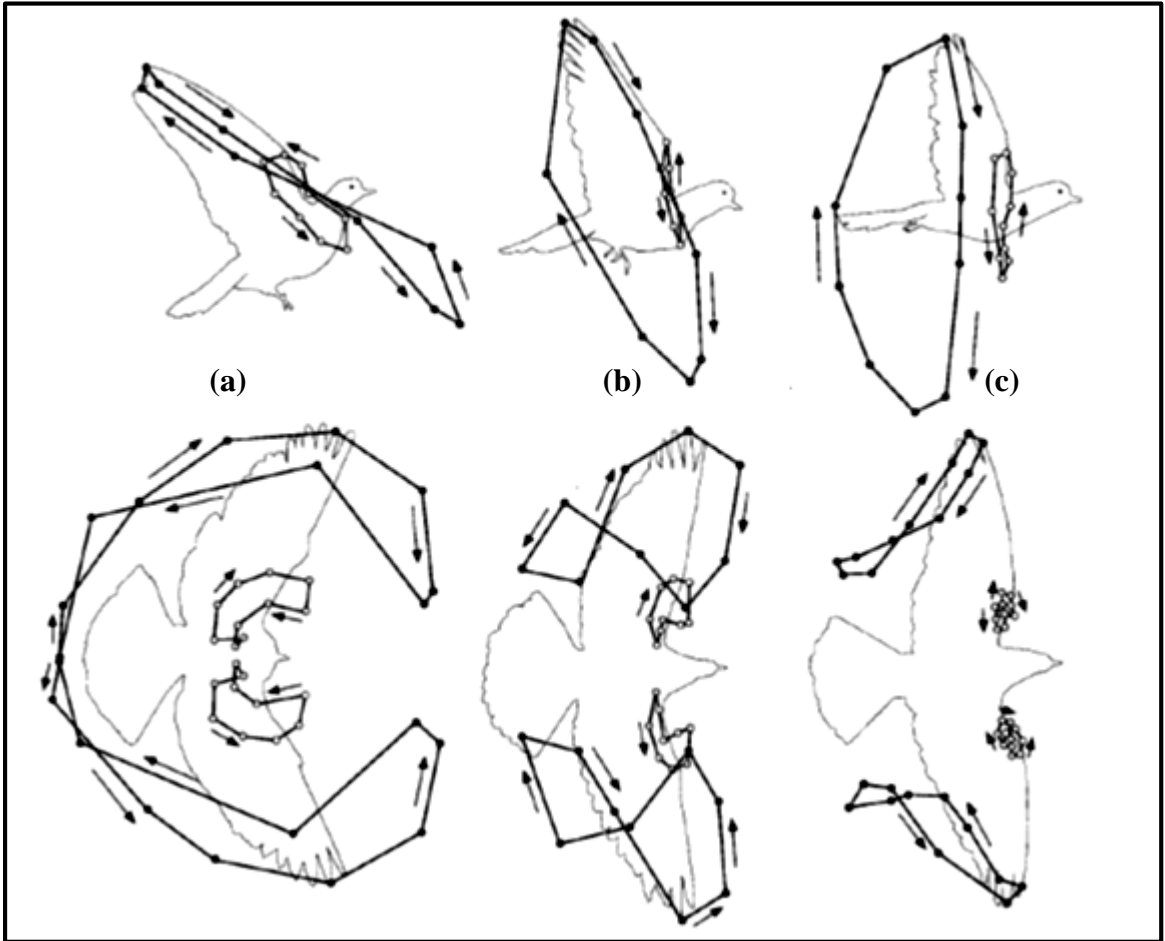


Figure 22. Side and top view of the wingtip and wrist paths of a pigeon during (a) a tip reversal upstroke vortex ring gait, (b) a feathered upstroke vortex ring gait, and (c) a continuous vortex gait [Adapted from [34]].

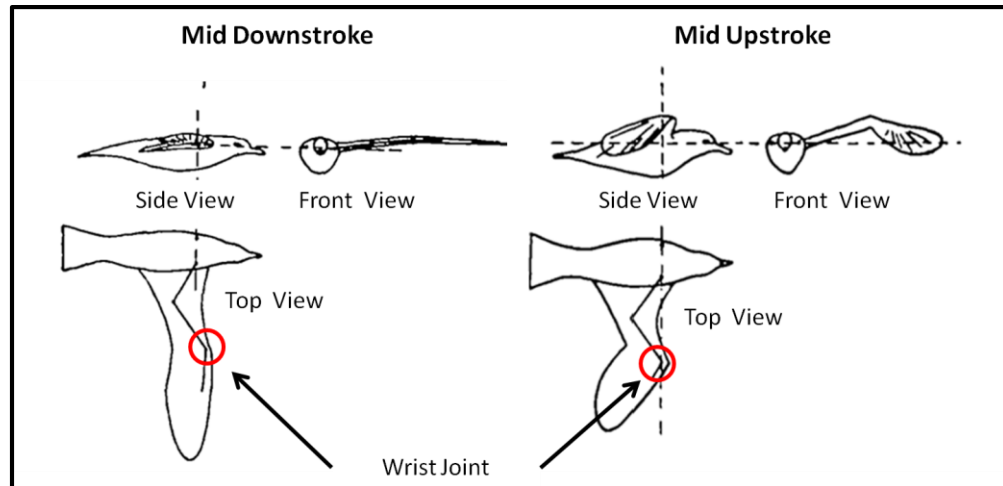


Figure 23. During the continuous vortex gait the wings are fully extended at mid downstroke (left) and out of plane bent, twisted and swept at mid upstroke (right) [Adapted from [45]].

2.2.2. Continuous Vortex Gait Design Specifications

The Continuous Vortex Gait was chosen as the desired set of wing kinematic to be implemented on the test ornithopter for several reasons. Not only is it the gait used by birds that have similar Aspect Ratio and steady level flight speed as the test vehicle, but it is also one of the only gaits that can be achieved passively. The CVG can be achieved passively because it requires motion in only one major joint, namely the wrist.

As mentioned before, in order to implement the CVG, a 3DOF motion is required, namely bending, sweep and twist. The focus of this research, however is using a compliant spine (CS), which is a 1 DOF compliant mechanism that allows for bending only, to achieve passive wing morphing.

The compliant spine was inserted at 37 % of the wing half span to mimic the function of an avian wrist, which is the major joint responsible for the CVG kinematics. Figure 24 shows a schematic of the compliant spine and its location along the leading edge spar of an ornithopter. The compliant spine had to fit in a box with a length of 63.5 mm, a width

of 6.3 mm and a depth of 6.3 mm in order to fit inside the pocket of the leading edge spar. The design and optimization procedure for the compliant spine must consider the loads that the spine experiences and the deflections that it needs to realize must be determined.

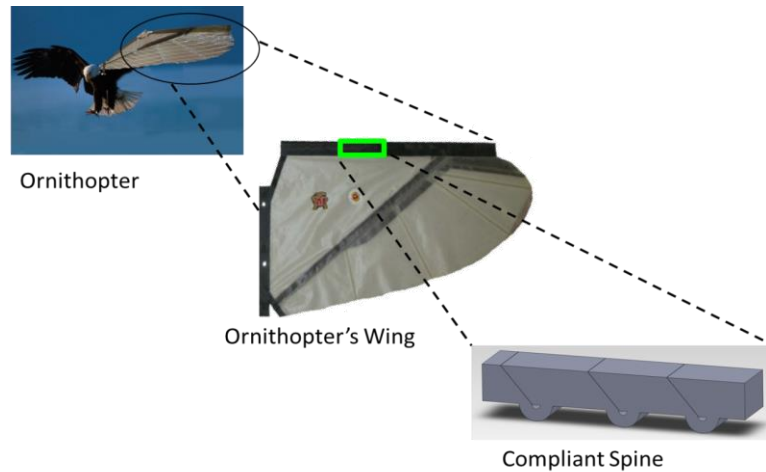


Figure 24. The compliant spine is inserted into the leading edge spar to mimic the function of an avian wrist

This section discusses the methods used to measure the loads that the compliant mechanism responsible for morphing would experience during flapping and the deflection requirements that the mechanism had to meet during both the up and downstrokes. These requirements provided the input to the design and optimization process described briefly in Section 2.3 and in detail in [20] and [46] through [47].

2.2.2.1. Compliant Spine Load Specifications

The strains experienced by the CS during steady level flight were measured experimentally using strain gages. Two CEA-06-125UN-120 Vishay® strain gages were mounted on the leading edge spar, with their centers at the locations where the compliant spine root and tip are located, namely 19.75 cm and 26.1 cm from the wing root. Figure 25 shows the strain gages mounted on the wing leading edge carbon fiber spar. The strain

gages were connected to a Vishay® 3800 strain indicator and the spars were inserted in the test ornithopter wing. The ornithopter was flapped at 5 Hz, a typical steady level flight flapping frequency. Figure 26 shows the experimental set-up.



Figure 25. Strain gages mounted on the leading edge spar at the location of the compliant spine root and tip

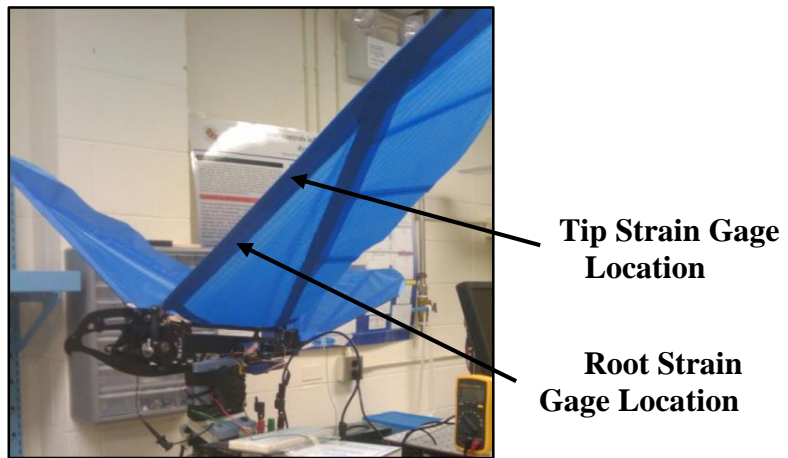


Figure 26. Experimental set-up for measuring the strains at the locations of the compliant spine root and tip at a flapping frequency of 5 Hz.

The strains at the root and tip locations were recorded for several flapping cycles. Figure 27 shows the strains measured over one flapping cycle. In the figure, the x-axis is t/T , which is the time, t , normalized by the flapping period, T . The normalized time parameter, t/T is zero or one at the downstroke/upstroke transition point and is 0.54 at the

upstroke/downstroke transition point. The strain measured from the strain gage at the location of the root of the compliant spine is noted as the inboard strain, and the strain measured from the strain gage at the location of the tip of the compliant spine is noted as the outboard strain.

A critical design point is shown in Figure 27 and occurs at the upstroke-downstroke transition point ($t/T=0.54$), where the maximum relative strain that the spine experiences occurs. The maximum strains recorded for the inboard and outboard strain gages were -1975.4 $\mu\epsilon$ and -1317.4 $\mu\epsilon$, respectively. After determining the maximum strains experimentally, the same spar was modeled in ANSYS under steady state dynamic loading at 5 Hz [20]. Assuming a uniform load distribution on the leading edge spar, the applied load was increased incrementally during the simulation until the resulting strains at the locations of the compliant spine root and tip matched the measured strains. Table 2 shows the experimental and simulated strains recorded at the locations of the compliant mechanism root and tip. During the optimization, the compliant spine was assumed to withstand about 10 Newton's [20, 46]. This load value was calculated by conservatively assuming that the compliant spine carried the load experienced by the leading edge spar from the root location of the root of the mechanism to the wing root.

Table 2. Experimental and Simulation Strains recorded at the locations of the compliant mechanism root and tip [Adapted from [20]].

Data Type	Maximum Root (Inboard) Strain [$\mu\epsilon$]	Maximum Tip (Outboard) Strain [$\mu\epsilon$]
Experiment	-1975.4	-1317.4
Simulation	-1982.8	-1263.6

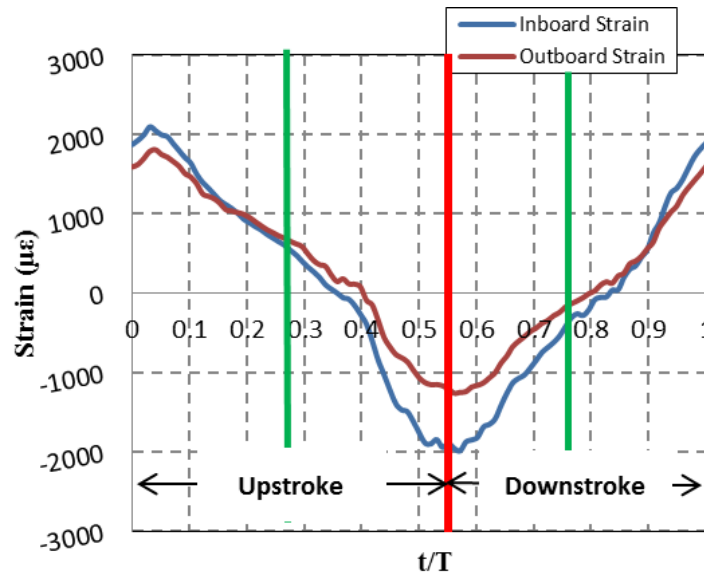


Figure 27. Inboard and Outboard Strains at the Location of the Compliant Spine Root and Tip

2.2.2.1. Compliant Spine Bending Deflection Specifications

After establishing the maximum load requirement that the compliant spine would have to withstand during steady level flight, the next step in the CS design process was to determine the bending deflections, which the spine had to realize in order to mimic the bending kinematics of the CVG. A video of a Cockatiel flying in a wind tunnel was used to extract the required deflections [48, 49, 50]. Figure 28 shows nine lateral views of the Cockatiel during one wing beat cycle. Matlab’s image processing toolbox was used to extract the wingtip sweep and bending deflections from the images. The wingtip bending deflections were assumed to be linearly related to the deflections that the tip of the compliant spine must realize in flight over the flapping cycle. Using the wing geometry and the location of the compliant spine, a scaling factor was calculated to be 0.189. Hence, the required bending deflection at the tip of the compliant spine at mid upstroke and mid downstroke are 8.42 mm and 0.6 mm, respectively

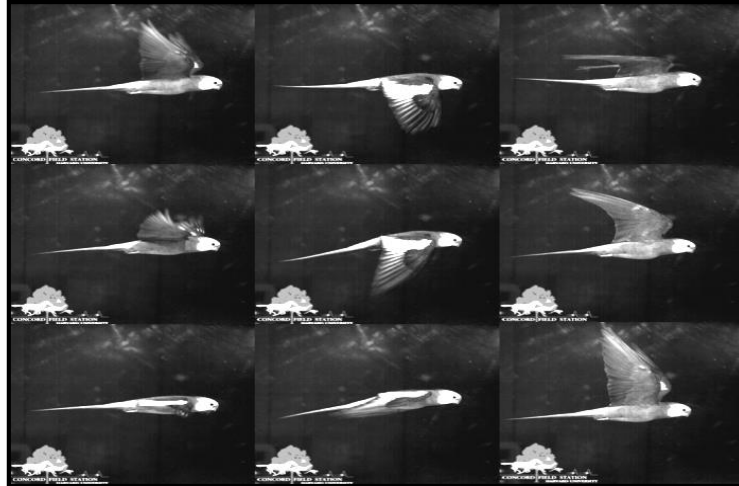


Figure 28. Lateral Flapping Sequence for a Cockatiel in a Wind Tunnel

In summary, the compliant spine had to be designed to withstand a maximum load of 10 N and the mechanism tip had to bend 8.42 mm at mid upstroke but only 0.6 mm at mid downstroke. The next section discusses the required compliant spine stiffness characteristics and introduces the compliant spine designs that were tested during this research as well as their loading and boundary conditions.

2.3. Compliant Spine Design

The compliant spine (CS) is a novel, monolithic, nonlinear contact-aided compliant mechanism. Compliant mechanisms have numerous advantages over rigid-link mechanisms. They are easy to manufacture and lower cost than their rigid link counterparts because they are usually monolithic in nature. During the upstroke, the compliant spine must allow the wing to morph in the bending direction. During the downstroke, it must become stiff, mimicking a rigid spar. A schematic illustrating the desired stiffness of a compliant spine compared to the rigid spar and to a torsional spring is shown in Figure 29(a) [47]. In Figure 29(a), the y-axis represents the forces during a flapping cycle, F , and the x-axis represents the compliant spine tip bending deflection, Z -deflection. As

illustrated, the desired stiffness of the compliant spine is nonlinear. It is stiff in the downstroke, similar to that of a rigid spar, and flexible in the upstroke, similar to a torsional spring. Figure 29(b) shows a CS design with three compliant joints. Note that this design is flexible in bending during upstroke because of the compliance of the semi-circular compliant hinges, and it is stiff in bending during downstroke because the slanted faces come into contact with one another.

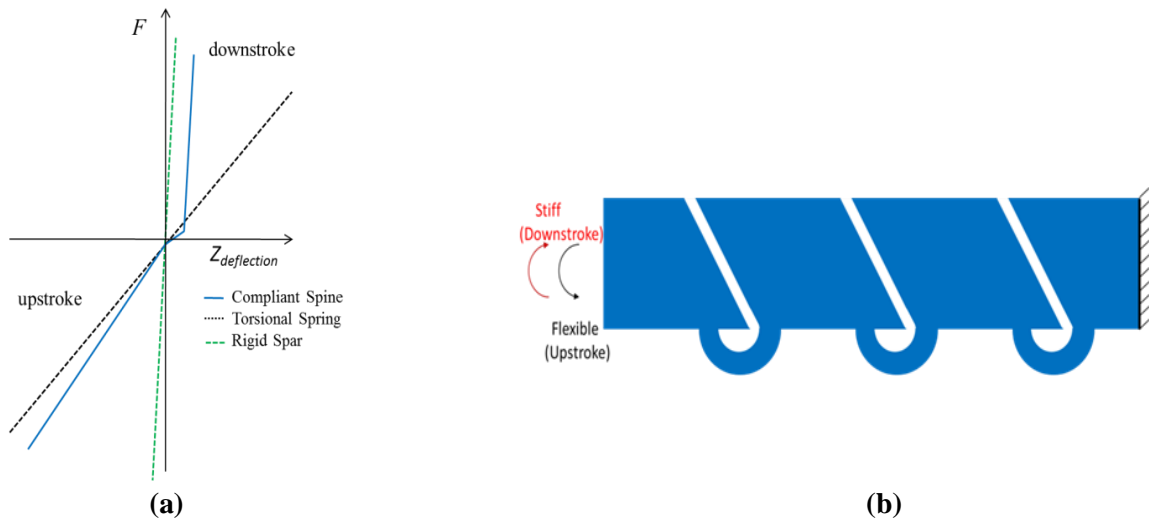


Figure 29. (a) The desired stiffness of the compliant spine is nonlinear. The Y-axis represents the forces during a flapping cycle and the X-axis represents the compliant spine tip bending deflection (b) Schematic of a compliant spine with three compliant joints.

The shape of a single compliant hinge was designed using a quasi-static multi-objective optimization problem described in [47]. The objectives of this optimization problem were to minimize the mass of the hinge, the error in bending deflection as compared to the desired bending deflection, and the error in maximum stress compared to the maximum allowable stress. The parameters that affect the performance of the compliant spine were the number of compliant joints and the shape of each compliant joint. The design parameters that affect the joint's stiffness during the upstroke were related to the shape of

the compliant hinge, while the design parameters that affect the downstroke stiffness were related to the geometry of the contact surfaces. This initial phase of design yielded a three compliant joint spine that was tested during preliminary constrained flight testing. Constrained flight testing was useful because even though the vehicle's dynamics are restrained, this type of testing allowed for the direct measurement of the integrated vertical and horizontal forces produced by the vehicle. The experimental setup and results are discussed in Sections 4.1.1 and 4.1.2, respectively

An optimization procedure involving steady state dynamic analysis was then performed on compliant spines with more than one compliant joint [46]. This procedure yielded a family of designs that met the requirements for maximum von-Mises stress, and desired wing bending deflections. Thus several compliant spines were tested during constrained and free flight tests. Figure 30 shows all compliant spine designs tested and their predicted stress distribution at mid upstroke [20]

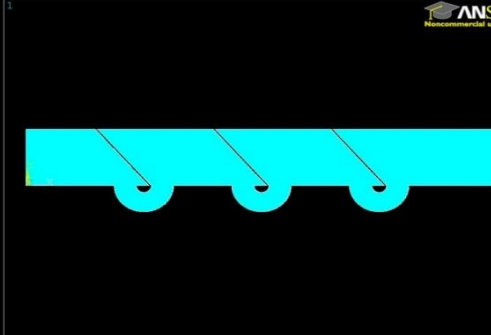
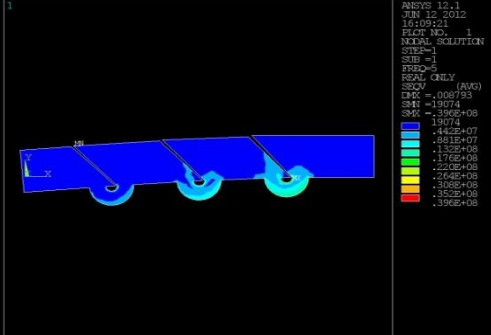
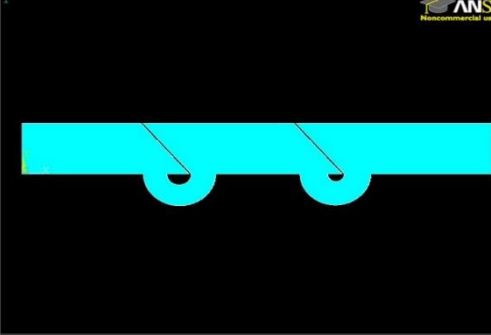
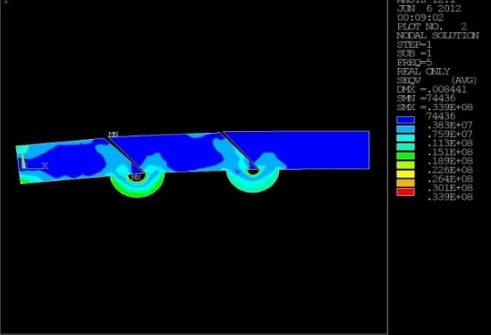
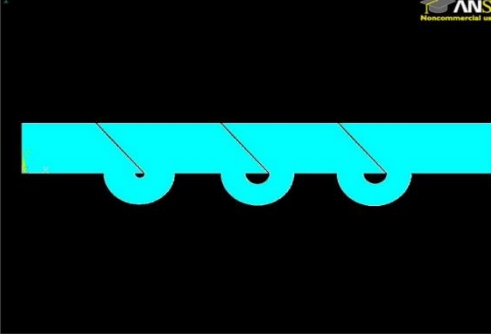
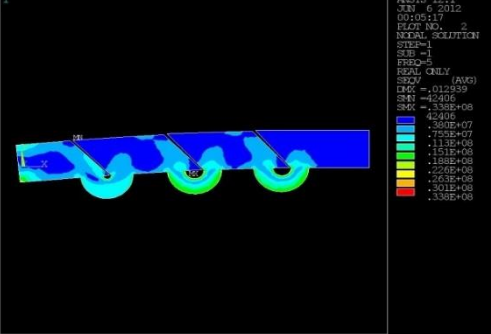
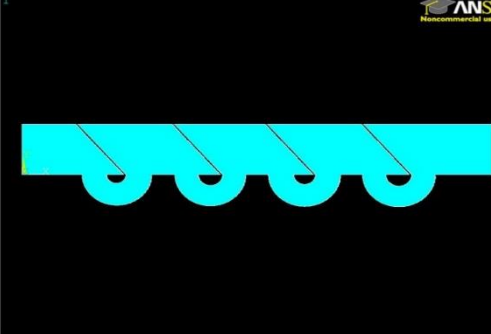
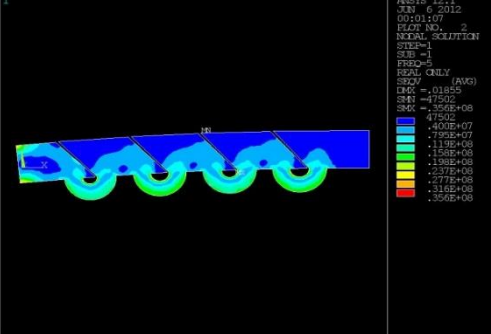
CS Design Name	CS Design Geometry	CS Design Von-Mises Stress Distribution
Comp 4TL		 <pre data-bbox="1328 321 1430 527"> ANSYS 12.1 JUN 12 2012 00:09:21 ELEM NO. 1 NODAL SOLUTION STEP=1 SUB =1 FREQ=5 REAL ONLY SCY (AVG) CMX =.008793 SMN =-19274 SMX =.396E+08 19274 442E+07 .831E+07 -1.52E+08 -1.76E+08 -2.22E+08 -2.64E+08 -3.39E+08 .392E+08 </pre>
Comp 4PM		 <pre data-bbox="1328 663 1430 869"> ANSYS 12.1 JUN 6 2012 00:09:02 ELEM NO. 2 NODAL SOLUTION STEP=1 SUB =1 FREQ=5 REAL ONLY SCY (AVG) CMX =.008441 SMN =-44416 SMX =.339E+08 44416 383E+07 7.95E+07 -1.13E+08 -1.51E+08 -1.88E+08 -2.22E+08 -2.63E+08 -3.01E+08 .339E+08 </pre>
Comp 14PM		 <pre data-bbox="1328 1008 1430 1213"> ANSYS 12.1 JUN 6 2012 00:05:17 ELEM NO. 2 NODAL SOLUTION STEP=1 SUB =1 FREQ=5 REAL ONLY SCY (AVG) CMX =.012939 SMN =-42406 SMX =.339E+08 42406 3.90E+07 7.95E+07 -1.13E+08 -1.51E+08 -1.88E+08 -2.22E+08 -2.63E+08 -3.01E+08 .339E+08 </pre>
Comp 24PM		 <pre data-bbox="1328 1352 1430 1558"> ANSYS 12.1 JUN 6 2012 00:01:07 ELEM NO. 2 NODAL SOLUTION STEP=1 SUB =1 FREQ=5 REAL ONLY SCY (AVG) CMX =.018557 SMN =-47502 SMX =.356E+08 47502 4.00E+07 7.95E+07 -1.13E+08 -1.51E+08 -1.88E+08 -2.22E+08 -2.77E+08 -3.18E+08 .356E+08 </pre>

Figure 30. The geometry (left) and von-Mises stress distribution at mid upstroke (right) of all the compliant spine designs tested.

Each compliant spine design was given a name designation consisting of a number and two letters (e.g. 4PM). The number in the name of the compliant spine referred to the design

number assigned by the optimization algorithm. The two letters in the name referred to the loading condition under which this compliant spine was designed. For example, TL stands for tip load and PM stands for pure moment. During the optimization procedure, the lift force distribution was approximated either as a tip load or a bending moment applied at the tip of the CS. The magnitude of the pure moment applied on the CS was assumed to be the maximum moment that the CS experienced when a tip load, representing the integrated lift load, was applied. Figure 31 shows the tip load and pure moment loading condition as well as the boundary conditions. In reality, the CS experiences a lift load distribution that is a combination of both moment and bending loads.

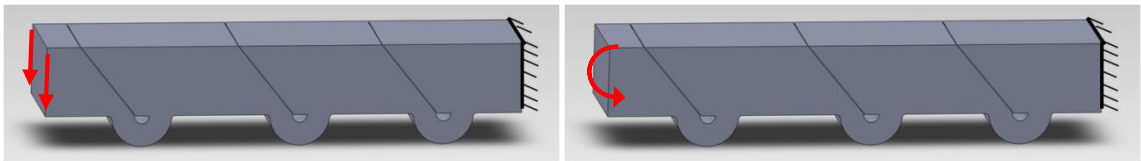


Figure 31. Compliant spines were assumed to have clamped-free boundary condition and were designed using either tip load (TL) loading condition (right) or pure moment (PM) loading condition (left).

Comp 4TL is the compliant spine that was tested during the preliminary constrained flight testing described in Section 4.1. While Comp 4PM, Comp 14PM and Comp 24PM are the dynamically optimized compliant spines that were tested during the flight tests described in Chapter 5.

2.4. Chapter Summary

Two test platform designs were used during the experiments described here. The first was the commercially available Park Hawk and the second one was the new custom built and improved ML101 design. Both platforms had the same overall specifications in order to maintain consistency in the experimental data.

In order to maintain the performance gains of wing morphing without incurring additional complexity, weight penalties or power expenditure, a passive wing morphing approach was chosen. It was concluded based on previous work that more sophisticated wing kinematics are required in order to improve the overall performance of the test ornithopter wings. The desired kinematics can be found in natural avian flyers. A bio-inspired gait known as the Continuous Vortex Gait (CVG) was chosen to be implemented on the wing because it is suitable for the test ornithopter wing morphology and flight speed. The CVG can also be achieved passively because it only required motion in one major joint, namely the wrist.

The structural mechanism mimicking the function of the avian wrist in the ornithopter is the compliant spine. This chapter discussed the load and deflection design specifications for the compliant spine and briefly described its design optimization procedure. This chapter also introduced the compliant spine designs that were tested during the constrained and free flight tests described in Chapter 4 and 5 along with their loading and boundary conditions.

Chapter 3: Leading Edge Spar Analytical Model and Stability Analysis

Inserting a variable stiffness compliant spine into the leading edge spar of the test ornithopter results in a parametrically excited system. A parametrically excited system is defined as a system in which one or more of the constitutive parameters of the problems are varying with time [51]. The oscillations of parametrically excited systems are different from both free and forced oscillations of systems where all the parameters are time invariant [52]. Parametric excitations take the form of time varying coefficients in a system's equations of motion (EOM). Unlike time invariant systems, the stability of a time varying system is not known and areas of instability can arise even in an unforced, undamped linear time varying systems. Therefore, a stability analysis was essential for the compliant leading edge spar, in order to ensure the structural stability of the spar during testing. A compliant leading edge spar is defined as the test ornithopter leading edge spar with a compliant spine design inserted at 37% of the wind half span.

The remainder of this chapter is divided into three sections. Section 3.1 formulates the compliant leading edge spar model, Section 3.2 validates the model using experimental data, and Section 3.3 presents the stability analysis of the leading edge spar.

3.1. Leading Edge Spar Equations of Motion

The compliant leading edge spar was modeled as two rigid rods with a torsional spring in between. Figure 32 shows the model of the compliant spar and along with the assumed boundary conditions. One rod is located inboard of the compliant spine and the other is outboard of the compliant spine. The inboard rod had a pinned boundary condition at the

wing root and was connected to the torsional spring on the other end. The outboard rod had a free boundary condition at the wing tip and was connected to the torsional spring on the other end. The torsional spring in this model represents the compliant spine. Due to the periodicity of the flapping motion of the test ornithopter, the stiffness of the torsional stiffness of the spring representing the compliant spine was described as:

$$k_T = (k_a + k_b) - k_b \cos\left(\frac{2\pi t}{T}\right) \quad (1)$$

where,

$$k_a = k_u \quad (2)$$

$$k_b = \frac{k_d - k_u}{2} \quad (3)$$

In the equations above, k_u and k_d are the upstroke and downstroke stiffness of the compliant spine, t is time, and T is the period of one wing beat cycle. The values of k_u and k_d were determined based on the compliant spine design choice.

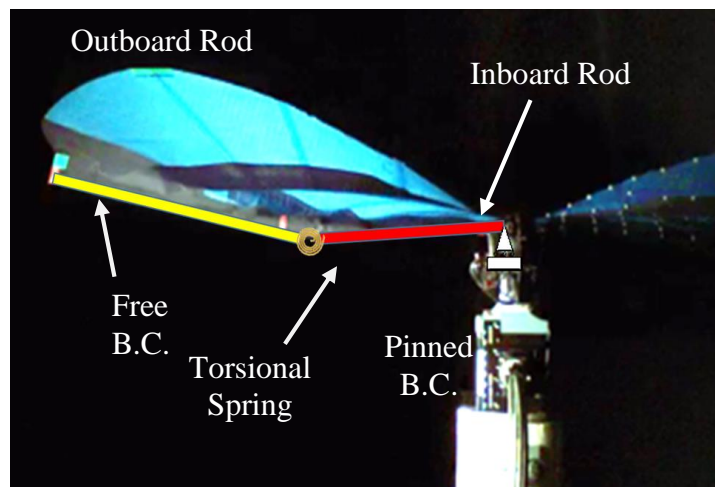


Figure 32. The research platform mounted on a test stand with the compliant leading edge spar model superimposed on the right wing for clarification.

Figure 33 shows a schematic of the compliant leading edge spar system. In the figure, θ_1 is the wing root angle, θ_2 is the spine root angle, L_1 and m_1 are the length and mass of the inboard rod, L_2 and m_2 are the length and mass of the outboard rod, and M is motor torque. During the modeling of the leading edge spar, θ_1 was assumed to be prescribed and it was expressed as:

$$\theta_1 = \frac{\varphi}{2} \sin(\omega t) \quad (4)$$

where, φ is the wing stroke angle, and ω is the flapping frequency in radians per second.

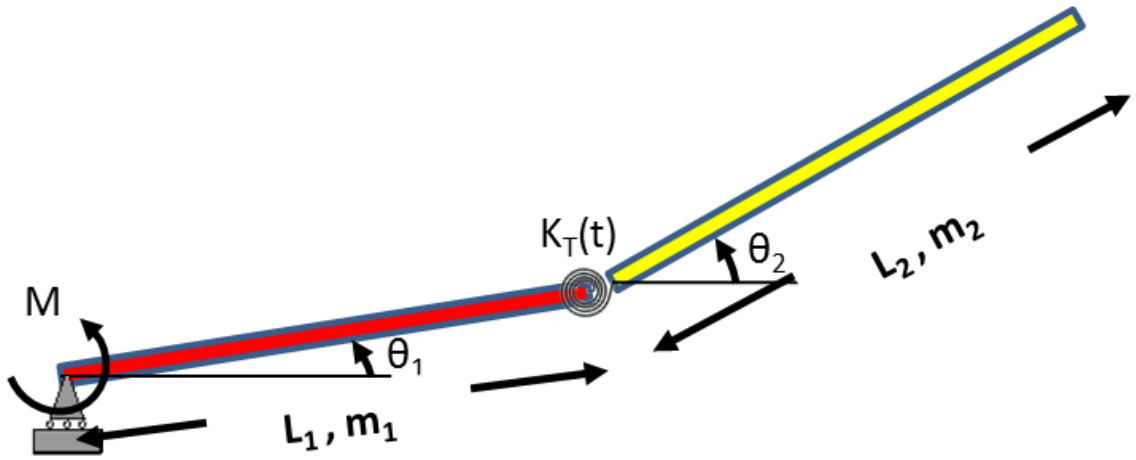


Figure 33. Detailed model of the leading edge spar with a torsional spring representing the compliant spine showing all relevant angles, lengths, and masses.

Using Newton's principles, the equations of motion (EOM) of the two rods shown in Figure 33 were derived. Equations (5) and (6) list the EOM of the system.

$$I_A \ddot{\theta}_1 - k_T [\theta_2 - \theta_1] + m_2 \ddot{y}_{2\ c.m.} L_1 \cos \theta_1 - m_2 \ddot{x}_{2\ c.m.} L_1 \sin \theta_1 = M \quad (5)$$

$$I_B \ddot{\theta}_2 + k_T [\theta_2 - \theta_1] = 0 \quad (6)$$

where, I_A and I_B are the mass moment of inertia of the inboard and outboard rods, respectively and $\ddot{x}_{2\ c.m.}$ and $\ddot{y}_{2\ c.m.}$ are the horizontal and vertical accelerations of the center of mass of the outboard rod, respectively.

Since Equations (5) and (6) are decoupled because the wing root angle was prescribed. Therefore, Equation (6) was solved directly for the spine root angle (θ_2). In the above model, Equation (5) was considered to be a compatibility equation describing the amount of torque the motor had to produce in order to drive the system at the prescribed wing root angle (θ_1). Matlab's[®] general forward time integration function, ODE45, was used to solve Equation (6) numerically. Section 3.2 compares the analytically calculated wing root and spine root angles with their experimentally measured counterparts.

3.2. Leading Edge Spar Model Validation

Experimental data was used to validate the aforementioned model of the leading edge spar. Details about the experiment can be found in Section 4.2.1. The experiment took place at NASA Langley Research Center (LaRC) thermal vacuum laboratory inside a 5 foot x 5 foot thermal vacuum chamber. The deflections of the leading edge spar had to be captured in order to measure the experimental wing root and spine root angle. Four retro-reflective markers were placed at the leading edge in order to capture its deflection. One marker was placed at the wing root, a second one was placed at the location of the compliant spine root, a third marker was placed at the location of the compliant spine tip, and a fourth marker was placed at the wing tip. The kinematics were captured using a Phantom V9.1 high speed camera at 200 frames per second. The camera was mounted outside of the vacuum chamber

as shown in Figure 34(a). In order to illuminate the markers for tracking purposes, 3 LED light panels are mounted on the inside of the vacuum chamber as shown in Figure 34(b).

The experiment was conducted using the same assumptions and constraints used to develop the model. Thus, the experimental data used was taken in vacuum at a pressure of 1 Torr because the model did not include aerodynamic effects.

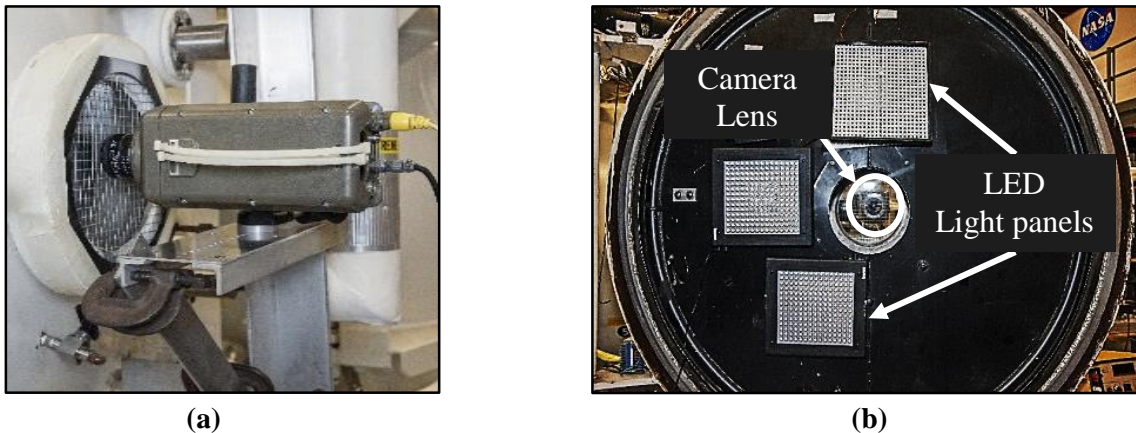


Figure 34. a) A Phantom high speed camera mounted outside the vacuum chamber. b) 3 LED panels mounted on the inside of the chamber to light the chamber and cause the markers to reflect light

The compliant leading edge spar configurations used to validate the model consisted of the leading edge carbon fiber spar with compliant spine design Comp 4TL inserted at 37% of the wing half span. Figure 35 shows an example of a wing spar-spine configuration. Comp 4TL has an upstroke stiffness (k_u) of 3.75 N-m/rad and a downstroke stiffness (k_d) of 72.5 N-m/rad. Figure 30 shows a schematic of compliant spine design, Comp 4TL. During the experiment, the leading edge of the ornithopter was flapped at 4.2 Hz. Vales in Table 1 indicate that this flapping frequency is suitable steady level flight.

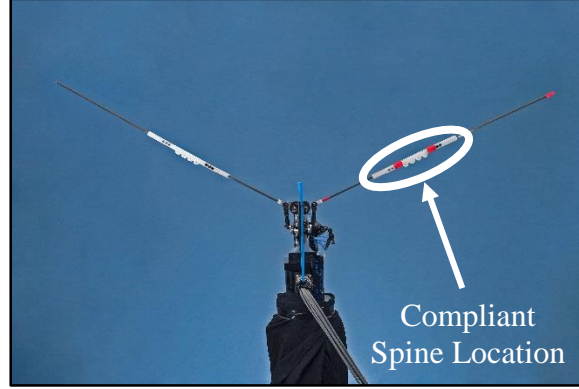


Figure 35. Example of a leading edge spar-spine configuration that was used to validate the leading edge spar analytical model.

The vertical displacement of the retro reflective markers was used to calculate the wing root (θ_{1exp}) and spine root (θ_{2exp}) angles, as shown by Equations (7) and (8).

$$\theta_{1exp} = \sin^{-1} \frac{[Y_{SR} - Y_{WR}]}{L_1} \quad (7)$$

$$\theta_{2exp} = \sin^{-1} \frac{[Y_{ST} - Y_{SR}]}{L_{spine}} \quad (8)$$

where, Y_{WR} , Y_{SR} , and Y_{ST} are the vertical displacements of the wing root, spine root, and spine tip retro reflective markers respectively. L_{spine} is the compliant spine length, which were 6.35 cm (2.5"). Figure 36 and Figure 37 compares the experimental data with the model results. The error between the experimental data and the model was calculated using Equations (9) and (10).

$$RMSE_{\theta_1} = \sqrt{\frac{\sum_1^n (\theta_{1exp} - \theta_1)^2}{n}} \approx 7 \% \quad (9)$$

$$RMSE_{\theta_2} = \sqrt{\frac{\sum_1^n (\theta_{2exp} - \theta_2)^2}{n}} \approx 11 \% \quad (10)$$

where, n is the number of data points used over one flapping cycle.

The analytical wing root angle agreed within 7 % of the experimental data while the analytical spine root angle agreed within 11 % of the experimental data. The error observed in Figure 36 and Equation (9) was due to the assumption that the analytical wing root angle is sinusoidal. Experiments show that the wing root angle is not exactly sinusoidal. The wings spent more than half of the stroke below the horizontal plane. The error observed in Figure 37 and Equation (10) was attributed to the fact that any physical system has some structural damping, which was not accounted for in the model. Moreover, the model assumed that the carbon fiber spar was rigid while the physical carbon fiber spar had some flexibility. Finally the high frequency content noticed in the analytical spine root angle is typical of a bounded response of Mathieu's equation in which the ratio between the system's Eigen frequencies and frequency of excitation (flapping frequency) is small [53].

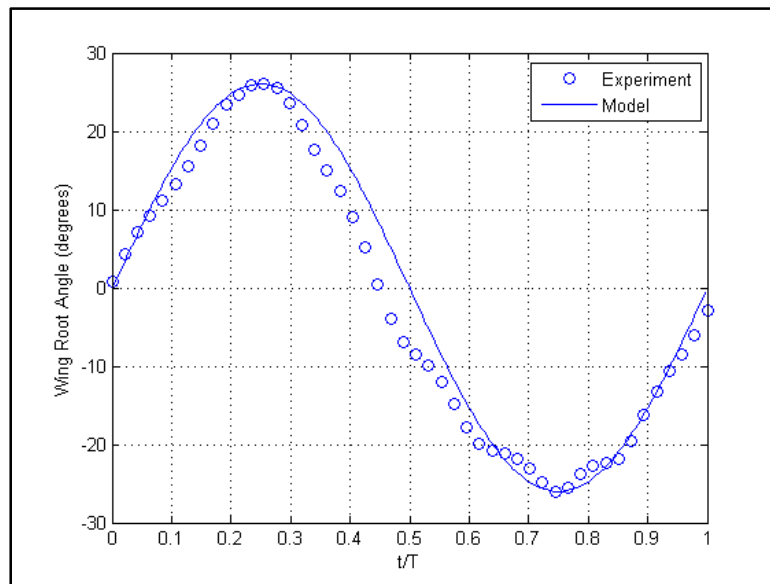


Figure 36. Experimental and analytical wing root angle versus time normalized by the period of one wing beat cycle. The experiment agrees with the model within 7%.

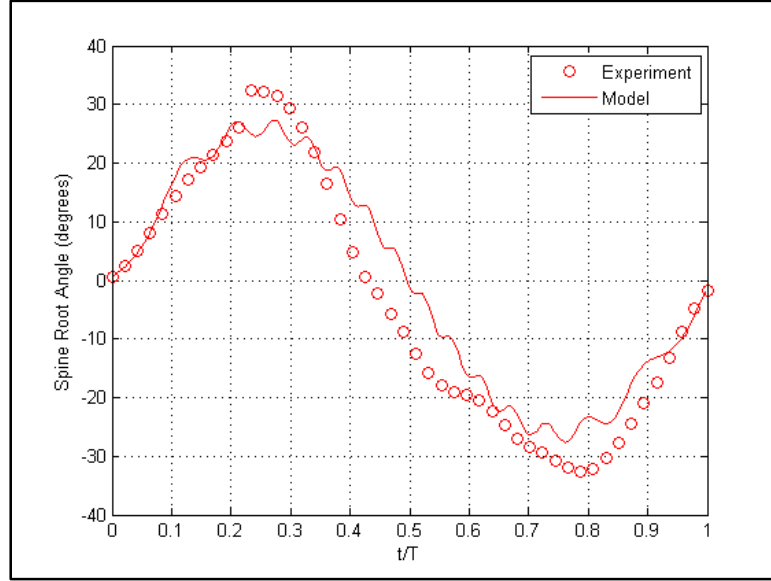


Figure 37. Experimental and analytical spine root angle versus time normalized by the period of one wing beat cycle. The experiment agrees with the model within 11%.

3.3. Leading Edge Spar Stability Analysis

The structural stability of the leading edge spar-spine system can be determined using the experimentally validated analytical model. Equation (6) was written in the form of a non-homogeneous Mathieu's equation, as shown by Equation (11). Equation (12) through (17) define the symbols in Equation (11).

$$\ddot{\theta}_2(p) + [\delta + 2\epsilon \cos(2p)] \theta_2(p) = [\alpha + 2\beta \cos(2p)] \sin(2p) \quad (11)$$

$$\delta = \frac{k_a + k_b}{A} \quad (12)$$

$$\epsilon = \frac{-k_b}{2A} \quad (13)$$

$$\alpha = \frac{\varphi(k_a + k_b)}{2A} \quad (14)$$

$$\beta = \frac{-\varphi k_b}{4A} \quad (15)$$

$$p = \frac{\pi t}{T} \quad (16)$$

$$A = \frac{I_B \pi^2}{T^2} \quad (17)$$

Several books and articles discuss the significance, history, and stability of Mathieu's equation [51, 54]. Mathieu's equation is very useful in modeling several physical and mathematical systems. The solution of Mathieu's equation takes different forms and various levels of stability according to the values of the system parameters, δ and ϵ . Therefore it is necessary to determine the values of the δ and ϵ for which the compliant leading edge spar may become unstable or have an unbounded response. The most common way to determine the stability of Mathieu's equation is using a Strutt Diagram [55]. A Strutt diagram is a plot of δ versus ϵ . The lines shown in the diagram form boundaries between values of the parameters for which the solution is stable or unstable. The stability diagram was developed using the Hill's determinant method. Hill's determinant method was introduced in [56] and has been outlined in several publications since then [51, 55].

The stability of the compliant leading edge spar can be determined using the Strutt diagram of the homogenous equation of the compliant spar (See Equation (18)). The non-homogeneous term on the right hand side of Equation (11) does not affect stability.

$$\ddot{\theta}_2(p) + [\delta + 2\epsilon \cos(2p)] \theta_2(p) = 0 \quad (18)$$

Figure 38 shows the Strutt diagram of Equation (18). The Strutt diagram is in terms of δ and ϵ . Since the design parameters for the compliant spine were the upstroke and downstroke stiffness, it was useful to transform and plot the classical Strutt diagram in terms of k_u and k_d . Figure 39 shows the transformed Strutt diagram. The figure also shows that design Comp 4TL, which is marked in the plot with a black dot, falls within a stable region of the Strutt diagram. The figure demonstrates that the leading edge spar with design Comp 4TL inserted in it is structurally stable when flapped in vacuum.

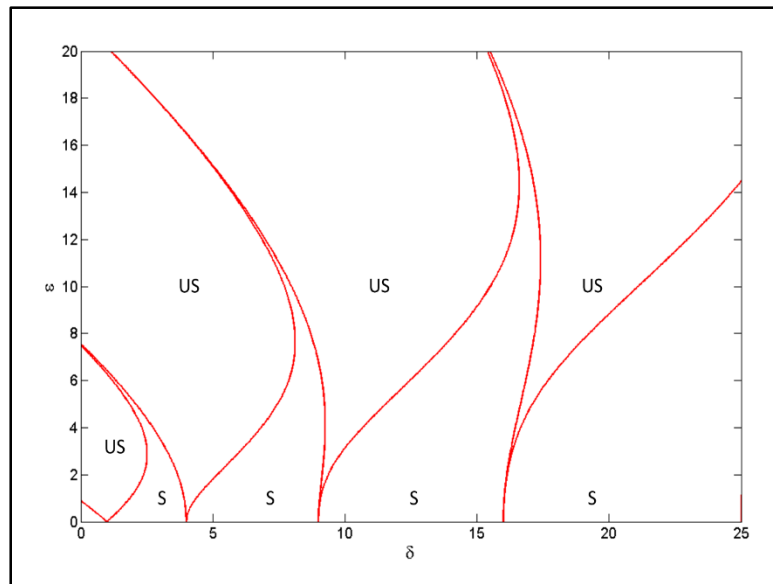


Figure 38. Strutt diagram for Mathieu's equation. The lines form boundaries or transition point between stable and unstable solution regions. Regions marked with US are unstable and regions marked with S are stable.

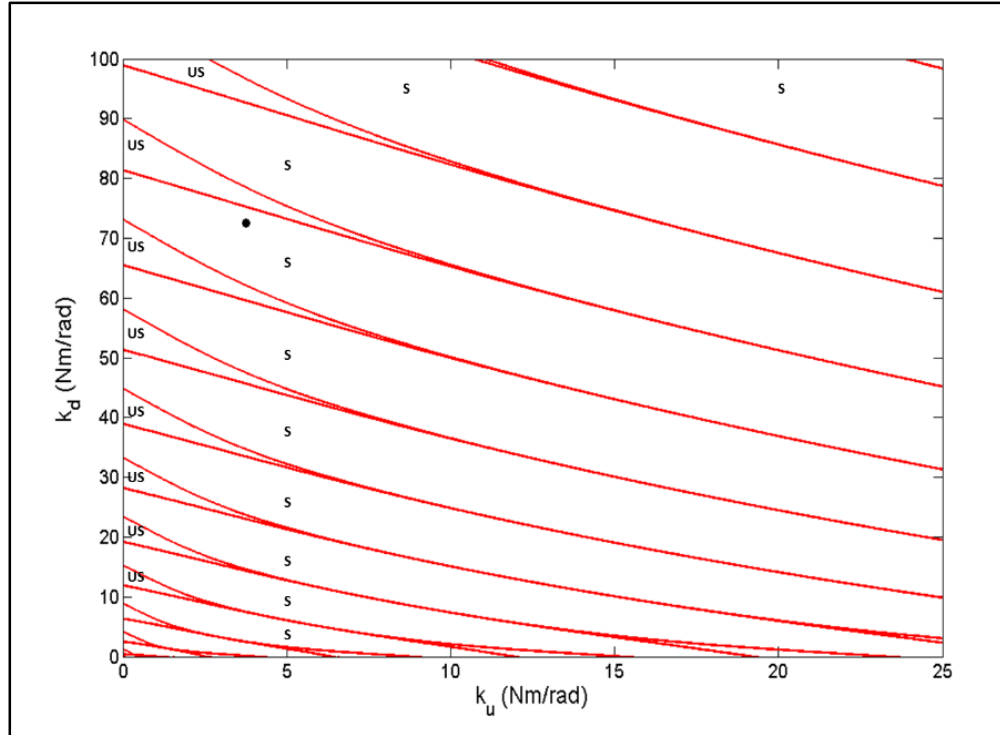


Figure 39. Strutt diagram for Mathieu's equation in terms of the upstroke and downstroke stiffness. The black dot represents compliant spine Comp 4TL. Regions marked with US are unstable and regions marked with S are stable.

Stability of Equation (11) could also be shown analytically by solving for the system response and examining the phase plane plot. The phase plane is a plot of the system response (θ_2) versus its first derivative ($\dot{\theta}_2$). Figure 40 shows the phase plane plot of Equation (11). The red dot in Figure 40 signifies the initial conditions given to the system. The plot shows that the response of leading edge spar with design Comp 4TL inserted at 37% of the wing half span is bounded and stable.

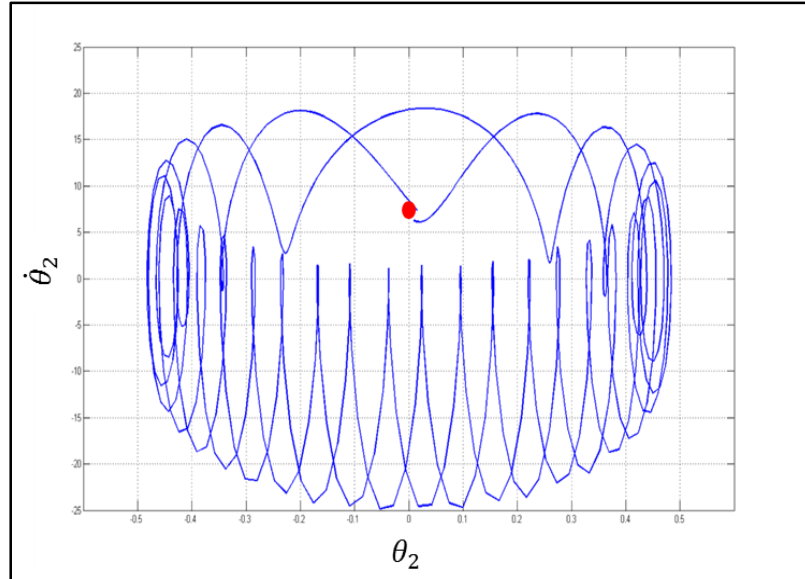


Figure 40. Phase plane plot of the spine root angle. The plot shows that the response of the leading edge spar with design Comp 4TL inserted at 37% of the wing half span is bounded and stable.

3.4. Effect of Damping on Leading Edge Spar Stability

The model discussed in Section 3.1 did not include any type of damping. Any physical system includes some degree of damping known as structural damping. Moreover, aerodynamic effects on a flexible structure appear as damping terms in a system's equations of motion. Therefore, the inclusion of damping in the leading edge spar-spine model is important. In this section, the effect of adding damping on the structural stability of the leading edge spar-spine is investigated.

A damper was added to the leading edge spar-spine system as shown in Figure 41. In the figure, C_T is the constant damping coefficient in Newton meter second per radian. A linear damping model was assumed and the EOM of the outboard rod is expressed as shown in Equation (19). Equations (20) and (21) define the terms in Equation (19) that were not defined by Equations (12) through (17). In Equation (19), ζ is the damping ratio.

$$\begin{aligned} \ddot{\theta}_2(p) + 2\zeta\dot{\theta}_2(p) + [\delta + 2\epsilon \cos(2p)] \theta_2(p) \\ = 2\gamma \cos(2p) + [\alpha + 2\beta \cos(2p)] \sin(2p) \end{aligned} \quad (19)$$

$$\zeta = \frac{C_T T}{2\pi I_B} \quad (20)$$

$$\gamma = \frac{C_T T \varphi}{2\pi I_B} \quad (21)$$

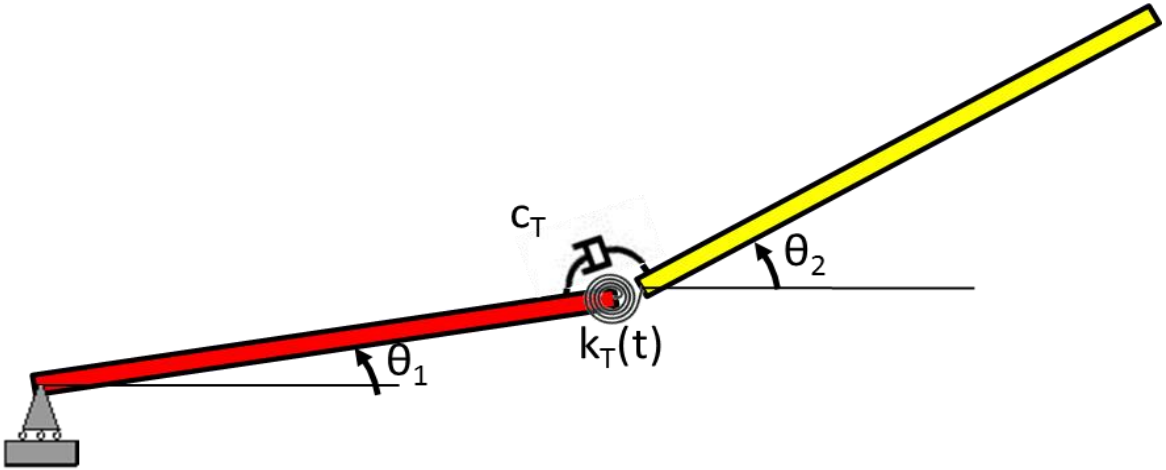


Figure 41. Model of the leading edge spar-spine system with a linear damping element

The structural stability of the leading edge spar with the torsional spring and damper was determined using the homogeneous equation (See Equation (22)). The non-homogeneous terms on the right hand side of Equation (19) do not affect stability.

$$\ddot{\theta}_2(p) + 2\zeta\dot{\theta}_2(p) + [\delta + 2\epsilon \cos(2p)] \theta_2(p) = 0 \quad (22)$$

Equation (22) is known as the lossy Mathieu's Equation and has been addressed frequently in the literature [51, 57]. The stability of Equation can also be determined using a Strutt Diagram as shown by Figure 42. The Strutt diagram is in terms of δ and ϵ . The lines formed by the red markers are for the case of $\zeta = 0$. They are the same curves shown in Figure 38 plotted in a different orientation in order to clarify the effect of damping. The

lines formed by the blue and green markers are for the cases of $\zeta = 0.2$ and 0.5 , respectively. The results in Figure 42 confirms that adding damping has a stabilizing effect for $\zeta > 0$. The presence of damping shrinks the instability area. This figure was obtained by solving Equation (22) numerically and using Floquet's theory to determine the criteria of stability [55].

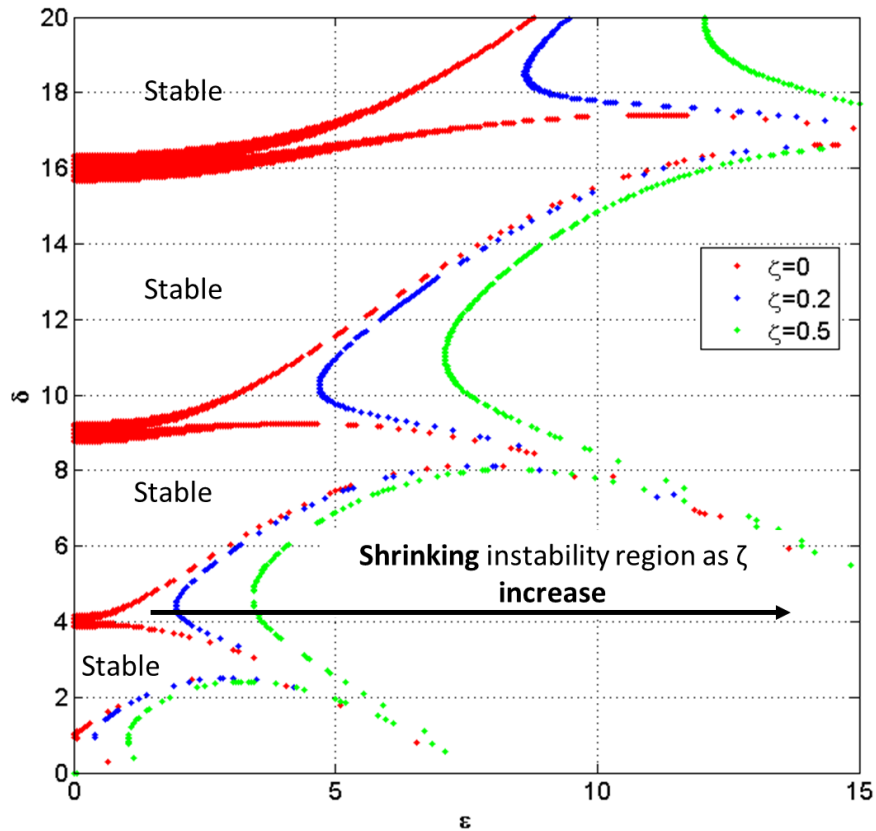


Figure 42. Strutt Diagram of the Lossy Mathieu's Equation for the cases of $\zeta= 0$ (red), 0.2 (blue), and 0.5 (green).

The design parameters for the compliant spine were the upstroke and downstroke stiffness, thus it was useful to transform and plot the classical Strutt diagram in terms of k_u and k_d to investigate the effect of damping on the design range for the up and downstroke stiffnesses. Figure 43 shows the transformed Strutt diagram. The results from the figure

confirms that damping shrinks the instability regions thus including viscous damping element into the leading edge spar-spine model is structurally stabilizing. More importantly, the figure shows that there exist a damping ratio between 0.2 and 0.5 for which areas of instability only occurs for $k_u < 0$. Given that the upstroke stiffness of the compliant spine is always greater than zero, it can be concluded that there exists a value for ζ for which the leading edge spar is always stable regardless of the upstroke and downstroke stiffness choices.

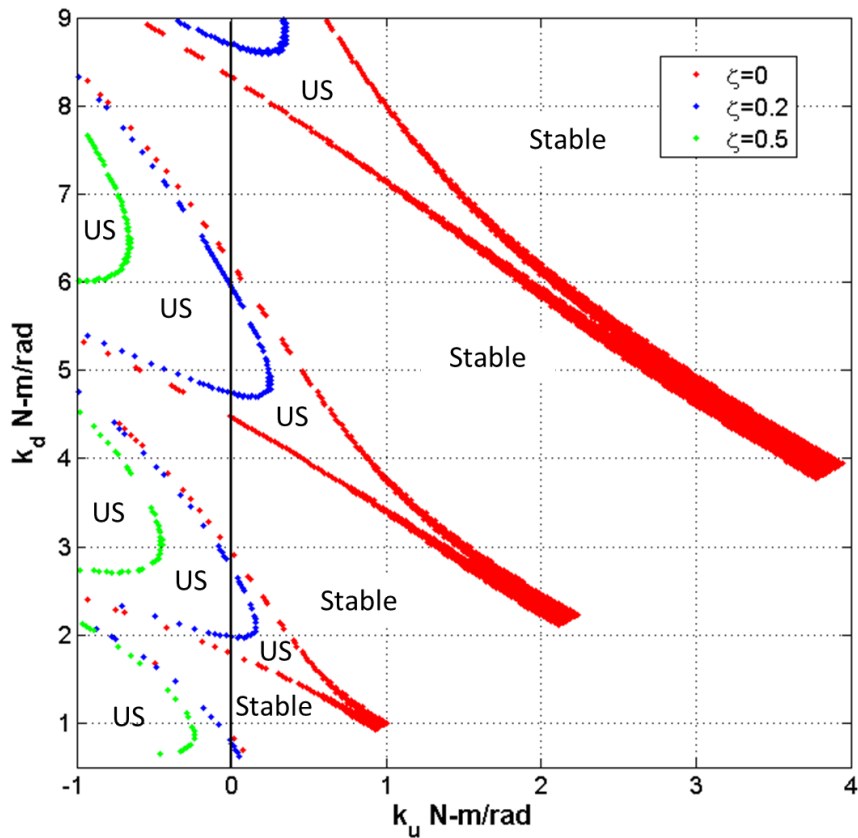


Figure 43. Strutt diagram for the lossy Mathieu's equation in terms of the upstroke and downstroke stiffness for the cases of $\zeta=0$ (red), 0.2 (blue), and 0.5 (green). Unstable regions shrink with increasing ζ and are marked by US.

3.5. Chapter Summary

In this chapter, the leading edge spar with a variable stiffness compliant spine inserted in it was modeled as a linear time periodic system. Such systems have a different stability criterion than that of a linear time invariant system. A stability analysis was necessary to ensure that the leading edge spar will remain structurally stable during testing. The EOM's of the compliant leading edge spar were derived. The EOMs were solved numerically and the system's response was validated using experimental data. The experimental validation indicated that the modeled wing root and spine root angles agreed with the measured angles within 7% and 11%, respectively. The validated EOM, were then reformulated in terms of Mathieu's equation and the stability of the compliant leading edge spar was determined both graphically and analytically. Stability was determined graphically using a Strutt diagram that showed that the response of leading edge spar with a compliant spine design inserted at 37% of the wing half span was stable and bounded. Finally, the effect of damping on the structural stability of the leading edge spar was investigated. It was concluded that there exists a damping ratio for which the leading edge spar spine system is stable for all values of compliant spine upstroke and downstroke stiffnesses.

Chapter 4: Constrained Flight Test Experiment

This chapter introduces a series of constrained flight tests designed to evaluate the performance of an ornithopter wing with compliant spines incorporated in its wings. A constrained flight test was defined as a test in which the fuselage of the ornithopter is constrained to a 6 DOF load cell and was neither free to translate nor rotate. The constrained flight tests in this chapter can be divided into two main parts. The first used a preliminary compliant spine design prototype to validate the efficacy and feasibility of passive wing morphing. This preliminary compliant spine design prototype was designed under a quasi-static loads and using a high stress safety factor to ensure that it did not fail. The second constrained flight test used compliant spines designed under dynamic loads, similar to the ones experienced during flight. The second test objective was to determine the effect of the presence of the compliant spine on the vehicle's wings performance, both in vacuum and at ambient pressure to separate the inertial and the aerodynamic effects

4.1. Preliminary Constrained Flight Test

4.1.1. Experimental Procedures of Constrained Flight Test

Based on preliminary quasi-static analyses and optimization, a compliant spine design was selected for prototyping and testing. The compliant spine design tested was design Comp4TL. It consisted of three compliant hinges, with each compliant hinge consisting of two concentric semicircles. The radius of the inner semi-circle was 1 mm and the radius of the outer semi-circle was 4 mm. Each hinge had a uniform thickness of 3 mm. Figure 30 shows the geometry of the compliant spine and its predicted von-Mises stress distribution at mid upstroke. Figure 31 shows the tip load loading condition as well as the boundary conditions used during the design optimization.

Comp 4TL was made of Delrin and was attached to the spar using 10-32 nylon bolts as shown in Figure 44. The test ornithopter used for this constrained flight test was a commercially available Park Hawk Model. The specifications for the test platform are listed in Table 1. The wing performance of the test ornithopter was measured with and without the compliant spine inserted into the leading edge spars. Three performance metrics were selected as a basis of comparison for the test ornithopter: (1) the required electric power, (2) the lift and thrust produced during one flapping cycle, and (3) the wing tip and spine tip deflections during the up and down strokes. In this section, the experimental set-up of these three performance metrics are described.

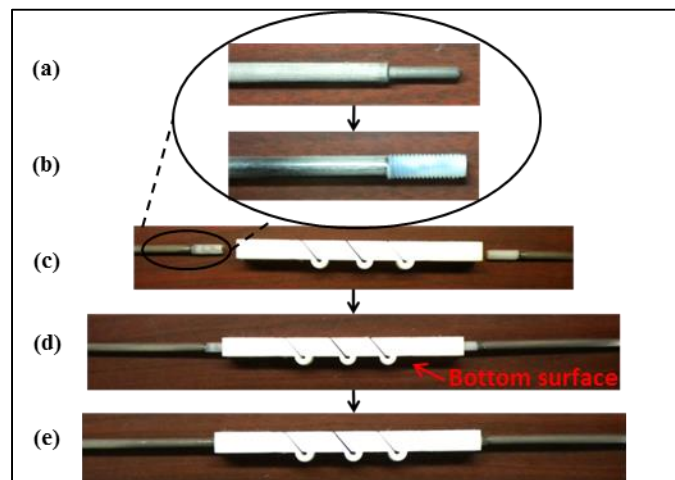


Figure 44. The compliant spine was attached to the spar (a) using 10-32 Nylon bolts. The bolts were glued to both ends of the spar as shown in (b) and (c). Then the spars were screwed into the ends of the spine as shown in (d) and (e).

The first wing performance metric used in this study was the electric power required by the flapping mechanism. In order to calculate the electric power, both the current and the voltage drawn from the power supply during flapping were measured. A constant voltage power supply was used for all of the experiments; hence, the supply voltage was fixed at 12.27 V. In order to measure the current, a CQ-121E current sensor manufactured

by Asahi Kasei Cooperation was used. The sensor was mounted in series with the power supply and the electric speed controller. Figure 45 shows a schematic of the current sensor circuit. Once the current and the voltage were measured, the electric power consumed by the ornithopter at various flapping frequencies was calculated.

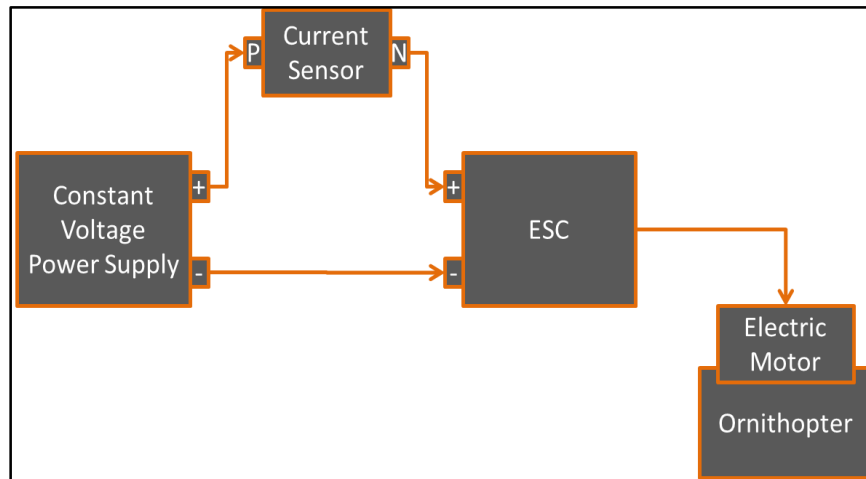


Figure 45. Schematic of current sensor circuit.

The second set of wing performance metrics used were the lift and thrust produced by the ornithopter. A six degree of freedom strain gauge transducer, manufactured by Advanced Mechanical Technology Inc., was used to measure the lift and thrust produced by the test ornithopter. The lift and thrust were measured at various flapping frequencies with and without the compliant spine inserted in the ornithopter leading edge wing spars. Figure 46(a) and Figure 46(b) show the test ornithopter mounted on the load cell.

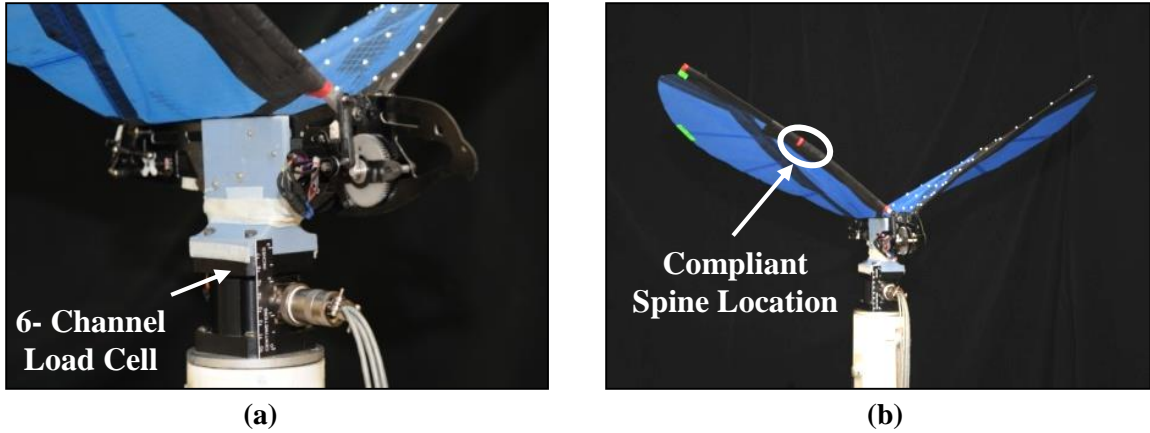


Figure 46. (a) Test ornithopter mounted on a six channel load cell. (b) The compliant spine was inserted at the leading edge spar of the test ornithopter at 37% of the wing half span

The third set of wing performance metrics applied were the wing tip and spine tip bending deflections. To capture the bending deflections of the wing during the up and down strokes, three red markers were placed on the leading edge spar. One marker was placed at the wing root, another was placed at the location of the compliant spine tip and a third marker was placed at the wing tip, as shown in Figure 47. The wing leading edge spar kinematics were captured using a Phantom 9 high speed camera at 100 frames per second. The camera time stamp was used to determine the frames that included the mid downstroke and upstroke kinematics.

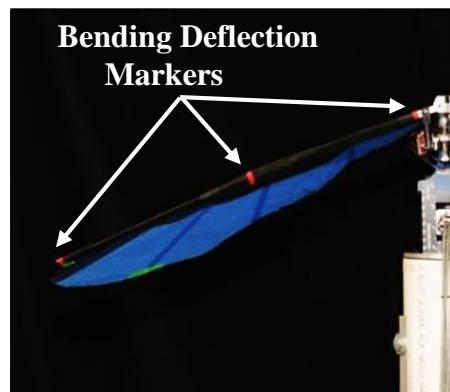
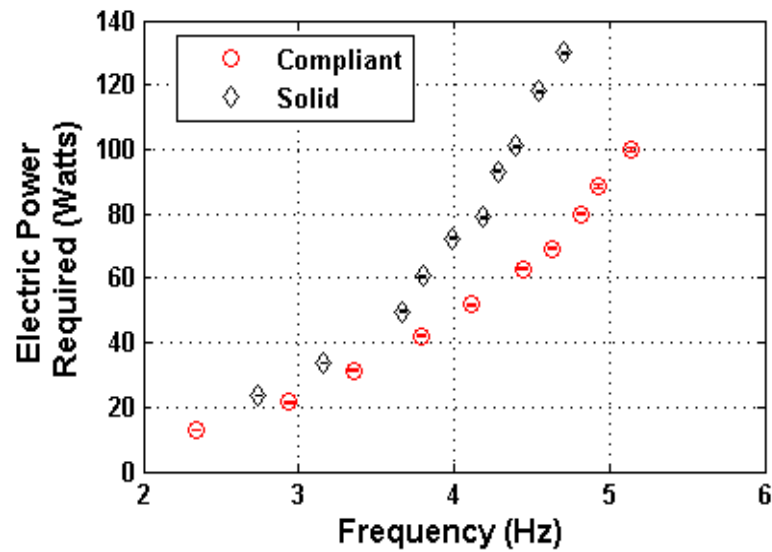


Figure 47. Red markers at the wing leading edge used for capturing wing bending deflections at the wing root, the compliant spine tip and the wing tip.

4.1.2. Experimental Results of Constrained Flight Test

Data was collected at various flapping frequencies, where the flapping frequency was controlled by the throttle position on a remote control radio transmitter. Figure 48 (a) and Figure 48(b) show the electric power consumed by the ornithopter at various flapping frequencies, and the flapping frequency versus the percentage throttle, respectively. The “solid” data corresponds to the performance of the ornithopter wing with the continuous leading edge spar without the compliant spine insert, and the “compliant” data corresponds to the performance of the ornithopter wing with the compliant spine inserted in the wings leading edge spar.



(a)

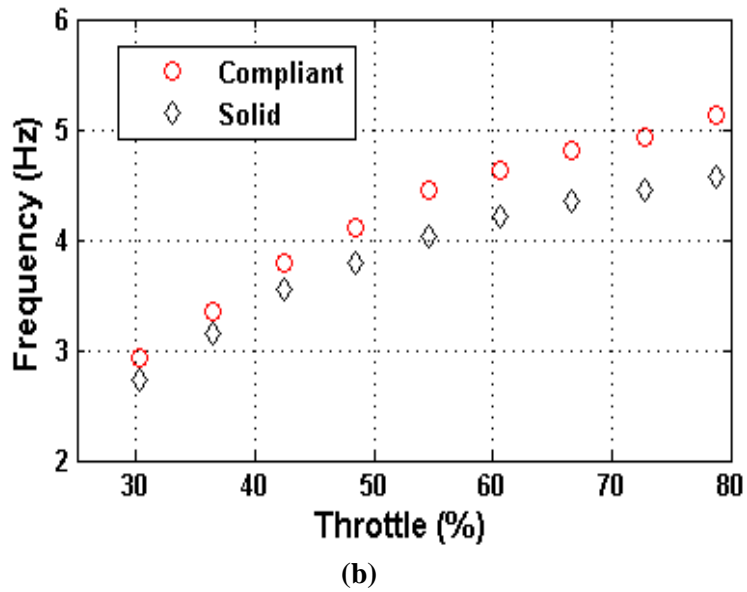


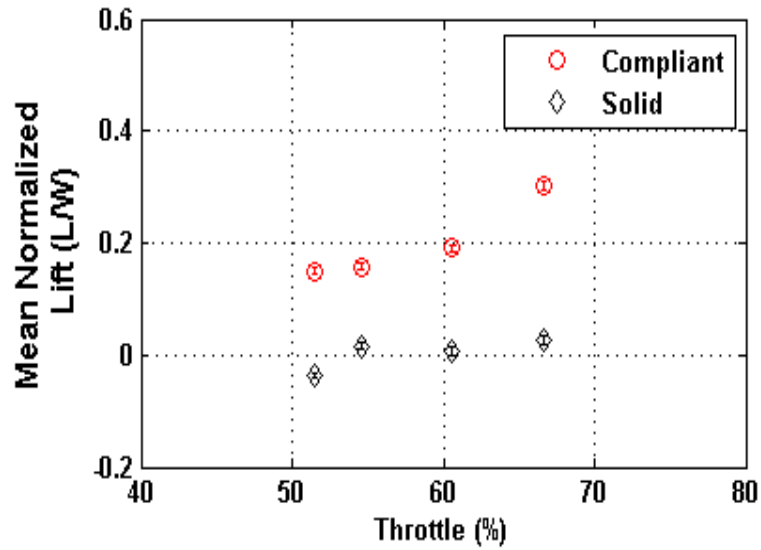
Figure 48. (a) Electric power required vs. flapping frequency (b) Flapping frequency versus percent throttle for the continuous and compliant ornithopter.

From Figure 48(a), it is observed that the test ornithopter with the compliant spine insert consumed less power than it did without the compliant spine, for all flapping frequencies. The focus of this work was centered on steady level flight. The steady level flight flapping frequency of the test ornithopter was determined using minimum power and drag curves to be approximately 4.7 Hz in [6]. At 4.7 Hz, the power savings due to the presence of the compliant spine is 44.7%. In addition, Figure 48(b) shows that the ornithopter with the compliant spine inserted in its wings flapped at a higher flapping frequency for all throttle inputs. The fact that the ornithopter flapped at a higher frequency for a given throttle input was also attributed to this power expenditure reduction.

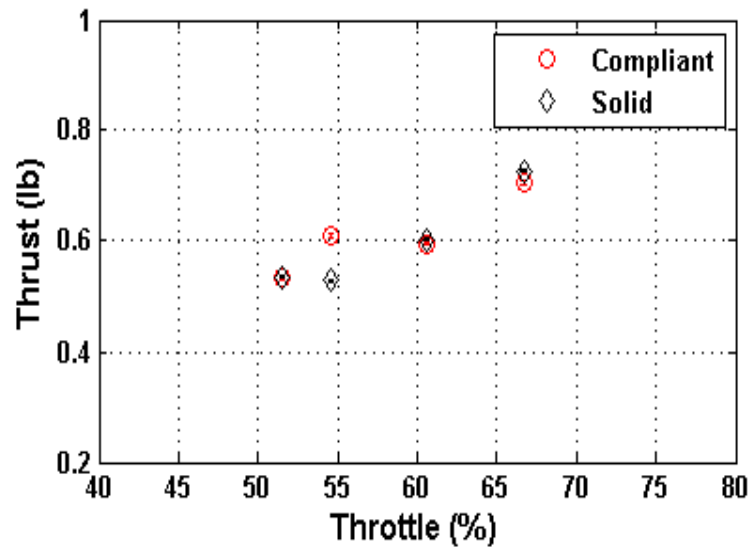
Second, the lift and thrust were measured at various flapping frequencies for one wing beat cycle. The mean lift and thrust over one flapping cycle was calculated and the mean lift was normalized by the test ornithopter’s weight. Research previously done in [6], determined that the mean induced lift produced by the test ornithopter when it was clamped

to a load cell at zero forward speed and zero angle of attack was zero. This was due to the symmetry between the up and down strokes. This symmetry caused the ornithopter to produce an equal amount of positive and negative lift during the down and up strokes, making the mean lift zero. The results shown in Figure 49(a) for the continuous leading edge spar confirm these results. The figure also shows that by inserting the compliant spine into the spars, an asymmetry was introduced between the up and down strokes, which causes an increase in the mean lift. Moreover, at the steady level flight flapping frequency of 4.7 Hz, which corresponds to a throttle setting of 60%, the ornithopter with the compliant spine produced an additional mean lift supporting 16% of its body weight. This lift gain could not be produced under the same conditions with a continuous leading edge wing spar. This increase in mean lift can be directly translated into improved payload capability.

Although lift gains due to extreme wing bending deflections during the upstroke have been reported in passive wing morphing experiments [28], they were accompanied by severe thrust penalties. A goal of the current work was to maintain the lift gains while mitigating the thrust penalties. Thus, the effect of the presence of the compliant spine on the mean thrust produced by the test ornithopter was evaluated. Figure 49(b) shows that for any given throttle input, the mean thrust produced by the ornithopter, with and without the compliant spine, are similar. It is concluded that the compliant spine was successful at producing lift gains without incurring any significant thrust penalties.



(a)



(b)

Figure 49. (a) Mean lift produced over one flapping cycle, normalized by the weight versus percentage throttle (b) Mean thrust produced over one flapping cycle versus throttle position plot

Lastly the wing kinematics of the continuous and hinged compliant spars were captured using high speed photography were compared. The compliant spine was designed to bend during the upstroke while remaining stiff (i.e., mimicking a continuous spar) during the downstroke. Figure 50 compares the leading edge spar bending deflections at mid

downstroke and mid upstroke for both the hinged compliant and continuous wing configurations. From Figure 50(b), it can be seen that during the downstroke there is minimal deflection due to the contact surfaces in the compliant joints, while Figure 50(d) shows that during the upstroke, the compliant spine bends as desired.

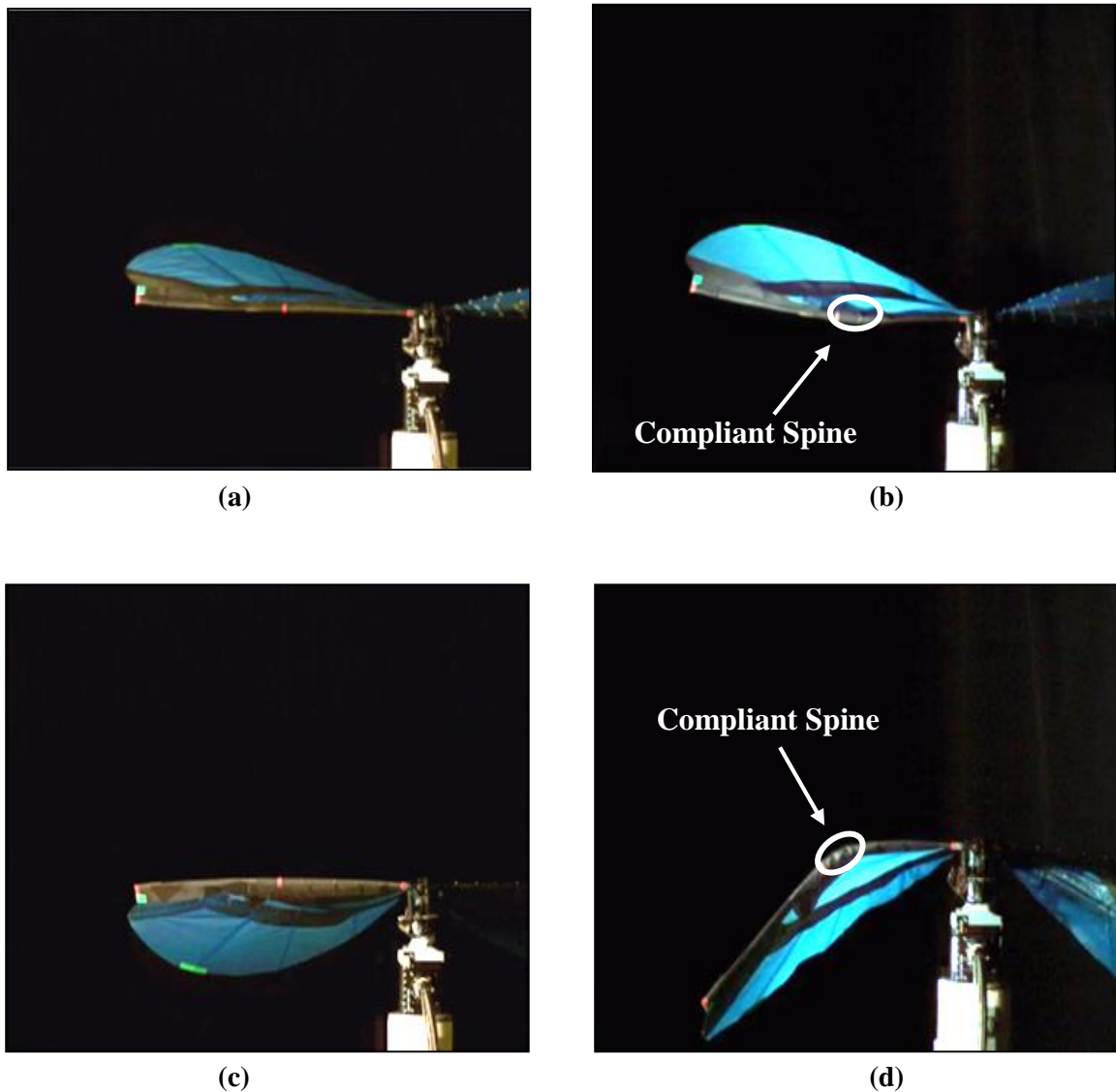


Figure 50. (a) Wing bending deflections at mid downstroke for the ornithopter with the continuous spar, i.e., without the compliant spine. (b) Wing bending deflections at mid downstroke for the ornithopter with the compliant spine. (c) Wing bending deflections at mid upstroke for the ornithopter with the continuous spar. (d) Wing bending deflections at mid upstroke for the ornithopter with the compliant spine.

Figure 50(a) and Figure 50(b) show comparable deformation during the downstroke indicating that the compliant spine is acting like the continuous spar. Figure 50(c) and Figure 50(d) shows that the wing with the compliant spine deflects more than that without the compliant spine during the upstroke. Table 3 shows the bending deflections at the location of the compliant spine tip relative to the wing root for the wing with and without the compliant spine at a flapping frequency of 4.7 Hz. These deflections were calculated by determining the difference between the vertical location of the middle bending deflection marker and the root bending deflection marker, mentioned in Section 4.1.

Table 3. Bending deflections at the compliant spine tip relative to the wing root*.

Wing Position	Bending deflection of wing with continuous spar (cm)	Bending deflection of wing with hinged compliant spar (cm)	Difference in deflections (cm)
Mid Downstroke	-3.41	-2.57	-0.84
Mid Upstroke	4.07	0.72	3.36

* Negative bending is upwards bending, positive bending is downwards bending.

The data in Table 3 along with Figure 50 show that during the downstroke the bending deflection of the leading edge spar with and without the compliant spine are similar. During the upstroke, the bending deflection of the leading edge spar with the compliant spine is larger than the wing without the compliant spine. The bending deflections noticed during the upstroke due the presence of the compliant spine leads to a reduction of the wing relative surface area and therefore a decrease in the amount of negative lift produced during that portion of the wing beat cycle.

4.2. Constrained Flight Test in Vacuum

This section describes the second set of constrained flight tests. The objective of this test was to determine whether the wing performance benefits, mentioned in Section 4.1, observed due to the presence of the compliant spine are a result of the aerodynamics effects, the inertial effects, or both. In other words, this experiment was designed to determine whether the benefits mentioned above were due to changing the wings moment of inertia or due to changing the wings local angle of attack along the span. In order to meet this objective, it was necessary to isolate the inertial and aerodynamics effects, thus this constrained flight test was performed both in vacuum and at ambient pressure. The remainder of this section describes the vacuum test experimental procedures and results.

4.2.1. Vacuum Test Experimental Procedures

4.2.1.1. Facility and Equipment

The test was conducted at the NASA Langley Research Center (LaRC) Thermal Vacuum Laboratory. The vacuum chamber where the vehicle was tested had a diameter of 5 feet and was 5 feet deep. The chamber is capable of providing a pressure range from atmospheric pressure of 760 mm to altitude vacuum and thermal simulation of approximately $10 \text{ E-}7$ Torr. Figure 51(a) and Figure 51(b) show the 5' x 5' thermal vacuum chamber and the test ornithopter mounted inside the vacuum chamber, respectively.

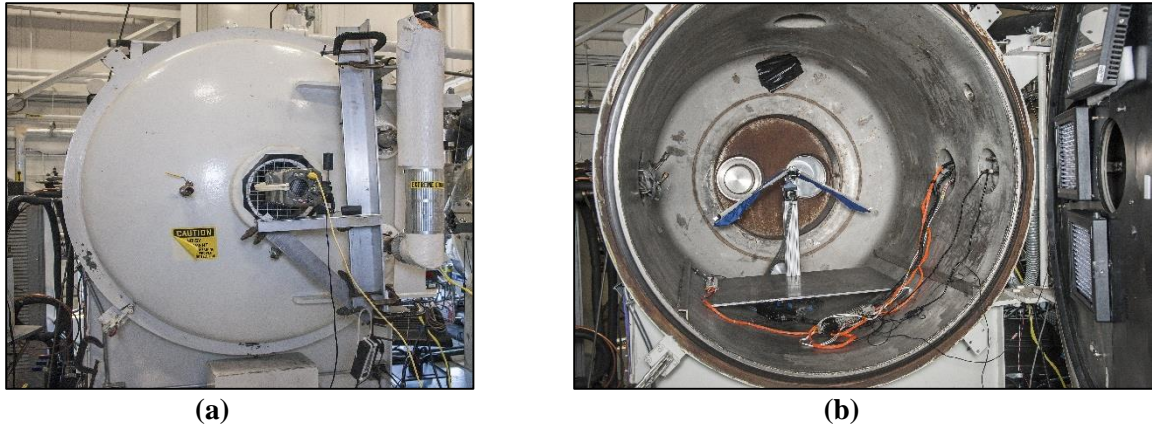


Figure 51. (a) NASA LaRC 5 foot x 5 foot thermal vacuum chamber. (b) Test ornithopter mounted inside the vacuum chamber.

During this test, lift, thrust, and pitching moment produced by a test ornithopter over one flapping cycle were used as comparison metrics to determine the effect of the presence of the compliant spine on the vehicle's aerodynamics and inertia [58]. In order to assess the aerodynamic and inertial effects separately, the comparison metrics were recorded in vacuum and at ambient pressure. During the ambient pressure runs, the pressure inside the chamber was set to 760 Torr (1 atm). During the vacuum runs, the pressure inside the chamber was 1 Torr (0.001 atm).

A six degree of freedom load cell was used to measure the lift, thrust, and pitching moment produced by the test ornithopter at various flapping frequencies. The flapping frequency was controlled using the throttle on a radio transmitter. Table 4 shows the throttle settings that were tested for each of the wing spar configurations in air and in vacuum. A given throttle percentage can correspond to various flapping frequencies depending on the ornithopter configuration being tested. In Section 4.2.2, results are presented with respect to the flapping frequency and not the throttle percentage. Figure 52(a) shows the

ornithopter mounted on the load cell inside the chamber. The load cell was mounted in the vacuum chamber using an aluminum pylon as shown in Figure 52(b).

Table 4. Throttle settings tested for all wing spar configurations in air and vacuum.

Test Run	1	2	3	4
Ambient (760 Torr)	18%	24%	30%	36%
Vacuum (1 Torr)	12%	15%	18%	24%

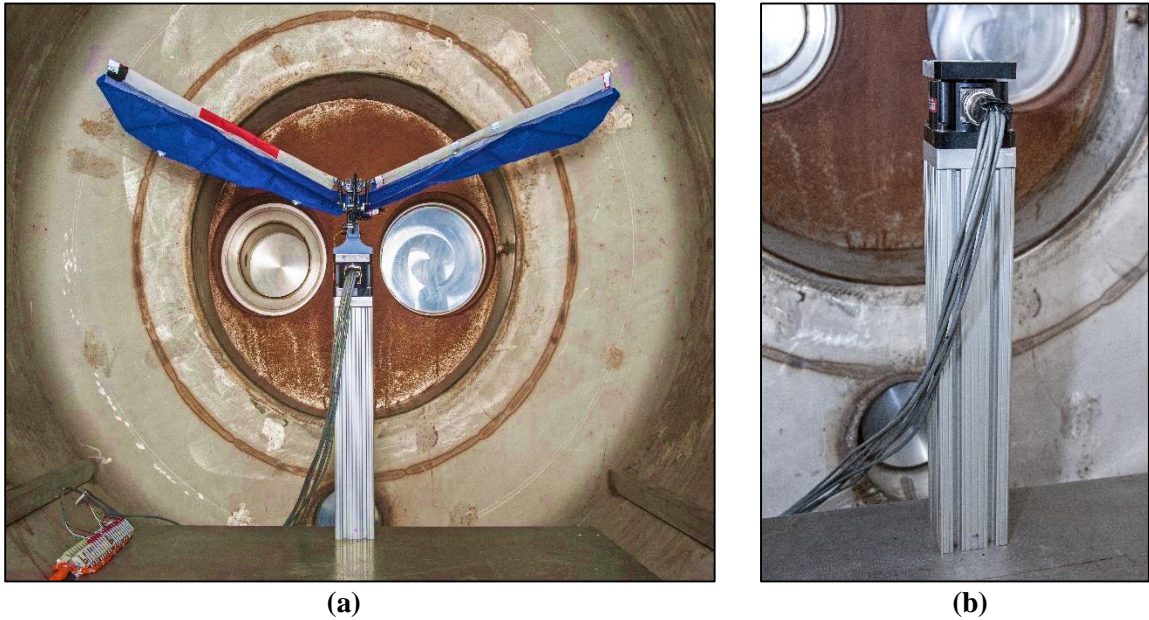


Figure 52. (a) Test ornithopter mounted on a six channel load cell in a 5 ft x 5 ft thermal vacuum chamber. (b) Load cell mounted on an aluminum pylon inside the vacuum chamber.

4.2.1.2. Tested Wing Spar Configurations

The research platform used during this test was the Morpheus Lab custom-built test ornithopter (ML 101). Figure 11 shows a picture of the vehicle and Table 1 includes the test platform specifications. Different wing spar configurations were tested. The first configuration was the continuous spar, which was the test ornithopter with a uniform carbon fiber leading edge spar. The rest of the configurations were the hinged compliant spars, which were the test ornithopter with a compliant spine inserted in its leading edge

spar. The only difference between the continuous and the hinged compliant wing spar configurations was the presence of the compliant spine in the leading edge spar of both wings. Three compliant spine designs were tested, thus there were a total of four wing spar configurations (1 continuous and 3 compliant). The continuous spar wing configuration served as the baseline configuration.

All of the compliant spines were 63.5 mm long with 25.4 mm tabs on both sides to allow for attachment to the leading edge spar. The compliant spine was attached to the carbon fiber spar of the leading edge using six 5-40 bolts and a Delrin collar, as shown in Figure 53. The characteristic differences between the various compliant spine designs were the number of compliant hinges and the compliant joint geometry. The compliant spine designs evaluated during this constrained flight test were: Comp 24PM, Comp 4PM, and Comp 4TL. Figure 30 shows the geometry of the compliant spine and its predicted von-Mises stress distribution at mid upstroke and Figure 31 shows the loading condition as well as the boundary conditions used during the design optimization.

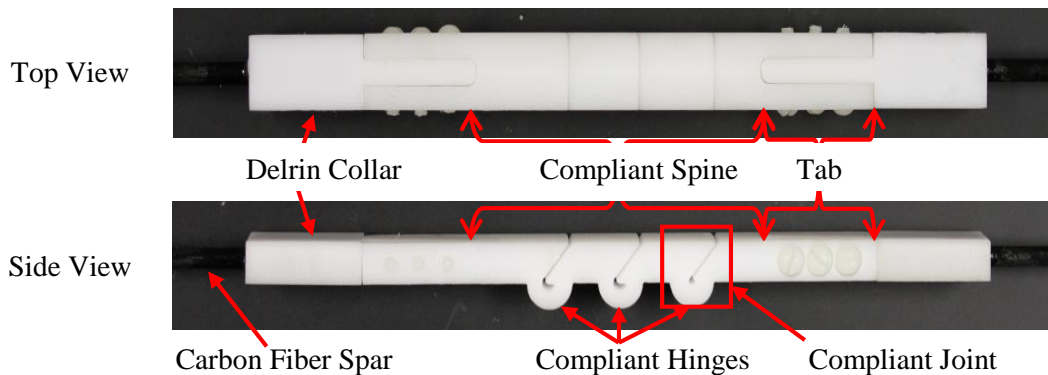


Figure 53. Compliant spine assembly components

Table 5 lists the compliant spine designs, their loading condition, and the number of compliant hinges. Comp 4PM and Comp24PM were designed using a loading condition and a dynamic load similar to the ones experienced by the wing during flight and thus were

included in this test so that each design's presence effect on the inertia and aerodynamics was further understood. Design Comp 4TL was included in this test because it was previously used for the constrained flight test described in Section 4.1. Comp 4TL was also the first compliant spine design to show the benefits of passive morphing on the overall lift production [59, 60].

Table 5. Specifications of compliant spine designs for vacuum constrained flight test.

Design Name	Loading Condition	Number of compliant joints
Comp 4TL	Tip load	3
Comp 4PM	Pure moment	2
Comp 24PM	Pure moment	4

4.2.2. Vacuum Constrained Flight Test Results

This section discusses the experimental results of the constrained flight test performed in vacuum. The effect of wing compliance on the lift, thrust, and pitching moment produced by the ornithopter over one flapping cycle in air and in vacuum is discussed in this section.

Figure 54 shows a plot of the mean thrust produced by the ornithopter over one flapping cycle versus the flapping frequency. The 95% confidence interval was calculated and the error bounds were found insignificant (less than 2%) thus they are not shown in the plot. The figure shows that at ambient pressure for any given flapping frequency, the ornithopter with the compliant spine inserted in its wings produced more thrust than the ornithopter with the continuous wing spar configuration. Thrust gains imply improved range and endurance. Figure 54 shows that in vacuum these thrust benefits disappear. In other words, in the absence of air, both the hinged compliant and the continuous wing spar configurations behave similarly. From the figure, it was concluded that the thrust gains

observed due to the presence of the compliant spine in the leading edge wing spar are attributed to the aerodynamic effects and not the inertial effects.

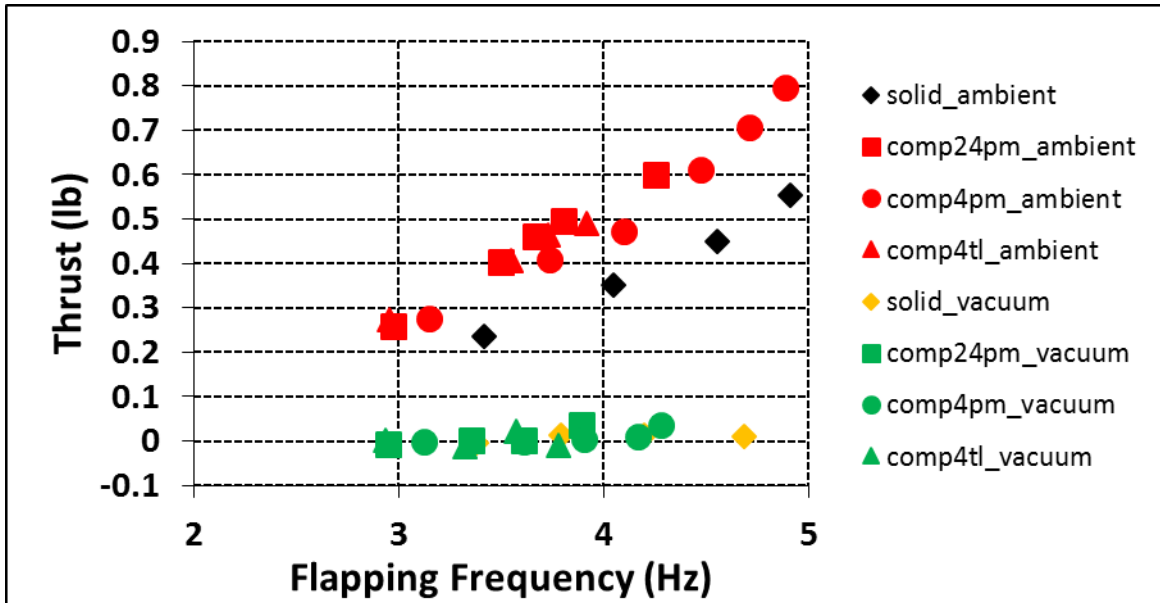


Figure 54. Mean thrust versus flapping frequency for the Continuous, Comp 4PM, Comp 4TL, and Comp 24PM wing spar configurations in ambient pressure (red and black data markers) and at vacuum (green and yellow data markers)

The second force that was measured during this test was the lift force. Figure 55 shows a plot of the mean lift produced by the ornithopter over one flapping cycle normalized by the vehicle’s weight versus the flapping frequency. The 95% confidence interval was calculated and the error bounds are shown in the plot. The figure shows that at ambient pressure, the ornithopter with the compliant spine inserted in its wings produces more lift per unit weight than the ornithopter with the continuous wing spar configuration, especially at flapping frequencies above 4 Hz. The lift gains here imply a higher payload capability. Figure 55 also shows that in vacuum these lift benefits disappear. Hence, in the absence of air, both the hinged compliant and the continuous wing spar configurations behaved similarly. In the presence of air, lift gains are observed due to the wing compliance, while

in vacuum, all four test configurations produce similar amount of lift. From Figure 55, it can be concluded that the lift gains observed due to the presence of the compliant spine in the leading edge spar are attributed to the aerodynamic effects and not the inertial effects.

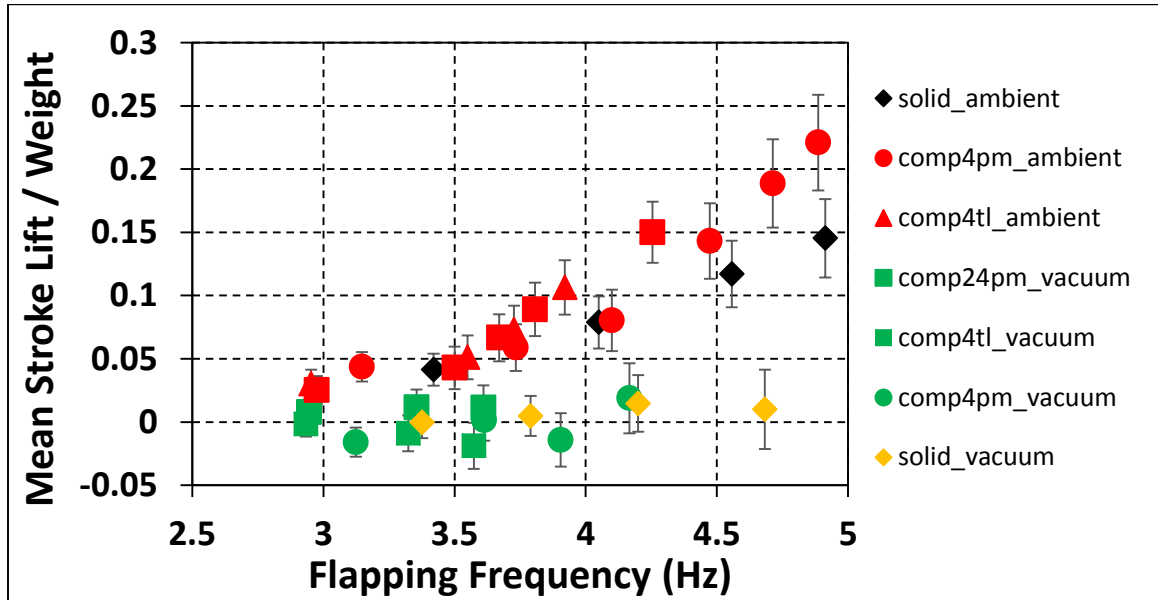


Figure 55. Mean lift normalized by the vehicle’s weight for the Continuous, Comp 4PM, Comp 4TL, and Comp 24PM wing spar configurations in ambient pressure (black and red data markers) and at vacuum (yellow and green data markers).

The final metric used to compare the effect of wing compliance in air and in vacuum is the pitching moment. Based on the experimental set-up and load cell manufacturer’s specification, a positive pitching moment corresponds to the front of the ornithopter pitching upwards and vice versa. Figure 56 shows a plot of the mean pitching moment produced by the ornithopter over one flapping cycle versus the flapping frequency. The 95% confidence interval was calculated and the error bounds were found insignificant (less than 1%) thus they are not shown in the plot. The figure shows that at ambient pressure, the ornithopter with the compliant spine inserted in its wings had a negative pitching moment that was larger in magnitude than the ornithopter with the continuous wing spar

configuration. Moreover, Figure 56 shows that in vacuum these variations in pitching moment disappear. In other words, in the absence of air, both the hinged compliant and the continuous wing spar configurations behaved similarly. In the presence of air, pitching moment variations were observed due to the wing compliance, while in vacuum all four test configurations produce similar amount of pitching moment. In vacuum, all four test configurations have a zero pitching moment. While in air, the wing compliance increases the negative mean pitching moment. The larger negative pitching moment indicates that the presence of the compliant spine has the same effect on pitching moment as increasing camber in the wings. From the figure, it can be concluded that the pitching moment variations observed due to the presence of the compliant spine in the leading edge spar are attributed to the aerodynamic effects and not the inertial effects.

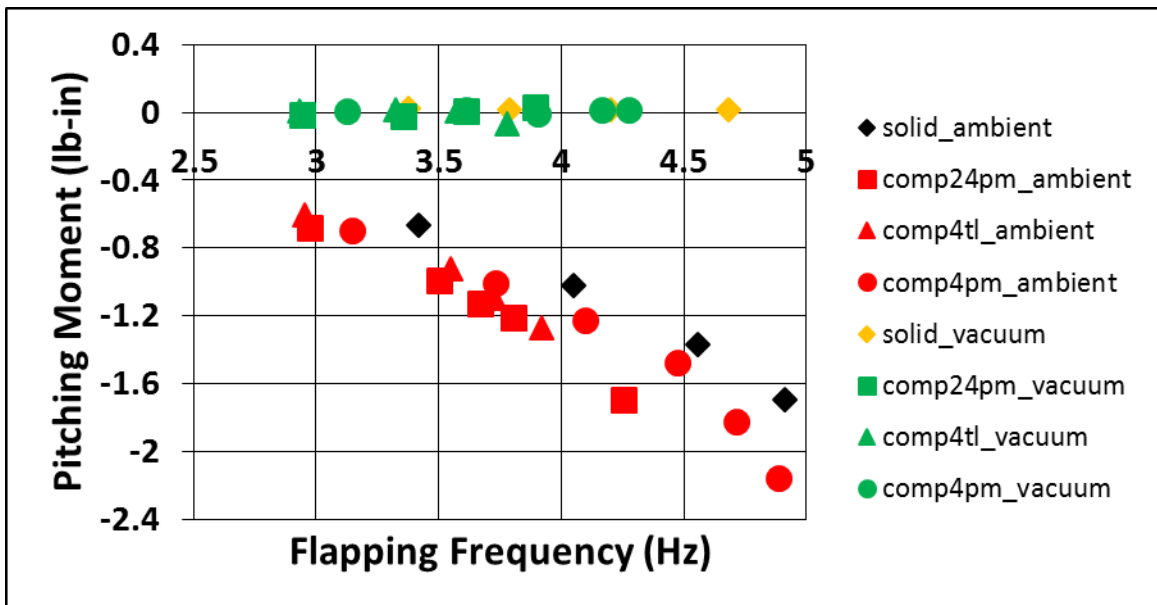


Figure 56. Mean pitching moment versus flapping frequency for the Continuous, Comp 4PM, Comp 4TL, and Comp 24PM wing spar configurations in ambient pressure (black and red data) and in vacuum (yellow and green data).

4.3. Chapter Summary

During the constrained flight test, a quasi-static optimization was conducted and one of the designs resulting from this optimization was tested as a proof of concept. The presence of the compliant spine in the ornithopter wing was found to introduce an asymmetry between the upstroke and the downstroke. This asymmetry was due to the presence of the compliant hinges that allowed for bending during the upstroke and the contact surfaces that did not allow for deflections during the downstroke. For any given flapping frequency, the ornithopter with the compliant spine consumed less electric power than the same ornithopter without the compliant spine. It was also found that for any given throttle input, the ornithopter with the compliant spine flapped at a higher flapping frequency, produced more mean lift and did not incur any thrust penalties when compared to the ornithopter without the compliant spine. Moreover, at the steady level flapping frequency, 4.7 Hz, the ornithopter with the compliant spine achieved 44.7% reduction in the power required and 16% lift gain. The aforementioned power reduction suggest range and endurance benefits, where the lift gains indicate payload capability improvements. The results of this test confirmed the feasibility of passive wing morphing using a compliant mechanism. The test also confirmed that passive morphing resulted in overall wing performance improvements.

After proving the efficacy of passive wing morphing using a compliant mechanism, it was necessary to understand whether these gains are due aerodynamic or inertial effects or both. In order to understand the aforementioned question, the second constrained flight test was performed both in air and in vacuum to determine the source of the aforementioned lift and thrust gains, as well as to investigate the effect of the presence of several compliant

spine designs on the wing performance both in ambient pressure and in vacuum. Results of the vacuum constrained flight test confirmed the efficacy of passive morphing in improving the lift and thrust forces produced by the ornithopter during a flapping cycle. Testing the vehicle in vacuum isolated the aerodynamic effects from the inertial effects. Results show that the lift and thrust gains observed along with the variations on pitching moment are due to aerodynamic effects and not inertial effects. These results indicate that the wing performance gains achieved due to morphing are due to aerodynamic effect. This was a valid conclusion because in vacuum, all test configurations, both continuous and compliant, performed the same. It was only in the presence of air when variations and gains in pitching moment, lift and thrust were observed.

Chapter 5: Free Flight Testing Experiment

Several flight tests were conducted in order to assess the performance of the various compliant spine designs presented earlier in free flight [61]. The flight tests were conducted at the Wright Patterson Air Force Base (WPAFB) in the Air Force Research Lab's (AFRL) Indoor Small Unmanned Aerial Systems (SUAS) laboratory. This facility is the largest Vicon® motion capture system lab in the United States. This chapter describes the experimental procedures and free flight tests results.

5.1. Free Flight Testing Experimental Procedures

This section describes the equipment used, ornithopter preparation, test configurations flown, and the experimental set-up. Figure 57 shows a picture of the flight test chamber in the SUAS lab.

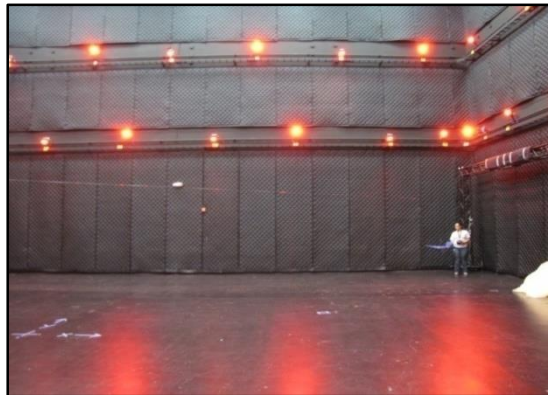


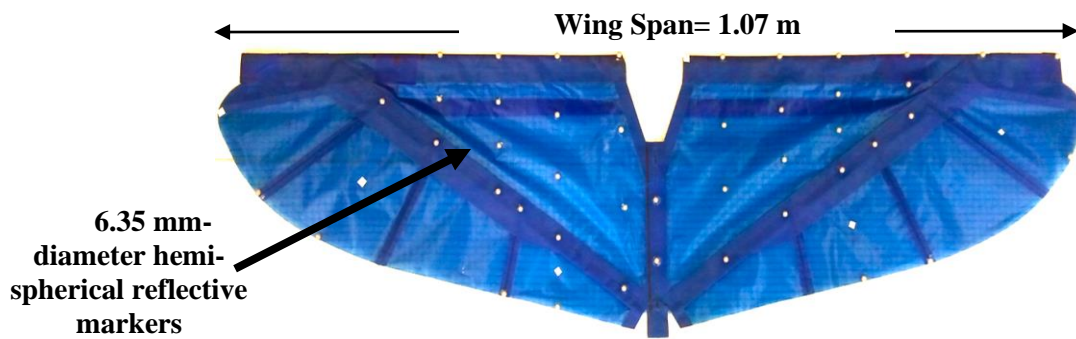
Figure 57. Test Chamber in the AFRL SUAS flight lab.

The AFRL SUAS indoor flight test laboratory is composed of an enclosed flight test chamber and a control room. The test chamber is a large, instrumented room where vehicles can be flown. It is roughly 16.8 m x 21.3 m x 10.6 m. SUAS lab instrumentation consists of a VICON® motion capture system with 60 motion capture cameras. By adding small retro-reflective markers to a vehicle, the VICON® system can track position and

orientation of the vehicle to an accuracy of about 1.0 mm. The control room was used to process and record test data, such as vehicle position/orientation, velocity, acceleration, commands, sensor telemetry, and video-stream and audio data.

5.1.1. Test Platform Experimental Setup

Fifty-three spherical markers were attached to the test vehicle in the locations needed to obtain sufficient data to fully determine the vehicle wing and body kinematics. The marker had a diameter of 6.35 mm and were out of retro-reflective tape, which reflects light. Of the fifty-three markers, forty-four 6.35mm diameter markers were placed in an asymmetrical pattern on the wings in order to aid in down range tracking. The nine additional markers were distributed as follows: 5 were placed on the fuselage to determine the ornithopter's body kinematics, 3 were placed on the tail to record user control inputs and 1 was placed at the wing root to measure the wing angle during a given flapping cycle. Figure 58(a) and Figure 58(b) show the placement of the wing and tail reflective markers, respectively. Markers were distributed over both wings to balance the weight and they were placed asymmetrically to aid with tracking and post-processing. Data was collected at a sampling rate of 200 Hz during these tests. The Vicon® motion capture system was used to capture and contrast the wing 3D kinematics of the ornithopter with and without the compliant spine inserted in the leading edge spar.



(a)



(b)

Figure 58. (a) Wing and (b) Tail reflective markers placement.

In addition to the Vicon® markers mounted on the ornithopter's wings, tail, and body, a current sensor was connected in series between the electric speed controller and the battery in order to measure the current drawn by the motor. The data was recorded using an onboard Logomatic v2 Serial SD data logger. Figure 59(a) and Figure 59(b) show a schematic of the current sensor connection and a picture of the data logger, respectively.

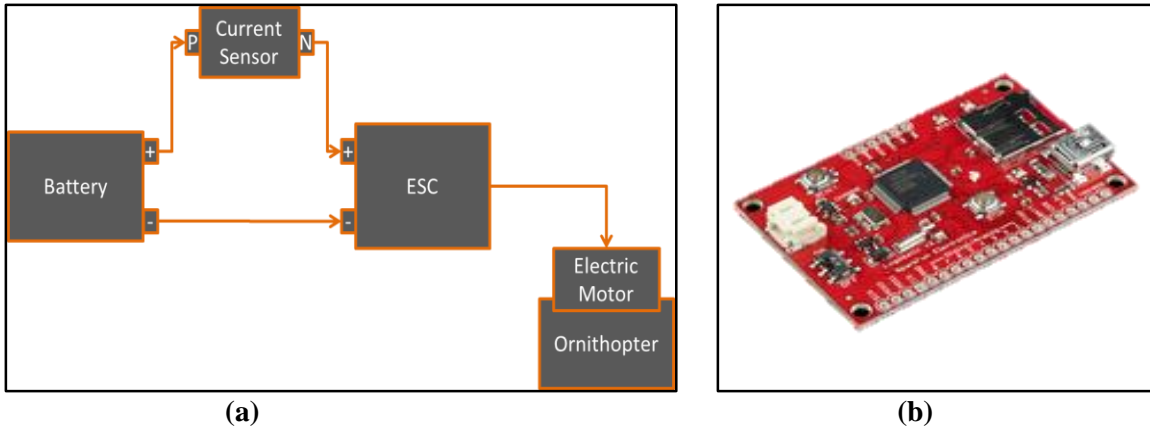


Figure 59. (a) Schematic for current sensor. (b) Logomatic v2 Serial SD data logger used to record the current sensor output.

5.1.2. Flight Testing Technique

To aid in test data repeatability and prevent vehicle impacts with the chamber walls, a low-friction tether was utilized to guide the vehicle within the test chamber. The vehicle was suspended from a lead wire hung from this tether in order to restrain its flight path. The lead line was able to slide along the tether by using a barrel swivel attachment. The tether was strung horizontally between two trusses at opposite corners of the flight lab, at 2.1 m height in order to maximize flight distance and keep the test vehicle at a height where camera coverage is ideal. A wire crimp and a braking tether were used at the end of the flight path in order to arrest the vehicle at the end of each test run. Figure 60 shows a schematic of the test setup.

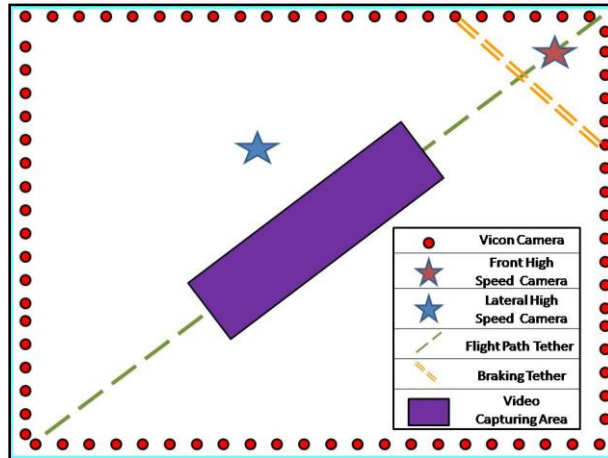


Figure 60. Test setup schematic showing the Vicon® cameras (representative), high speed cameras, flight path, braking tether, and video capturing area.

5.1.3. Free Flight Tested Ornithopter Wing Configurations

Four ornithopter wing configurations were tested. The first configuration tested was an ornithopter with a continuous, carbon fiber wing spar. This configuration is referred to as the solid spar configuration. The remaining configurations consisted of hinged compliant wing spars and are referred to as the compliant configurations. A hinged compliant wing spar configuration was defined as a leading edge spar with a compliant spine inserted in the leading edge spar at 37% of the wing half-span to mimic the function of the avian wrist. Three compliant spine designs were tested, thus there were a total of four configurations (1 continuous and 3 hinged compliant).

The Morpheus Lab ornithopter (ML101) was used as the test platform during this test. Common test platform specifications can be found in Table 1. Figure 11 shows an image of a Morpheus Lab custom-built test ornithopter (ML 101) with a continuous leading edge spar. This test configuration served as the test baseline. The mass of the continuous wing spar configuration ornithopter including batteries, motor, current sensor, markers, and data logger was measured to be 528 g.

The ML101 test ornithopter was also flown for the hinged compliant wing spar configurations. For the compliant wing spar configurations, the spines consisted of the same components included in the vacuum constrained flight test and they were integrated into the leading edge using the same method shown in Figure 53. The compliant spines tested during the free flight tests were Comp 4PM, Comp 14PM, and Comp 24PM designs. Table 6 lists the compliant spine designs, the number of compliant hinges, and the total mass of the ornithopter with these spines inserted in its leading edge and including all the components that were previously present in the continuous configuration. Comp 4TL design was replaced by Comp 14PM in this flight test because Comp 14PM was the equivalent three compliant hinge compliant spine that was designed using flight-like loading condition. Figure 30 shows the geometry of the compliant spines and their predicted von-Mises stress distribution at mid upstroke and Figure 31 shows the loading condition as well as the boundary conditions used during the design optimization.

Table 6. Specifications of compliant spine designs.

Design Name	Number of compliant joints	Ornithopter Mass
Comp 4PM	2	611 g
Comp 14PM	3	614 g
Comp 24PM	4	612 g

5.2. Free Flight Experimental Results

The free flight experiment results can be divided into three main sections. The first explains the free flight characteristics of a test ornithopter’s wing and body kinematics. The second discusses the effect of the presence of the compliant spine on the leading edge spar deflections. Lastly, the third part of this section introduces several flight metrics to

compare the overall wing performance with and without the compliant spine inserted in its wings.

5.2.1. Ornithopter's Free Flight Kinematics

One of the goals of these flight tests was to extend the current database of steady level free flight data for avian-scale ornithopters. In order to attain this goal, consistent and repeatable kinematics over several flapping cycles were required. Before presenting the collected flight test data, the inertial reference frame, C_I , and body fixed frames, C_0 , used during this test were defined as shown in Figure 61.

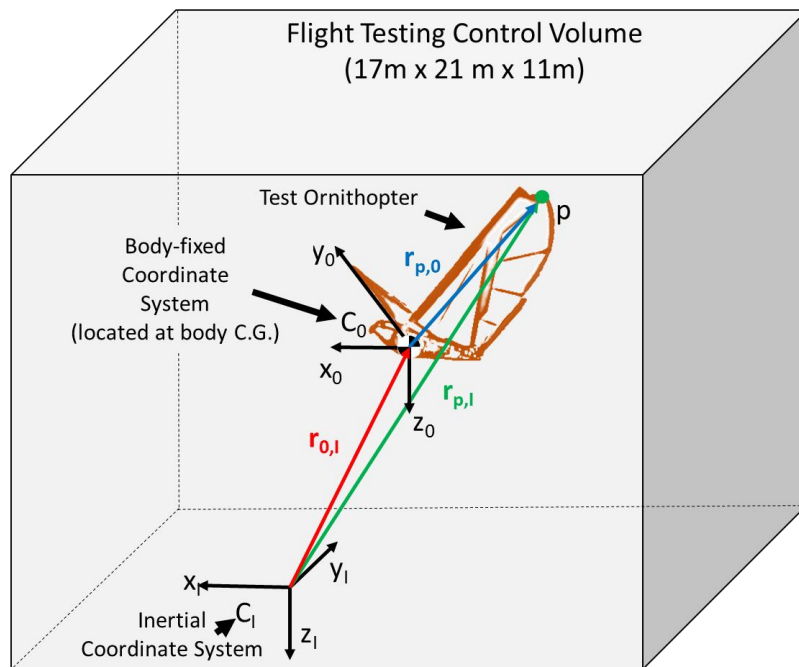


Figure 61. The flight testing control volume, showing the inertial, C_I , and body fixed, C_0 , coordinate systems along with the position vector naming conventions.

The inertial reference frame was defined in accordance with the north, east, down (NED) convention and the body axis was defined with the axes pointing out the nose, right wing, and underside of the ornithopter. Both reference frames are in accordance with standard aircraft body axes convention [62]. Based on the inertial and body reference

frames, a negative Z position indicates upwards displacement and a positive Z position indicates downwards displacement. Figure 61 also shows the naming convention for the position vectors. For example, $r_{0,I}$ was defined as the position vector of the center of mass of the fuselage with respect to the inertial frame. Also, $r_{p,I}$ and $r_{p,0}$ were defined as the position vector of any point, p, on the vehicle with respect to the inertial reference frame and the body reference frame, respectively.

Figure 62 shows the measured X, Y and Z positions of the 53 markers that were mounted on the ornithopter relative to the inertial reference frame, C_1 . The X and Y position represents the down range location of the marker and the Z position represent the marker's altitude. The figure also illustrates that repeatable tracking was achieved. The plot extends over eight consistent flapping cycles and represents a duration of 1.5 seconds of flight data. In order to estimate the accuracy of the markers' location and tracking, the ornithopter was placed in the middle of the control volume and the variances of the markers X, Y, and Z locations were computed. The maximum standard deviation was calculated to be 0.10 mm, 0.10 mm, and 0.12 mm for the X, Y, and Z markers location, respectively. Not only was it required that consistent and repeatable kinematics be achieved, but also the data needed to be recorded during steady level free flight. Figure 63 shows the Z position above ground level (AGL) of the center of mass of the ornithopter's fuselage with respect to the inertial frame, $r_{z 0,I}$. The location and orientation of the fuselage's center of mass was calculated by fitting a rigid body to the fuselage using the five markers that were mounted on it. More details about this technique can be found in [63]. The black line in Figure 63 represents a threshold altitude above which the vehicle is no longer suspended from the tether and therefore is in quasi free flight condition. From the figure, it can be concluded that the

ornithopter was flying well above this threshold altitude and therefore this flight test was successful in measuring and recording the ornithopter's kinematics over several flapping cycles and during steady level flight.

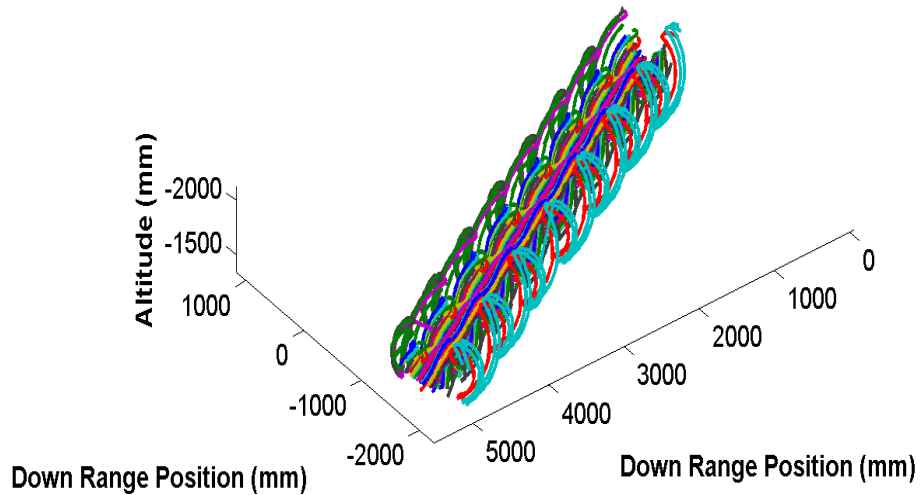


Figure 62. X, Y, and Z position of the 53 markers mounted on the ornithopter with respect to the inertial frame of reference showing over eight flapping cycles of consistent and repeatable kinematics.

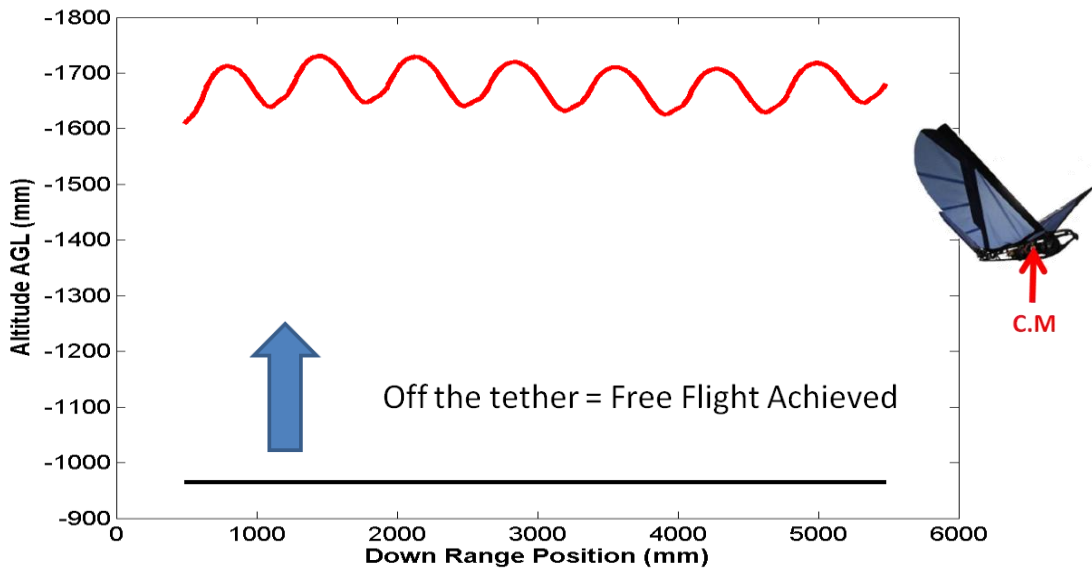


Figure 63. Ornithopter fuselage's center of mass altitude (red line) showing that the test ornithopter is flying above the altitude threshold (black line) for free flight.

After establishing free flight, the ornithopter kinematics was examined. Figure 64 compares the Z position above ground level in meters of the right wing tip marker ($r_{z,wt,I}$) and the fuselage's center of mass ($r_{z,0,I}$) for 2.5 flapping cycles. The figure shows that during free flight, the ornithopter's body position is out of phase with the wing tip position; in other words, as the wing flaps downwards, the fuselage is moving upwards and vice versa. Figure 64 also shows the ornithopter's body kinematics; an aspect of the vehicle's flight physics that is only possible to monitor through free flight testing.

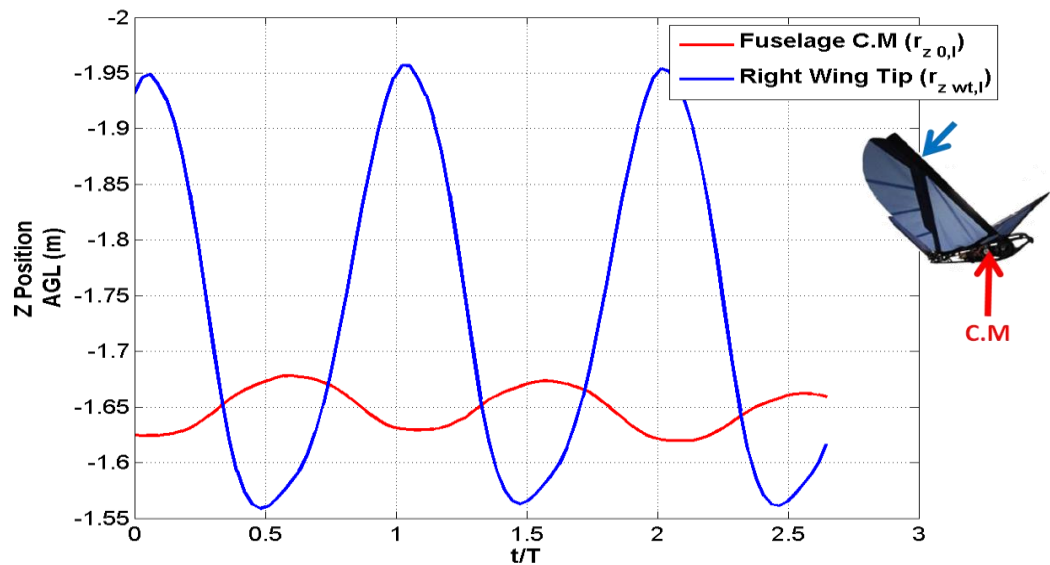


Figure 64. The altitude above ground level of the right wing tip marker (blue) and the fuselage's center of mass (red) versus time, normalized by the period of one flapping cycle.

In order to further understand the body kinematics, the Z position of the fuselage center of mass with respect to the inertial frame, $r_{z,0,I}$, was differentiated twice to obtain the center of mass vertical acceleration, $a_{z,0,I}$. Figure 65 shows the wing tip Z position with respect to the body frame in meters ($r_{z,wt,0}$), and the fuselage center of mass acceleration ($a_{z,0,I}$) in g_s with respect to the inertial frame.

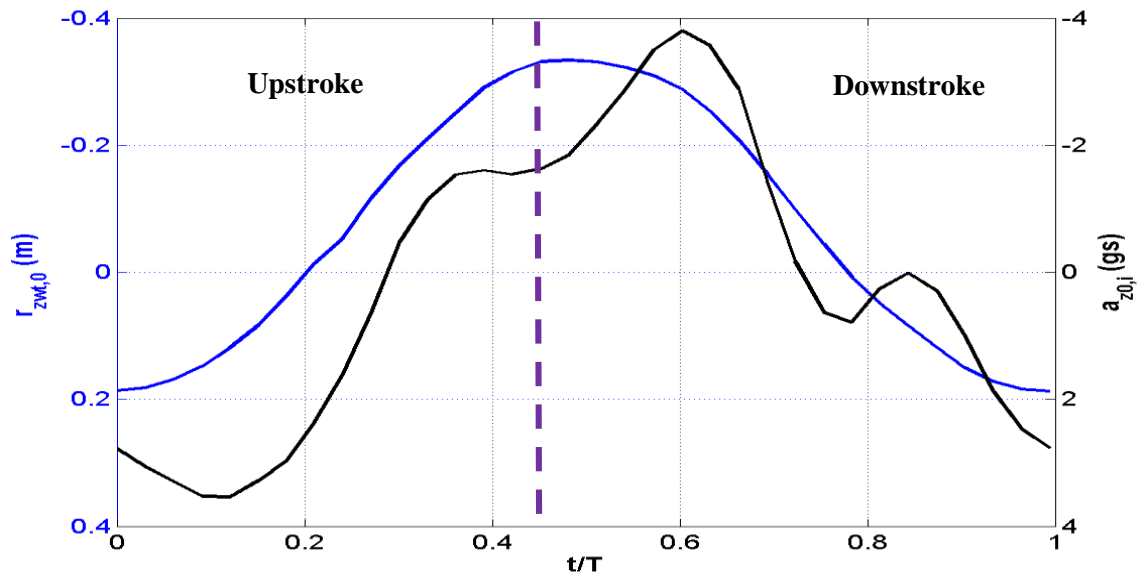


Figure 65. Wing tip marker Z-position with respect to the center of mass (blue) and the center of mass acceleration (black) versus time normalized by the period of one flapping cycle.

The significance of the body dynamics is apparent in Figure 65. The body of the the ornithopter with the continuous spar had an acceleration of ± 4 gs. During prior and current flight tests, it was noticed that the vertical acceleration had a peak after the upstroke-downstroke transition and downstroke-upstroke transition points [63, 61]. Figure 66 shows the Z position of the wing tip and the thrust flap with respect to the body frame, along with the vertical acceleration of the center of mass with respect to the inertial frame. The figure also shows that the peaks that occur after the transition points, marked by the red circles, are due to the thrust flap portion of the wing changing directions. The thrust flap portion of the wing is shown in Figure 67 and it is the part of the wing primarily responsible for the thrust production [6]. The thrust flap lags the main wing leading edge spar in changing directions at both stroke transition points. The thrust flap can be thought of as a hinged flat

plate, as it changes direction, it causes an increase in the body's acceleration. Figure 67 also shows the location of the wing tip and thrust flap markers.

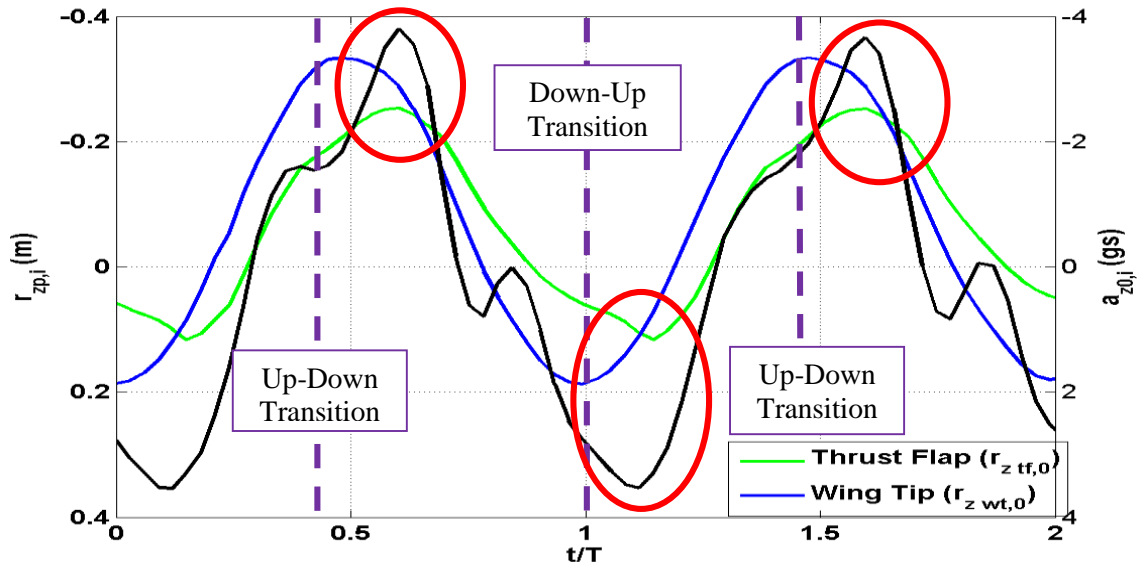


Figure 66. Wing tip marker Z-position with respect to the center of mass (blue), thrust flap marker Z-position with respect to the center of mass (green), and the center of mass acceleration (black) versus time, normalized by the period of one flapping cycle.



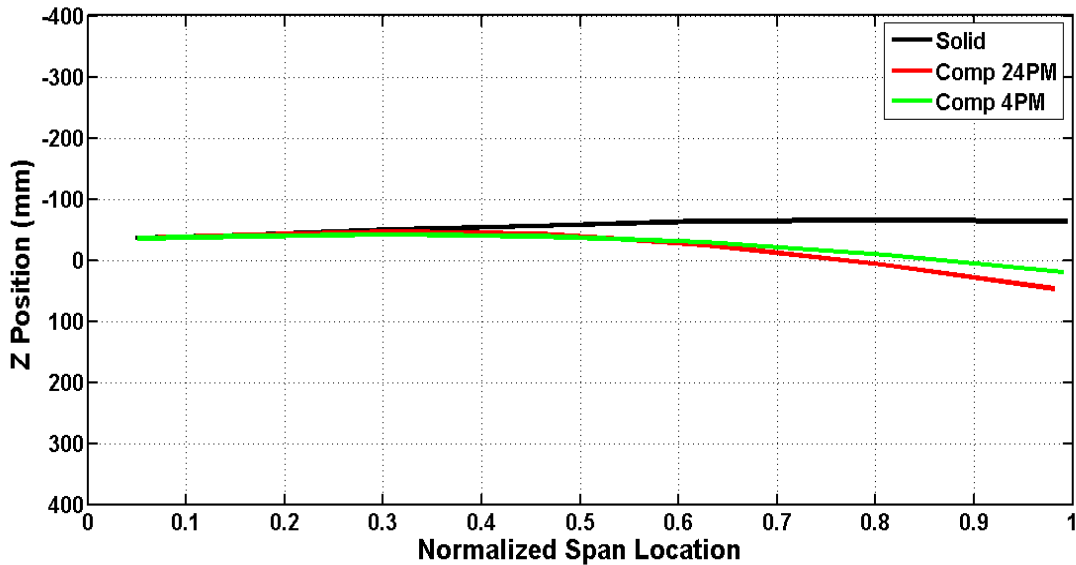
Figure 67. Wing planform showing the thrust flap region and the locations of the wing tip and thrust flap markers.

5.2.2. Effect of Compliant Spine Presence on Leading Edge Spar Deflection

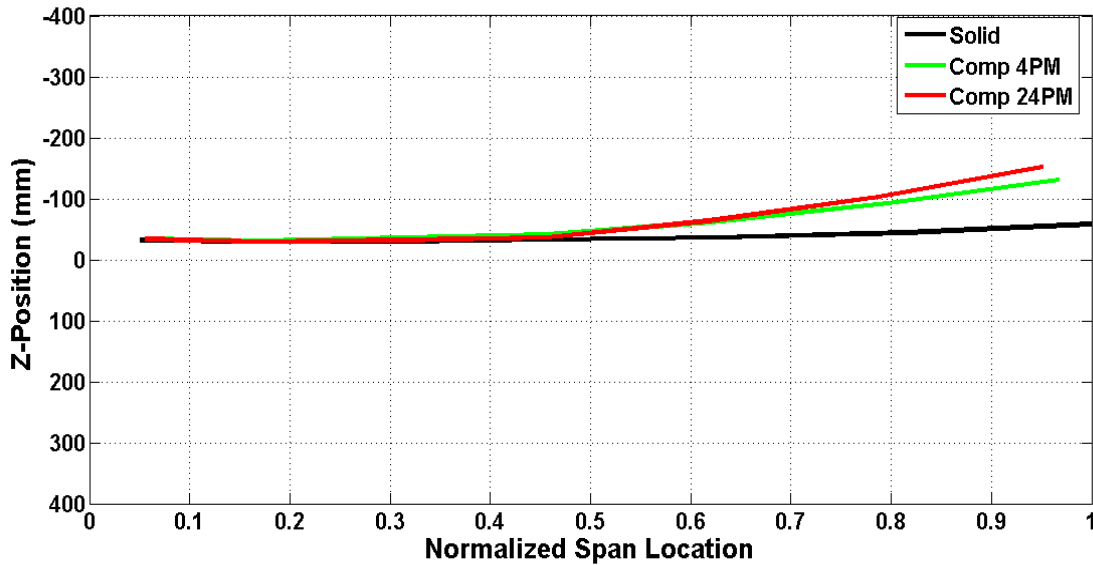
During the flight test, the three compliant spine designs described in Section 5.1.3 were inserted into the wing leading edge spar. This section details the effect of the presence of the compliant spine on the leading edge spar bending deflection. The compliant spine

design optimization results predicted that a compliant spine with a larger number of compliant hinges tends to have a greater maximum bending deflection [46, 64]. For this sub-section, results from designs Comp 24PM and Comp 4PM are shown as these designs had the most and least number of compliant hinges, respectively.

During the wing upstroke the compliant spine was allowed to bend due to the presence of the compliant joints, while during the downstroke, the contact surfaces come together, locking the compliant spine so that it simulated the uniform, rigid carbon fiber spar. Figure 68 a and b show the Z deflection in millimeters of the markers placed on the right wing leading edge spar, at mid upstroke and mid downstroke, respectively. The Z deflection for the leading edge spar markers was referenced to the body frame of reference.



(a) Mid upstroke



(b) Mid downstroke

Figure 68. The Z position of the reflective markers mounted at the right wing leading edge spar versus the normalized span location at (a) mid upstroke and (b) mid downstroke.

Figure 68 confirms the design optimization result that Comp 24PM was more flexible than design 4PM and therefore has a larger bending deflection. Figure 68(a) shows that the configuration with the compliant spar inserted in its wings were allowed to bend during the upstroke. The relative bending deflection between the compliant spar tip marker and the continuous spar tip marker at mid upstroke was 110.7 mm and 83.24 mm for the Comp 24PM and Comp 4PM designs, respectively. In Figure 68(b), upwards bending was observed, this bending occurs during the downstroke due to the presence of the contact gaps and flexibility of the DelrinTM spine. The relative bending deflection between the compliant spar tip marker and the continuous spar tip marker at mid downstroke was 94.3 mm and 72.6 mm for the Comp 24PM and Comp 4PM designs, respectively. Overall, the downwards bending deflection of the compliant spines during the upstroke was greater than the upwards bending deflection during the downstroke, thus an asymmetry in the wings kinematics was achieved due to the presence of the compliant spine.

5.2.3. Effect of Compliant Spine Presence on Wing Performance

Several metrics were used to investigate the effect of the presence of the compliant spine on the wing performance. These metrics can be divided into three categories: power expenditure, horizontal propulsive force and vertical propulsive force.

5.2.3.1. *The Power Expenditure Performance Metric*

Most morphing wing mechanisms, presented in the literature, show performance benefits, however they result in weight penalties that necessitate additional power expenditures that mitigate the performance gains [10, 21]. The first metric that was used to evaluate the wing performance of the hinged compliant and continuous ornithopter wing was the specific power. Specific power was defined as the electric power consumed by the flapping wing drive motor normalized by the mass of the ornithopter platform. Figure 69 shows a plot of the mean specific power over one flapping cycle for the compliant and continuous leading edge wing spar configurations. The figure shows that when normalized by the mass of the various configurations, the power expenditure of the compliant versus non-compliant configurations is comparable. Consequently, carrying the additional weight of the compliant spines, as compared to the weight of the continuous spar, does not cost the vehicle any significant power consumption penalty. The most compliant and heaviest configuration, namely Comp 24PM, has less than 5% penalty in specific power.

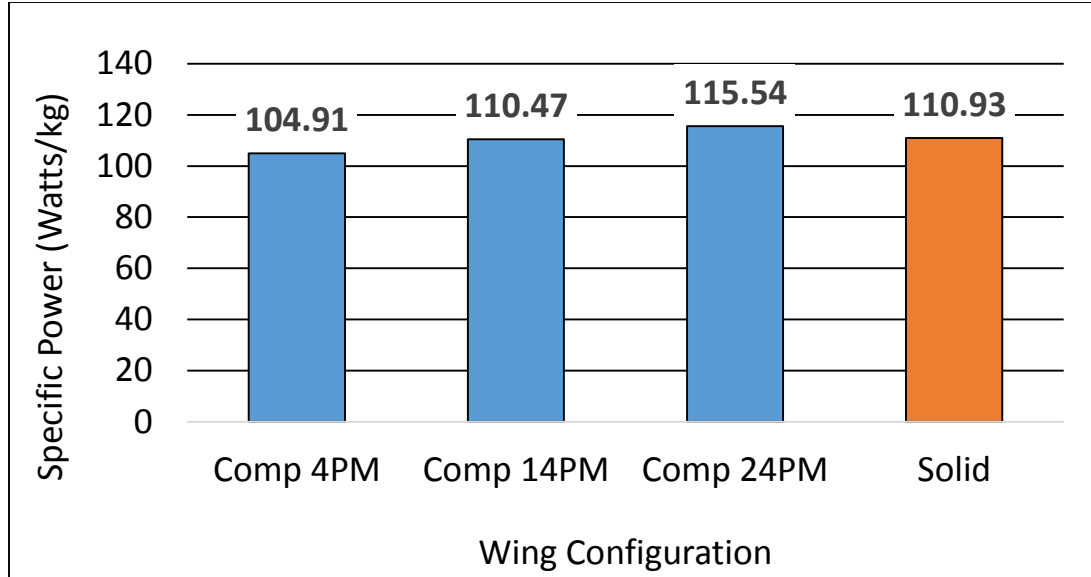


Figure 69. Mean specific power over one flapping cycle for the compliant and solid, non-compliant, wing configurations.

5.2.3.2. Horizontal Propulsive Force Performance Metric

The second group of metrics used to compare the performance of the test ornithopter wing with and without the presence of the compliant spine was related to the horizontal acceleration of the center of mass with respect to the inertial frame, $a_{x0,I}$. The horizontal acceleration can be related to the vehicle's thrust production. According to the body fixed frame of reference, a positive $a_{x0,I}$ corresponds to forward flight. Rather than using $a_{x0,I}$ directly to compare the effect of the various compliant spines, an additional metric that is common in the literature, namely the horizontal load coefficient, C_x is used [65]. The expression for C_x is shown in Equation (23) and it is the coefficient of propulsive force in the horizontal direction.

$$C_x = \frac{m \overline{a_{x0,I}}}{\frac{1}{2} \rho V_f^2 S} \quad (23)$$

In Equation (23), m is the vehicle's mass, ρ is the air density, V_f is the mean forward velocity, S is the wing area, and $\overline{a_{x0,I}}$ is the mean horizontal acceleration of the center of mass over one flapping cycle. C_X is the non-dimensional form of the mean horizontal force generated by the ornithopter over one flapping cycle. An intuitive way to explain C_X is that, for a given distance per unit time, a vehicle that has a larger value of C_X will have more propulsive power in the horizontal direction. Figure 70 compares the values of C_X for the solid, Comp 4PM, Comp 14PM, and Comp 24PM wing configurations. The figure shows that Comp14PM, Comp 24PM, and Comp 4PM improve the coefficient of horizontal propulsive force. When comparing the values of C_X for the compliant and non-compliant wing spar configurations shown in Figure 70, it should be noted that Comp 14PM improves C_X by 295% and it has the highest propulsive force in the horizontal direction.

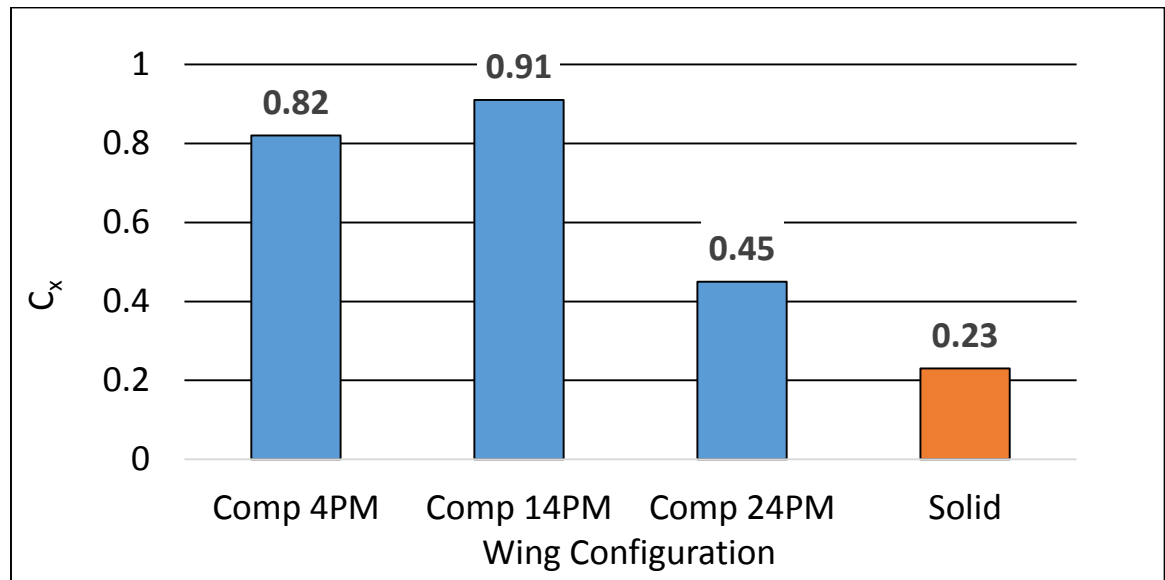


Figure 70. Coefficient of mean horizontal propulsive force for the compliant and solid, non-compliant, wing configurations.

The final metric related to the horizontal propulsive force is called the power loading and it is defined as C_X/C_P [65]. The horizontal power loading metric describes the amount of horizontal force that can be generated per unit power consumed, thus maximizing this quantity would indicate that the vehicle is able to generate a given amount of horizontal force efficiently. C_P is defined in Equation (24) and it is the non-dimensional mean electric power consumed over one flapping cycle [65].

$$C_p = \frac{\bar{P}}{\frac{1}{2} \rho V_f^3 S} \quad (24)$$

In Equation (24), \bar{P} is the mean power consumed over one flapping cycle. Table 7 compares the values of the horizontal power loading for the compliant and non-compliant configurations. From the values shown in the table, it can be concluded that the ornithopter with Comp14PM wing spar configuration generates horizontal propulsive force more efficiently than any of other configurations tested. Thus from a horizontal propulsive force production and therefore thrust and range standpoint, Comp 14PM offers the best design. Data from this flight test shows that the compliance achieved during the upstroke causes penalties to the mean horizontal acceleration produced, while compliance during the downstroke results in gains. Thus, Comp14PM offers the best compromise between up and down strokes compliance for horizontal force production.

Table 7. Values for horizontal power loading for the non-compliant and compliant wing spar configurations.

Wing Configuration	C_X/C_P
Solid	0.05
Comp 4PM	0.04
Comp 14PM	0.07
Comp 24PM	0.03

5.2.3.3. Vertical Propulsive Force Performance Metric

The third and final group of metrics used are related to the vertical acceleration of the center of mass with respect to the inertial frame, $a_{z0,1}$. According to the inertial frame of reference, negative vertical acceleration corresponds to upwards acceleration. Therefore a higher negative acceleration indicates an increase in the body's upwards acceleration and the wings' downwards acceleration, or an increase in the amount of positive vertical propulsive force produced by the wings. Figure 71 shows the vertical acceleration of the body center of mass for the Solid, Comp 4PM, and Comp 24PM configurations versus time normalized by the period of one flapping cycle. Only the most and least compliant configurations are shown below for graphical clarity, Comp 14PM exhibits the same body center of mass vertical acceleration characteristics.

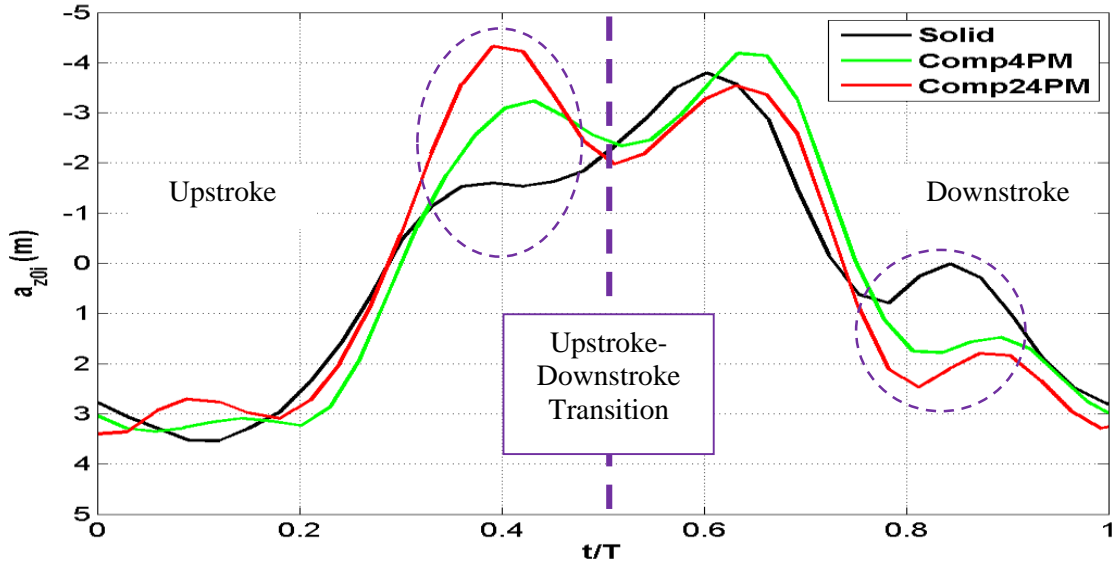


Figure 71. Vertical acceleration of the fuselage center of mass for the solid (black), Comp 4PM (green, and Comp 24PM (red) configurations versus time normalized by the period of one flapping cycle

The effect of the presence of a compliant spine in the leading edge spar is evident at two locations in the flapping cycle (marked by the dashed circles), as shown in Figure 71. The first location is at the end of the upstroke right before the upstroke to downstroke transition. At this point, the compliant spine is changing from the bending configuration to the locked configuration, creating an effect similar to a whiplash and increasing the body upwards acceleration. Therefore, increasing the wings' downwards acceleration, which is a favorable effect. During the downstroke portion of the flapping cycle, the compliant spine was designed so that the wing kinematics of the compliant wind spar are the same as those of the solid spar. However, as mentioned in Section 5.2.2, due to the presence of the contact gaps and the difference in Young's modulus between the material of the solid spar (unidirectional carbon fiber composite) and the material of the compliant spine (Delrin™) upwards bending occurs during the downstroke. The second location where the effect of the compliant spine is apparent is during the second half of the downstroke. At this point, the compliant spine has locked completely and the upward bending has started to occur. Thus, during the second half of the downstroke, an increase in the body's positive acceleration is observed due to the presence of the compliant spine. A higher positive vertical center of mass acceleration indicates an increase in the body's downwards acceleration and wings' upwards acceleration and therefore an increase in the amount of negative vertical propulsive force produced by the wings, which is an adverse effect.

In order to better quantify the effect of the compliance, the mean center of mass vertical acceleration over one flapping cycle was computed, $\overline{a_{z0,I}}$. Figure 72 shows the mean vertical acceleration over one flapping cycle for the Solid, Comp 4PM, Comp 14PM, and Comp 24PM wing spar configurations. The figure shows that the ornithopter with Comp

24PM and Comp 4PM inserted in its wing reduced the body's center of mass positive acceleration by 69% and 45%, respectively. While the ornithopter with Comp 14PM in its wing increased the body's center of mass positive acceleration by 5%. The positive acceleration reduction, which occurred due to presence of Comp 24PM and Comp4PM, translates, into vertical propulsive force gains. The positive acceleration increase, which occurred due to the presence of Comp 14PM, translates into a lift vertical propulsive force penalties. The most flexible design, namely Comp24PM, represents the superior design from a propulsive vertical force or payload capability viewpoint.

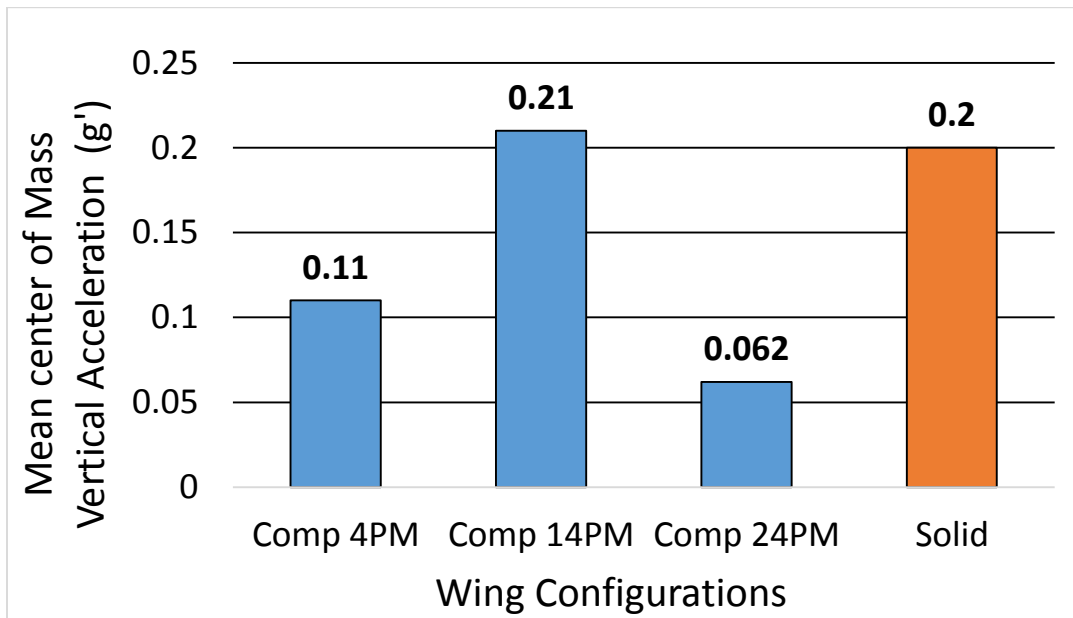


Figure 72. Mean positive vertical acceleration over one flapping cycle for the compliant and solid, non-compliant, wing configurations

A metric that is more common in literature, namely the vertical force coefficient, C_z is also used to compare the effect of compliance on the vertical propulsive force generated by the ornithopter [65]. The expression for C_z is shown in Equation (25) and it is the coefficient of propulsive force in the vertical direction.

$$C_z = \frac{m\overline{a_{z0,l}}}{\frac{1}{2}\rho V_f^2 S} \quad (25)$$

Similar to C_x , C_z is an indication of the propulsive force a vehicle can generate but in the vertical direction so, for a given distance per unit time, C_z can indicate the amount of propulsive power a vehicle can generate. As such, the objective here is to minimize C_z because, as explained before, a higher positive value for $\overline{a_{z0,l}}$ corresponds to more wings' upwards acceleration and more negative vertical propulsive force production. Table 8 shows the values of coefficient of vertical propulsive force, C_z , for the solid, Comp 4PM, Comp 14PM, and Comp 24PM wing configurations. Thus, when comparing the values of C_z for the compliant and continuous configurations, Comp 24PM has the lowest value of and thus the best vertical load production metric. Also, because the objective is to minimize rather than maximize C_z , it is not appropriate to use the power loading metrics as previously used for the horizontal load coefficient.

Table 8. Values for the coefficient of vertical propulsive force for the solid and compliant wing spar configurations.

Wing Configuration	C_z
Solid	0.48
Comp 4PM	0.71
Comp 14PM	0.98
Comp 24PM	0.31

5.3. Chapter Summary

The test results presented herein was successful in producing consistent and repeatable flight data over more than eight free flight flapping cycles and several compliant spine configurations. Throughout these flight tests, the ornithopter body dynamics were shown to be significant, $\pm 4g$ s for the solid configuration and with significantly different

acceleration profiles with the compliant spines. Also the peak in the body's vertical acceleration that occurred after the upstroke-downstroke and downstroke-upstroke transition points was attributed to the dynamics of the thrust flap. The effect of the presence of the compliant spines in the wings on leading edge spar deflection was examined through the flight tests. Inserting the compliant spine into the leading edge spar introduced an asymmetry between the upstroke and the downstroke, as desired. However, the data shows that upwards bending occurs during the downstroke due to the flexibility of Delrin and the contact gaps. Several metrics were presented and used to compare the performance of the compliant and baseline ornithopter wing. The first metric used was the specific power; data showed that, when normalized by the vehicle's mass, the test ornithopter with any given wing configuration consumed a similar amount of electric power. The second group of metrics used were related to the horizontal force produced over one flapping cycle, results showed that Comp 14PM design improved the mean horizontal propulsive force the most when compared to the other wing-spar configurations. Comp 14PM design increased the solid wing spar configuration horizontal propulsive force coefficient by 300%. The third and last group of wing performance metrics were related to the vertical propulsive force produced over one flapping cycle. Comp 24PM design reduced the solid wing spar configuration body's center of mass positive acceleration by 69%, which translates into overall vertical propulsive force gains. These flight tests showed that passively morphing the wings through introducing compliance in the leading edge spar is not only possible and requires no additional power expenditure but it is also beneficial to the overall vertical and horizontal propulsive force production.

Chapter 6: Concluding Remarks

6.1. Summary of Work

Wing morphing is needed for flapping wing un-manned vehicles in order for them to achieve mission adaptability and improved performance over multiple missions. This work contributes a passive wing morphing system that was shown to be both feasible and effective in improving steady level flight wing performance. Passive wing morphing was defined as wing shape change due to loads that the vehicle experiences during flight and not due to any other additional actuators.

Chapter 2 presented a bio-inspired technical approach towards achieving wing morphing. A review of avian wing morphology and kinematics was presented. The Continuous Vortex Gait was selected as the desired wing kinematics to be achieved using a structural modification. This gait was chosen because it is suitable for the test ornithopter steady level flight forward speed and wing Aspect Ratio. The continuous vortex gait could also be achieved passively because it required motion in only one major joint, namely the wrist. A compliant mechanism called a compliant spine was presented as the structural modification needed to achieve the wing morphing. The design load and bending deflection specifications for the compliant spine were determined and its integration in the test ornithopter leading edge spar to mimic the function of an avian wrist was demonstrated. .

The compliant spine allowed for bending during the upstroke only, thus its stiffness was time varying. Inserting a variable stiffness element in the leading edge spar required an analytical model in order to ensure the structural stability of the spar-spine system. Chapter 3 presented the analytical model of the leading edge spar with a compliant spine

inserted in it. The model was validated using experimental data. Analytical results from the model agreed with the experimental measurement within 7% and 11% for the wing root and spine root angles, respectively. The Equation of motion for the leading edge spar-spine system was reformulated into Mathieu's equation. The stability of the model was investigated graphically using a Strutt diagram and analytically using a phase plane plot. Both methods showed that the system response is stable and bounded.

After establishing stability, the ornithopter with various compliant spine designs inserted in its leading edge spar was evaluated experimentally. Chapter 4 presented constrained flight test both in air and in vacuum. Constrained flight testing was defined as testing where the ornithopter fuselage was constrained to a load cell and was not free to translate or rotate. The constrained flight tests results confirmed that passive wing morphing is beneficial to the overall steady level flight wing performance. At the steady level flapping frequency, 4.7 Hz, the ornithopter with the compliant spine achieved 44.7% reduction in the power required and 16% lift gain without incurring any thrust penalties. The power reduction suggested range and endurance benefits, where the lift gains indicated payload capability improvements. The results of the constrained flight test performed at the NASA Langley Research Center Thermal Vacuum Laboratory attributed the wing performance gains due to morphing to aerodynamic effects rather than inertial effects. In vacuum, the ornithopter with and without the compliant spine performed equally. In the presence of air, however, lift and thrust gains were observed for the ornithopter with the compliant spine inserted in the wings.

During the constrained flight test, the body dynamics could not be observed. Free flight testing was necessary in order to observe and investigate the body dynamics. Chapter 5

presented extensive free flight testing of the ornithopter with several compliant spine designs. The test was conducted at the Wright Patterson Air Force Base in the Air Force Research Lab's Indoor Small Unmanned Aerial Systems (SUAS) Laboratory and used a Vicon© motion tracking system. The test enabled the observation of the body dynamics, wing kinematics, and overall wing performance. The results confirmed that the ornithopter body dynamics were significant. Several metrics were presented and used to compare the performance of the test ornithopter wing with and without the compliant spine. Results showed that the ornithopter with a compliant spine consumed similar amount of specific power as an ornithopter without the compliant spine. However, the ornithopter with a compliant spine inserted in its wings, improved the horizontal propulsive force by 300% and improved body center of mass vertical acceleration by 69%, which translates into overall vertical propulsive force gains.

6.2. Summary of Original Contributions

The original contributions of this work is summarized in the following points:

- Bio-inspired avian kinematics

This work quantified and identified bio-inspired avian kinematics that were used as the design specifications for the passive wing morphing mechanism. The kinematics were inspired from the Continuous Vortex Gait. The bending kinematics of this gait were used as the required deflection for the morphing mechanism. One of the significant contributions of this work was realizing that an avian wing gait could be achieved passively using a wing structural modification, which would vary its shape in response to the aerodynamic loads experienced by the vehicle during steady level flight. Unlike other wing morphing systems,

these kinematics allowed the passive wing morphing system, presented in this work, to achieve lift gains without incurring any thrust penalties.

- A feasible and effective passive wing morphing

This work demonstrated that passive wing morphing was not only possible, but it was also beneficial for the overall steady level wing performance. This is the first morphing mechanism for avian scale flapping wing un-manned air vehicle, which achieved lift and thrust performance benefits without incurring weight, complexity, or power penalties.

- Extensive free flight data for avian scale flapping wing vehicles

Free flight data for avian scale flapping wing un-manned air vehicles was extremely limited. One of the significant contributions of this work was developing and extending a novel free flight testing technique. This technique provided the most extensive free flight data for avian scale flapping wing-unmanned vehicles. This data was used in this work to better understand the body dynamics and wing kinematics of the test ornithopter with the continuous and the hinged compliant leading edge spar. Results demonstrated the benefits of passive wing morphing on steady level flight. The effect of the presence of a wing morphing mechanism on the body vertical and horizontal propulsive force of an avian scale was examined for the first time in the literature. The data produced from these test was used to validate other researchers' numerical and analytical models of the test ornithopter and could be used to create the first avian scale ornithopters free flight database.

- Constrained flight data in vacuum

This work presented a constrained flight test of the ornithopter in vacuum. This test was considered a significant contribution because it isolated and the inertial effects from the aerodynamic effects. This test was the first of its kind for avian scale morphing

ornithopters. Through this test, it was determined that the wing performance gains observed due passive morphing was attributed to the aerodynamic effects and not inertial effects. The data from this test was also used to validate an analytical model to ensure the structural stability of the hinged compliant leading edge spar.

6.3.Future Recommendations

- Flow Visualization of Morphing Wing Wake

The work presented here stated that the compliant spine achieved the bending deflection desired for achieving the Continuous Vortex Gait. The main characteristic of the Continuous Vortex Gait is the continuous shedding of vortices from the wing tips into the wake of avian flyers. A flow visualization comparing the wake of the test ornithopter with and without a compliant spine inserted in its wing is necessary to determine the effect of the achieved bending deflection on the wake of the vehicle. The flow visualization will discern whether the performance benefits achieved due to the presence of the compliant spine are simply due to reducing the wing wetted surface area during the upstroke or is it in fact due to the vortices be shedding continuously from wing tip into the wake.

- Three Degrees of Freedom Morphing

The passive wing morphing system presented in this work achieve only one of the three degrees of freedom present in the Continuous Vortex Gait, namely bending. Future research should aspire to achieve bending, twist, and sweep passively. Wing twist and sweep during the upstroke can further decrease the wing wetted surface area and thus reduce the drag and negative lift penalty associated with this portion of the wing beat cycle. The author of this work along with collaborators from the Engineering Design and optimization Group at the Pennsylvania State University have published several papers that

focus on the design optimization of bend, sweep and twist compliant mechanisms for improved agility [66, 67, 68, 69]. The testing of these mechanisms is beyond the scope of this work but is highly recommended for future research.

- Spatially Distributed Compliant Elements

The work presented here focuses on improving the steady level flight wing performance and achieves so using one compliant spine at the location of the avian wrist. In order for flapping wing un-manned air vehicles to reach their full potential, they need to achieve mission adaptability or improved performance over several mission scenarios. Several spatially distributed multiple DOF compliant elements could facilitate such goal. These compliant elements could function as other major joints such as the elbow joint or as wing muscles that enable more complicated wing shapes. Achieving such wing shapes could improve the vehicle's agility and maneuverability as well as improve the vehicle's performance over multiple mission roles.

References

- [1] W. Shyy, H. Aono, S. K. Chimakurthi, P. Trizila, C. Kang, C. Cesnik and H. Liu, "Recent progress in flapping wing aerodynamics and aeroelasticity," *Progress in Aerospace Sciences*, vol. 46, no. 7, pp. 284-327, 2010.
- [2] W. Shyy, M. Berg and D. Ljungqvist, "Flapping and Flexible Wings for Biological and Micro Air Vehicles," *Progress in Aerospace Sciences*, vol. 35, pp. 455-506, 1999.
- [3] J. Grauer, "Modeling and System Identification of An Ornithopter Flight Dynamics Model," College Park, 2012.
- [4] M. Abdulrahim and R. Lind, "Modeling and control of micro air vehicles with biologically-inspired morphing," in *American Control Conference*, Minneapolis, 2006.
- [5] J. Gerdes, "Design, Analysis, and Testing of a Flapping Wing Miniature Air Vehicle," College Park, 2010.
- [6] R. Harmon, "Aerodynamic Modeling of Flapping Membrane Wing Using Motion Tracking Experiments," College Park, 2006.
- [7] P. Seshadri, M. Benedict and I. Chopra, "Understanding Micro Air Vehicle Flapping-Wing Aerodynamics Using Force and Flowfield Measurements," *Journal of Aircraft*, vol. 50, no. 4, pp. 1070-1087, 2013.

- [8] J. Delaurier, "An Aerodynamic Model for Flapping-Wing Flight," *The Aeronautical Journal of the Royal Aeronautical Society*, pp. 125-130, 1993.
- [9] J. M. Rayner, "Thrust and Drag in Flying Birds: Applications to Birdlike Micro Air Vehicles," in *Fixed and Flapping Wing Aerodynamics for Micro Air Vehicles*, Reston, American Institute of Astronautics and Aeronautics, 2001, pp. 217-230.
- [10] S. Barbino, O. Bilgen, R. Ajaj, M. Friswell and D. Inman, "A Review of Aircraft," *Journal of Intelligent Material Systems and Structures*, vol. 22, pp. 823-877, 2011.
- [11] "Merriam-Webster," [Online]. Available: <http://www.merriam-webster.com>. [Accessed 17 July 2014].
- [12] E. Garcia and J. Gomez, "Morphing unmanned aerial vehicles," *Smart Materials and Structures*, vol. 20, no. 10, 2011.
- [13] G. Taylor, A. Carruthers and T. Hubel, "Wing Morphing in Insects, Birds and Bats: Mechanism and Function," in *Morphing Aerospace Vehicles and Structures*, West Sussex, Wiley, 2012, pp. 13-40.
- [14] C. Thill, J. Etches, I. Bond, K. Potter and P. Weaver, "Morphing Skins," *The Aeronautical Journal*, vol. 112, pp. 117-139, 2008.

- [15] C. Grand, P. Martinelli, J. Mouret and S. Doncieux, "Flapping-Wing Mechanism for a Bird-Sized UAVs: Design, Modeling and Control," in *Advances in Robot Kinematics: Analysis and Design*, Springer, 2008, pp. 127-134.
- [16] J. Blondeau and D. Pines, "Pneumatic Morphing Aspect Ratio Wing," in *45th AIAA/ASME/ASCE/AHS/ASC Structures, Structural Dynamics & Materials Conference*, Palm Springs, 2004.
- [17] G. Zi-Wu and Y. Liang, "A study on aerodynamics and mechanisms of elementary morphing models for flapping wing in bat forward flight," 2014.
- [18] J. Colorado, A. Barrientos, C. Rossi and K. Breuer, "Biomechanics of smart wings in a bat robot: morphing wings using SMA actuators.," *Bioinspiration & Biomimetics*, vol. 7, no. 3, 2012.
- [19] G. Abate and W. Shyy, "Bio-Inspiration of Morphing for Micro Air Vehicles," in *Morphing Aerospace Vehicles and Structures*, West Sussex, Wiley, 2011, pp. 41-53.
- [20] Y. Tummala, "DESIGN AND OPTIMIZATION OF CONTACT-AIDED COMPLIANT MECHANISMS WITH NONLINEAR STIFFNESS," State College, 2013.
- [21] A. Conn, S. Burgess and C. Ling, "Design of a Parallel Crank-Rocker Flapping Mechanism for Insect-Inspired Micro Air Vehicles," *Journal of Mechanical Engineering Science*, vol. 221, pp. 1211-1222, 2007.

- [22] A. Cox, D. Monopoli, D. Cveticanin, M. Goldfarb and E. Garcia, "The Development of Elastodynamic Components for Piezoelectrically Actuated Flapping Micro-air Vehicles," *Journal of Intelligent Material Systems and Structures*, vol. 13, pp. 611-615, 2002.
- [23] K. Frampton, M. Goldfarb, D. Monopoli and D. Cveticanin , "Passive Aeroelastic Tailoring for Optimal Flapping Wings," in *Fixed and Flapping Wing Aerodynamics for Micro Air Vehicle Applications*, Reston, Wiley, 2001, pp. 473-482.
- [24] S. Banala and S. Agrawal, "Design and Optimization of a Mechanism for Out-of-Plane Insect Winglike Motion With Twist," *Journal of Mechanical Design*, vol. 127, pp. 841-844, 2005.
- [25] R. Madangopal, Z. Khan and S. Agrawal, "Biologically Inspired Design Of Small Flapping Wing Air Vehicles Using Four-Bar Mechanisms And Quasi-steady Aerodynamics," *Journal of Mechanical Design*, vol. 127, pp. 809-816, 2005.
- [26] P. Zdunich, D. Bilyk, M. MacMaster, D. Loewen, J. Delaurier, R. Kornbluh, T. Low, S. Stanford and D. Holeman, "Development and Testing of the Mentor Flapping-Wing Micro Air Vehicle," *Journal of Aircraft*, vol. 44, no. 5, pp. 1701-1711, 2007.
- [27] M. Demetgul, W. Pino and I. N. Tansel, "Morphing Wing Design for Ornithopters," in *ASME Early Career Technical Conference*, Miami, 2008.

- [28] D. Billingsley, G. Slipper, J. Grauer and J. Hubbard, "Testing of Passively Morphing Ornithopter Wing," in *AIAA Infrotech@Aerospace Conference*, Seattle, 2009.
- [29] D. Mueller, J. Gerdes and S. K. Gupta, "Incorporation of Passive Wing Folding in Flapping Wing Miniature Air Vehicles," in *International Design Engineering Technical Conferences & Computers and Information in Engineering Conference*, San Diego, 2009.
- [30] "Engineering Design & Optimization Group," [Online]. Available: <http://edog.mne.psu.edu/>. [Accessed 17 July 2014].
- [31] N. Chronister, "Ornithopter zone," [Online]. Available: <http://www.ornithopter.org/>. [Accessed 16 July 2014].
- [32] J. Videler, *Avian Flight*, New York: Oxford University Press, 2005.
- [33] K. Dial, "Avian forelimb Muscles and Non-steady Flight: Can birds fly without using the muscles in their wings," *The Auk*, vol. 109, no. 4, pp. 874-885, 1992.
- [34] B. Tobalske, "Biomechanics and Physiology of Gait Selection in Flying Birds," *Physiological and Biochemical Zoology*, vol. 73, no. 6, pp. 736-750, 2000.
- [35] J. M. Rayner, "On Aerodynamics and the Energetics of Vertebrate Flapping Flight," *Contemporary Mathematics*, vol. 141, pp. 351-385, 1993.

- [36] J. M. Rayner, "A vortex theory of animal flight. Part I. The vortex wake of a hovering animal," *Journal of Fluid Mechanics*, vol. 91, pp. 697-730, 1979.
- [37] J. M. Rayner, "A vortex theory of animal flight. Part II. The forward," *Journal of Fluid Mechanics*, vol. 91, pp. 731-763, 1979.
- [38] N. V. Kokshaysky, "Tracing the wake of a flying bird," *Nature*, vol. 279, pp. 146-148, 1979.
- [39] G. R. Spedding, "The wake of a kestrel (*Falco tinnunculus*) in flapping," *Journal of Experimental Biology*, vol. 127, pp. 59-78, 1987.
- [40] J. M. Rayner, "The mechanics of flight and bird migration performance," in *Bird Migration*, Heidelberg, Springer Verlag, 1990, pp. 283-299.
- [41] M. Rosen, "The relationship between wingbeat kinematics and vortex wake of a thrush nightingale.," *Journal of Experimental Biology*, vol. 207, pp. 4255-4268, 2004.
- [42] B. Tobalske and K. Dial, "Flight kinematics of black-billed magpies and pigeons over a wide range of speeds.," *Journal of Experimental Biology*, vol. 199, pp. 263-280, 1996.
- [43] B. Tobalske, "Biomechanics of bird flight," *The Journal of Experimental Biology*, vol. 210, pp. 3135-3146, 2007.

- [44] B. Tobalske, T. Hedrick, K. Dial and A. Biewener, "Comparative power curves in bird flight.," *Nature*, vol. 421, pp. 363-366, 2003.
- [45] R. H. Brown, "The Flight of Birds: Wing Function in Relation to Flight Speed," *Journal of Experimental Biology*, vol. 30, pp. 90-103, 1953.
- [46] Y. Tummala, A. Wissa, M. Frecker and J. Hubbard Jr., "Design Optimization of a Compliant Spine for Dynamic Applications," in *Smart Materials, Adaptive Structures and Intelligent Systems Conference*, Scottsdale, 2011.
- [47] Y. Tummala, A. Wissa, M. Frecker and J. Hubbard Jr, "Design of a Passively Morphing Ornithopter Wing using a Novel Compliant Spine," in *Smart Materials, Adaptive Structures and Intelligent Systems*, Philadelphia, 2010.
- [48] "Concord Field Station," 2008. [Online]. Available: <http://www.oeb.harvard.edu/cfs/media.html>. [Accessed 17 July 2014].
- [49] T. Hedrick, J. Usherwood and A. Biewener, "Wing inertia and whole-body acceleration: an analysis of instantaneous aerodynamic force production in cockatiels (*Nymphicus hollandicus*) flying across a range of speeds," *The Journal of Experimental Biology*, vol. 207, pp. 1689-1702, 2004.
- [50] T. Hedrick, B. Tobalske and A. Biewener, "Estimates of circulation and gait change based on a three-dimensional kinematic analysis of flight in cockatiels (*Nymphicus hollandicus*) and ringed turtle-doves (*Streptopelia risoria*)," *The Journal of Experimental Biology*, vol. 205, pp. 1389-1409, 2002.

- [51] N. M. Wereley, "Analysis and Control of Linear Periodically Time Varying Systems," 1991.
- [52] E. I. Butikov, "Parametric Excitation of a Linear Oscillator," *European Journal of Physics*, vol. 25, pp. 535-554, 2004.
- [53] A. Nayfeh, *Nonlinear Oscillations*, New York: Wiley, 1979.
- [54] N. W. McLachlan, *Theory and Application of Mathieu Functions*, New York: Dover, 1964.
- [55] S. V. Simakhina, "Stability Analysis of Hill's Equation," 2003.
- [56] G. W. Hill, "On the part of the lunar perigee which is a function of the mean motions of the sun and the moon," *Acta Mathematica*, vol. 8, pp. 1-36, 1886.
- [57] J. A. Richards, "Stability Diagram Approximation for the Lossy Mathieu Equation," *SIAM Journal on Applied Mathematics*, vol. 30, no. 2, pp. 240-247, 1976.
- [58] A. Wissa, Y. Tummala, J. Hubbard Jr., M. Frecker and M. Northrup, "Inertial Effects Due to Passive Wing Morphing in Ornithopters," in *22nd AIAA/ASME/AHS Adaptive Structures Conference*, National Harbor, 2014.
- [59] A. Wissa, Y. Tummala, J. Hubbard Jr. and M. Frecker, "Passively Morphing Ornithopter Wings using a Novel Compliant Spine: Design and Testing," *Smart Materials and Structures*, vol. 21, no. 9, 2012.

- [60] A. Wissa, Y. Tummala, J. Hubbard Jr., M. Frecker and A. Brown, "Testing of Novel Compliant Spines for Passive Wing Morphing," in *Smart Materials, Adaptive Structures and Intelligent Systems*, Scottsdale, 2011.
- [61] A. Wissa, J. Grauer, N. Guerreiro, R. Roberts, C. Altenbuchner, J. Hubbard Jr., Y. Tummala and M. Frecker, " Flight Testing of Novel Compliant Spines for Passive Wing Morphing on Ornithopters," in *54TH AIAA/ASME/ASCE/AHS/ASC Structures, Structural Dynamics, and Materials Conference*, Boston, 2013.
- [62] B. Etkin, *Dynamics of Flight: Stability and Control.*, New York: Wiley, 1982.
- [63] J. Grauer, E. Ulrich, J. Hubbard Jr., P. Darryll and S. Humbert, "Testing and System Identification of An Ornithopter in Longitudinal Flight," *Journal of Aircraft*, vol. 48, p. 660–667, 2011.
- [64] Y. Tummala, A. Wissa, M. Frecker and J. Hubbard Jr., "Design and Optimization of a Contact-Aided Compliant Mechanism for Passive Bending," *Journal of Mechanisms and Robotics*, vol. 6, no. 3, 2014.
- [65] L. Zheng, T. Hedrick and R. Mittal, "Comparative Study of the Hovering Efficiency of Flapping and Revolving Wings.," *Bioinspiration and Biomimetics*, vol. 8, no. 3, 2013.
- [66] Y. Tummala, M. Frecker, A. Wissa and J. Hubbard Jr., "Design and optimization of a bend-and-sweep compliant mechanism," *Smart Material and Structures*, vol. 22, 2013.

- [67] Y. Tummala, M. Frecker, A. Wissa and J. Hubbard Jr, "Design Optimization of a Twist Compliant Mechanism With Nonlinear Stiffness," in *Smart Materials, Adaptive Structures and Intelligent Systems*, Snowbird, 2013.
- [68] Y. Tummala, M. Frecker, A. Wissa and J. Hubbard Jr, "Design and Optimization of a Bend-and-Sweep Compliant Mechanism," in *International Design Engineering Technical Conferences and Computers and Information in Engineering Conference*, Portland, 2013.
- [69] Y. Tummala, M. Frecker, A. Wissa and J. Hubbard, "Design of Bend-and-Sweep Compliant Mechanism for Passive Shape Change," in *Smart Materials, Adaptive Structures and Intelligent Systems*, Stone Mountain, 2012.